Modelling Fluid Dynamics and Mass Transfer in Bubble Plumes using Lagrangian Particle Tracking

by

Mengyao Wang

Submitted in partial fulfilment of the requirements
for the degree of **Master of Applied Science**

at

Dalhousie University
Halifax, Nova Scotia
August 2019

Table of Contents

List of Tables

List of Figures

Abstract

A solver was developed in OpenFOAM to simulate fluid dynamics and gas dissolution in bubble plumes. The solver uses Lagrangian particle tracking (LPT) to resolve the motion of individual bubbles or bubbles grouped into parcels. Interphase momentum exchange models are used to provide two-way coupling between the motion of the bubbles and the surrounding liquid. The volume-of-fluid (VOF) method is used to track the position of the gas-liquid free surface. The performance of the hybrid LPT-VOF solver was verified using several theoretical test cases. Solver validation employed three bubble plume validation cases with experimental data from the literature: small-scale vertical injection, small-scale horizontal injection, and large-scale vertical injection. Overall, the predicted results are in good agreement with the experimental results. Although the solver predicts reasonable results, it has limitations on the implemented interphase momentum and mass exchange methods, averaging techniques, and has not been tested for non-uniform bubble size distributions.

List of Abbreviations and Symbols Used

Abbreviations

CFD	Computational Fluid Dynamics
CL	Contour Level
DBM	Discrete Bubble Model
DPM	Discrete Phase Model
DRW	Discrete Random Walk
EE	Eulerian-Eulerian
EL	Eulerian-Lagrangian
LES	Large Eddy Simulations
LPT	Lagrangian Particle Tracking
IT	Interface Tracking
OpenFOAM	Open-source Field Operation and Manipulation
PBM	Population Balance Model
PISO	Pressure-Implicit with Splitting of Operators
PIV	Particle Image Velocimetry
RANS	Reynolds-Averaged Navier-Stokes
SGS	Subgrid-Scale
SIMPLE	Semi-Implicit Momentum Linked Equations
VLES	Very Large Eddy Simulation
VOF	Volume-of-Fluid

Symbols

A	Area (m^2)
A_p	Projected Area of Particle (m^2)
a	Interfacial Area (m^2)
C	Oxygen Concentration at Time t (kg/m^3)
C_0	Initial Concentration of Oxygen (kg/m^3)
C_D	Drag Coefficient (-)
C_L	Lift Coefficient (-)
c_p	Specific Heat Capacity (J/kg/K)

C_s	Smagorinsky Coefficient (-)
C_{sat}	Concentrations of Dissolved Oxygen at the Saturation Condition (kg/m^3)
C_{TD}	Turbulent Dispersion Coefficient (-)
C_{VM}	Virtual Mass Coefficient (-)
C_μ	Model Constant for Turbulent Viscosity (-)
D_{ab}	Mass Diffusivity Coefficient (m^2/s)
Eö	Eötvös Number (-)
Eö$_d$	Modified Eötvös Number (-)
F_B	Buoyancy Force (N)
F_D	Drag Force (N)
F_G	Gravitational Force (N)
F_L	Lift Force (N)
F_{LPT}	Exchange of Momentum from the Dispersed Phase
F_{ST}	Surface Tension Force (N)
F_{TD}	Turbulent Dispersion Force (N)
F_{VM}	Virtual Mass Force (N)
F_d	Source Term in the Momentum Equation
Fr'	Modified Froude Number (-)
$\vec{g}$	Gravitational Acceleration (m/s^2)
h	Position (m)
H	Dimensionless Henry's Law Constant (-)
J	Mass flux (kg/m^2/s)
k_l	Mass Transfer Coefficient (m/s)
$k_l a$	Volumetric Mass Transfer Coefficient (1/s)
l_e	Dissipation Length Scale (m)
m	Mass (kg)
$\dot{m}$	Mass Flow Rate (kg/s)
$\vec{M}$	Interphase Momentum Exchange Term
M_{LPT}	Exchange of Mass from the Dispersed Phase to the Continuous Phase
p_{rgh}	Modified Pressure (Pa)
P	Pressure (Pa)
Pr	Prandtl Number (-)

R	Universal Gas Constant (m^3 Pa/K/mol)
Re	Reynolds Number (-)
S	Source Term (various units)
Sc	Schmidt Number (-)
Sh	Sherwood Number (-)
S_P	Implicit Source Terms (s^{-1})
S_U	Explicit Source Terms (s^{-1})
$S_{U,g}$	Momentum Source Transferred from the Lagrangian Phase to the VOF Gas Phase ($kg/m^2/s^2$)
$S_{U,l}$	Momentum Source Transferred from the Lagrangian Phase to the VOF Liquid Phase ($kg/m^2/s^2$)
t	Time (s)
T	Temperature (K)
$\vec{u}$	Velocity (m/s)
$\vec{u}_{drift}$	Drift Velocity (m/s)
$\vec{u}_R$	Relative Velocity (m/s)
V	Volume (m^3)
W	Molecular Weight (g/mol)
x	Position in the x Direction (m)
x_i	Position in the i Direction (m)
x_j	Position in the j Direction (m)
Y	Mass Fraction (-)
Y_{1,O_2}	O_2 Mass Fraction in the Liquid Phase (-)
Y_{1,N_2}	N_2 Mass Fraction in the Liquid Phase (-)

Greek Letters

α	Phase Volume Fraction (m^3/m^3)
α_{local}	Local Volume Fraction (m^3/m^3)
ε	Turbulent Dissipation Rate (m^2/s^3)
θ	Spreading Angle (°)
μ	Dynamic Viscosity (Pa s)
ν_t	Turbulent Kinematic Viscosity (m^2/s)

π	Ratio of the Circumference of a Circle to its Diameter (-)
ρ	Density (kg/m^3)
σ_{SD}	Standard Deviation
σ_{ST}	Surface Tension (N/m)
τ	Stress Tensor (N/m^2)
ω	Specific Turbulent Dissipation Rate (1/s)

Subscripts

0	Initial Value
1	VOF Liquid Phase
2	VOF Gas Phase
b	Bubble
c	Continuous Phase
cell	Computational Cell
d	Dispersed Phase
i	Species
k	Phase Indicator
l	Liquid
m	Mixture
M	Mass
p	Particle
t	Time
∞	Single-Bubble System

Superscripts

i	Species
j	Bubble (or Parcel) Number in a Computational Cell
sol	Solubility
*	Solubility
T	Transpose

Acknowledgements

First, I would like to acknowledge my supervisor, Dr. Jan Haelssig, for his continual guidance and support in my whole degree.

Subsequently, I would like to thank my committee members, Dr. Adam Donaldson and Dr. Arturo Macchi, for reading the thesis and providing thoughtful feedback and suggestions.

Additionally, I would like to thank my colleagues for their experience sharing and help. Especially, I would like to thank Dr. Devin O'Malley, who helped me a lot with code troubleshooting and thesis reviewing.

Finally, I would like to thank my parents, family, and friends for their support throughout my life.

Chapter 1: Introduction

1.1. Introduction

Dispersed bubbly flows are important in many industrial processes, particularly in reactors, separation systems, and a variety of other processes requiring high interfacial surface area. Bubbly flows can be uniform, such as in bubble columns. Alternatively, they can be released from a point source into a larger reservoir, such as in aeration systems. The primary benefit of dispersed flow is an increase in the interfacial contact area, which provides a larger surface area for reactions to exploit and promotes interphase heat and mass transfer.

There are many examples of systems that use bubbles released from a point source to form a bubble plume, which then promotes mixing and heat and mass transfer. A small-scale example of a bubble plume is the aeration of a fish tank. On a larger scale, bubble plumes are commonly employed for aeration of ponds, lakes, and basins to improve water quality and ensure that there is a sufficient supply of oxygen for fish. Air injected at the bottom of lakes or reservoirs can also be used for mixing to avoid thermal stratification (Helfer et al., 2012). In aquaculture, supplemental aeration is often required to meet the metabolic oxygen requirements of fish and to reduce mortality and increase birth rates. Aeration in large tanks is also commonly used in wastewater treatment processes.

Another commonly investigated situation, due to its potential environmental and safety consequences, is the accidental release of gas into the ocean at offshore oil and gas facilities. Such releases could occur due to a loss of containment at a wellhead or from a broken transport pipeline and would result in the formation of a large-scale bubble plume. To perform a risk assessment, it is important to be able to predict the fluid dynamics and mass transfer in such plumes because this will determine the location and quantity of harmful and hazardous gases when they reach the ocean surface. Therefore, predictive models are necessary to perform risk assessments in order to minimize the effects of a potential release on the environment, human life, and loss of assets (Olsen and Skjetne, 2016).

Bubble plumes are normally divided into three different zones: jet zone, plume zone, and surface zone. Each of these zones has to its own governing time and length scales. Figure 1.1 illustrates the location of the three zones for vertically- and horizontally-injected plumes. The zone just above the release point is often referred to as the near-field, momentum-governed, or jet zone. When the gas is first released into the liquid, it forms a jet-like flow, where the momentum from the source drives the gas phase trajectory. The liquid in this zone is pushed and sheared upward while being entrained, which results in highly turbulent flows (Schaub and Pluschkell, 2006). Depending on how the gas is injected into the liquid, the interface between the gas and liquid may form a continuous free surface. In this case, the momentum dissipated by the release helps to disperse and break up the gas into a swarm of bubbles. However, in some cases it is also possible to form a dispersed bubbly flow directly at the injection point. The size and existence of the jet zone depends on the flow condition and the Weber number at the injection point.

As momentum is dissipated into the surrounding liquid, large clumps of gas break free from the momentum core and eventually disperse into smaller and smaller bubbles. This marks the transition to a region called the plume zone, where the bubbles drift toward the surface due to the buoyancy force. Those rising bubbles drive and entrain the surrounding liquid. In addition to gravity and buoyancy, the bubbly flow is governed by local forces such as drag, lift, and virtual mass, as well as collisions between particles. The bubbles in the plume zone are smaller and more dispersed than in the near-field region, which drastically increases the interfacial area density. The final region within a bubble plume, known as the surface zone, occurs when the plume reaches the free surface. In the surface zone, the gases are released through the free surface and detrainment of liquid causes an outward flow. The development of waves and the radial outflow of liquid can promote extra mixing in the vicinity of the surface, which will impact the detrainment and entrainment of the gas above and below the interface.

Mass transfer (e.g., gas dissolution) or reactions can occur in every zone within a bubble plume. However, the momentum-governed region is usually small because the gas phase has a low density, which means that its momentum will be readily dissipated into the liquid phase. This means that the plume zone is typically the dominant zone, especially as the

depth of the release increases. Most mass transfer therefore occurs in the plume zone and can be predicted using correlations for dispersed bubbly flow. The mass transfer rate is governed by the relative velocity between the liquid and gas, solubility, diffusivity, residence time, and surface area of the bubbles (Olsen and Skjetne, 2016).

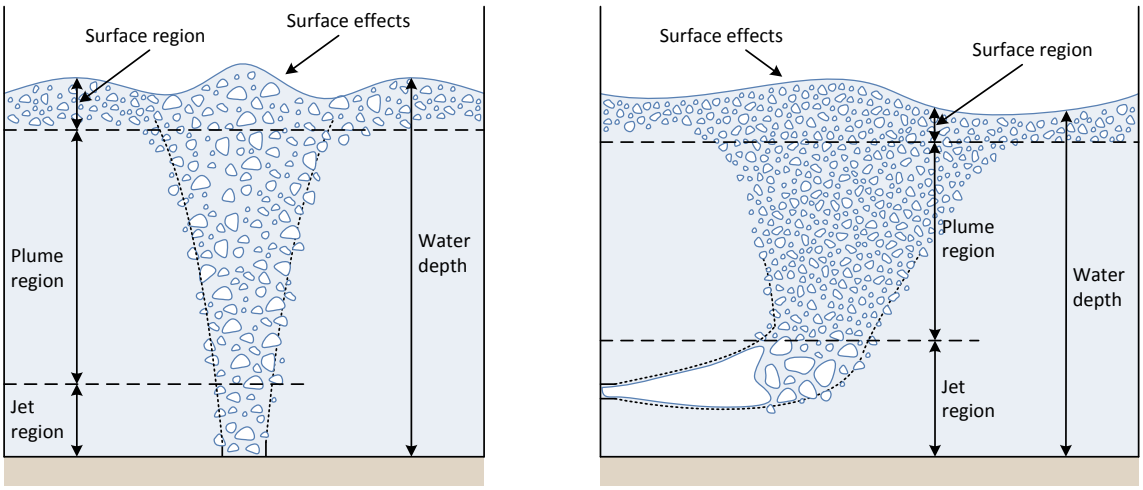

Figure 1.1: Schematic representation of vertically (left) and horizontally (right) injected plumes.

As stated by Olsen and Skjetne (2016), the modelling of two-phase plumes dates back to the middle of the 20th century. The work done by Morton et al. (1956) was considered the first published study on two-phase plume modelling. Ditmars and Cederwall (1974) included the compressibility of the gas and the slip velocity of bubble based on the model of Morton et al. (1956). These models are known as integral models because the governing equations are integrated along the plume trajectory. The radial profiles of field variables (e.g., velocity, gas phase fraction, temperature, etc.) are assumed to follow prescribed mathematical functions, rendering the models one-dimensional. Most commonly, the Gaussian and top hat profiles are used to represent the radial distribution (Olsen and Skjetne, 2016). The conservation equations for liquid, gas, and momentum are derived via the gas control volume at each height and solved to obtain the vertical profiles of the field variables.

Brevik et al. (1977, 1996) further improved integral models by considering the conservation equations of momentum, total mass, and the kinetic energy and introducing a kinetic energy related coefficient to the added momentum to provide more insight into the

plume hydrodynamics. This kinetic energy method was extended later to include gas dissolution (Einarsrud and Brevik, 2009). Given their fundamental assumptions, integral models are restricted to modelling bubbly plumes rather than those cases with significant jetting, and rarely consider free surface interactions. Additionally, most integral models assume the concentration of dissolved gas in the background liquid phase to be negligible. In other words, these models rarely track the concentration in the background field (Olsen and Skjetne, 2016). Another drawback in the concept of the integral models is that local turbulence is not considered and that bubble sizes are assumed to be related to gas expansion and gas dissolution only. Although the global impact of turbulence can be incorporated globally into the model (e.g., entrainment), the lack of local resolution makes it difficult to develop more detailed modelling approaches. This is important because the local turbulence in the liquid plays an important role in both fluid dynamics and mass transfer, which control gas dissolution rate, bubble sizes, and the spreading of the plumes (Olsen and Skjetne, 2016).

More recently, computational fluid dynamics (CFD) models have been applied as an alternative to integral models for bubble plumes. CFD models can directly track the concentration of the dissolved gas in the liquid phase and can provide local information about the background flow and turbulence. However, the primary disadvantage with CFD methods are the higher computational costs, which lead to longer runtimes. It can also be quite challenging to parameterize the empirical closure relationships in CFD models because they are inherently more complex. Nonetheless, CFD approaches are gaining popularity because local turbulence has a significant impact of the motion of bubbles in the plume (Sheng and Irons, 1995), and the available local information facilitates the development of more detailed interphase momentum, heat transfer, and mass transfer closure models. For example, Buscaglia et al. (2002) simulated the aeration of lakes using CFD with the Eulerian model and they successfully reproduced the results obtained from the integral models with a slightly higher accuracy.

CFD is a useful and powerful tool for modelling bubble plumes that can provide detailed information on plume mechanics, which can be used to select key experiments and to tune integral models. There are two approaches that are currently widely used to simulate gas-

liquid dispersed flows: the Eulerian-Eulerian (EE) method and the Eulerian-Lagrangian (EL) method. The EE, or two-fluid method, treats the liquid (continuous phase) and gas (dispersed phase) phases as interpenetrating fluids represented by volume fractions in each computational cell. The conservation equations are solved independently for each phase and coupled through source terms in each equation. Although EE has a lower computational cost than methods that attempt to resolve gas-liquid interface dynamics, EE methods have trouble capturing the jet transition (Olsen and Skjetne, 2016). Another disadvantage of EE methods is that they cannot accurately resolve the free surface without modification.

The Euler-Lagrange (EL) method, also known as the Lagrangian particle tracking (LPT) method, is an alternative CFD approach to the EE method for modelling bubble plumes. In this approach, the continuous phase is solved on an Eulerian grid, while the dispersed phase is tracked by a series of Lagrangian particles which are advected by solving the force balance. Therefore, the dispersed bubbles can be tracked individually. The motion of the bubbles is governed by Newton's second law and can be coupled to the continuous phase through interphase momentum exchange terms. The individual bubbles can be grouped into parcels (clusters) to reduce computational cost if the number of the bubbles is extremely high. In these cases, the force balance is conducted on the entire parcel. The interphase momentum exchange terms include the forces that act on the bubbles or parcels, such as gravity, buoyancy, drag, lift, virtual mass, and collision between particles. The interphase exchange terms can also be used to modify the background flow (i.e., two-way coupling). Although EE methods have a fixed computational cost based on grid size, the computational cost of the EL method increases when simulating a large number of particles. However, the background computational grid can often have a lower resolution because the particle balances are performed on each particle (or parcel) in order to track their exact position. Like EE methods, EL cannot be used to directly simulate the free surface. Therefore, EL methods need to be combined with another method to include the effects of the free surface and increase computational accuracy in this region. The modelling of the free surface can be achieved by coupling an interface tracking/interface capturing (IT) method to the EL algorithm.

IT methods are used to directly predict the motion of the gas-liquid interface. IT methods, in general, offer a more accurate representation of the interface at the cost of increased mesh refinement so that surface deformations can be accurately modelled (Wörner, 2012). In general, the required mesh resolution would be too high to use IT methods to capture the motion of the gas-liquid interface in a dispersed bubbly flow. However, it is possible to use IT methods to approximate the motion of the gas-liquid interface using a relatively coarse mesh when the interface does not include very small structures. For example, the volume-of-fluid (VOF) method is often used to model free surface behaviour for liquid flow around structures and ships (Godderidge et al., 2015; Yang et al., 2005; Wang et al., 2008). In this study, the VOF method is used to model free surface behaviour and combined with the EL approach to model the surface region in bubble plumes. The hybrid LPT and VOF approach exploits the advantages of both methods to provide accurate predictions of hydrodynamics and mass transfer in bubble plumes.

1.2. Objectives

The primary objective of this work was to develop a new solver in OpenFOAM (Open-source Field Operation and Manipulation) that combines the Lagrangian library with a compressible VOF solver. The solver is intended to be used to model fluid dynamics and mass transfer in large-scale bubble plumes. This development required the coupling of the pre-existing LPT and VOF solvers, expansion of the existing libraries to include methods to predict gas dissolution, the implementation of several post-processing utilities to facilitate data analysis, and validation of simulation predictions against fluid dynamics and mass transfer experiments found in the literature.

A summary of the specific objectives for this work is as follows:

- Develop and implement a hybrid LPT-VOF solver that can track bubbles/parcels in large-scale bubble plumes and simulate free surface motion.
- Include the effects of gas compressibility on bubble size and therefore predict the density and diameter changes of the bubbles at different depths.
- Implement a gas dissolution model in the Lagrangian library.

- Verify the coupling of the solver and implemented gas dissolution model through small-scale verification cases.
- Validate the fluid dynamics and mass transfer predictions for bubble plumes by comparing with available experimental data.

1.3. Thesis Organization

This thesis is divided into six chapters. Chapter 2 provides a review of important literature related to the objectives outlined in the previous section. This includes methods that are currently used to model dispersed gas-liquid flows, closure models for the interphase momentum exchange terms, and methods for the prediction of dispersed phase mass transfer. Chapter 3 outlines the solver development, including the mathematical formulation of the hybrid LPT-VOF model and the algorithm for code implementation. Chapter 3 also contains results from the small-scale verification cases. Chapter 4 contains the fluid dynamics validation of model predictions using experimental data for a small-scale bubble plume injected vertically into a cylindrical tank (Simiano, 2005). Chapter 4 also includes the fluid dynamics validation of the model by comparing to the simulation works of Dhotre and Smith (2007) and Dhotre et al. (2009). Chapter 5 contains the fluid dynamics and mass transfer validation of model predictions using small-scale experimental data for aeration through horizontal injection of a two-phase air-water jet into a liquid in a rectangular tank (Park and Yang, 2017). This chapter also includes the fluid dynamics validation of predictions using experimental data for a large-scale bubble plume injected vertically into a large reservoir (Milgram, 1983). Chapter 6 summarizes the conclusions and recommendations of this work.

1.4. Significance of the Current Work

The new contributions resulting from this work are as follows:

1. The coupling of the compressible VOF solver to the LPT library within OpenFOAM.
2. Modification of the VOF solver to include species transport.
3. Modification of the LPT library to include
    a) compressibility effects on bubble size and density;

b) suitable momentum closure models for bubbly flow;
c) an algorithm to solve the species equation for bubbly flow; and
d) suitable closure models for gas dissolution.

4. Verification of the implemented solver using several theoretical test cases.
5. Validation of the hybrid LPT-VOF solver for three cases involving horizontally- and vertically-injected bubble plumes with and without gas dissolution.

Chapter 2: Literature Review

2.1. Introduction

Multiphase flows have complex and varied interphase phenomena that strongly impact the hydrodynamics because many flow types can occur: gas-liquid, liquid-liquid, gas-solid, and gas-liquid-solid. Further complications arise because many flow regimes are possible, such as jet flow, slug flow, churn-turbulent flow, bubbly flow, and many others. Each of these flow regimes has different length scale characteristics, and the transition between flow regimes can mean that a single flow scenario can cover a variety of relevant length scales. Some regimes (e.g., slug flow or jetting) are effectively segregated and better considered as two separate continuous phases with coupling at an interface, while others are best represented as a continuous and dispersed phase because one phase exists as small discrete phase pockets (bubbles, droplets, particles) in the other phase. Both approaches rely on different formulations of the governing equations.

Although there are technical difficulties associated with multiphase CFD, such as high computational costs and the availability of closure models for all situations, it is often desirable to perform such simulations to gain insight into physical systems. CFD methodologies allow for the study of the governing equations directly, meaning fewer components need to be modelled by closure terms or assumed profiles. As stated by Van Wachem and Almstedt (2003), CFD has become technically viable in the past 50 years and significant efforts were made to solve multiphase flows. Anderson and Jackson (1967) derived the continuum equations of motion for gas-particle flow. Garg et al. (1975, 1978) performed impressive computations based on governing equations by Anderson and Jackson (1967) and simulated bubble behaviour in a particle bed. Many other researchers have since improved the constitutive models and performed simulations for gas-solid flows such as Boemer et al. (1997), Ding and Gidaspow (1990), Ding and Lyczkowski (1992), and Enwald et al. (1996). Ishii (1975) derived detailed governing equations for multiphase fluid-fluid flows and published appropriate models for gas-liquid flow conditions.

Multiphase CFD modelling approaches can be broadly divided into two categories: dispersed flow models and interface tracking/capturing methods. The concept of dispersed

phase models is that they use the Eulerian reference frame to describe the continuous phase and either an Eulerian or a Lagrangian reference frame to describe the dispersed phase (Dhotre et al., 2013). Interface tracking methods solve the interactions at the interface between the continuous phase and the dispersed phase by resolving the interface location directly. Resolving the interface requires a higher level of resolution, which results in more computational cells. This results directly in higher computational costs for systems with a complex interface structure (Fraga et al., 2016). Thus, interface tracking methods are not applicable for modelling large-scale bubbly flows because of the large number of bubbles in the dispersed phase.

A variety of dispersed flow models exist. Although a liquid can be dispersed in a gas (e.g., liquid sprays), the focus of this work is on gases dispersed in liquids (bubbly flows). For two-phase dispersed flow models, there are two primary approaches: the one-fluid approach and the two-fluid approach. One-fluid methods include mixture models, as per Manninen et al. (1996), and solve the volume-averaged continuity and momentum equations for the mixture of the two phases. Additionally, the dispersed phase fraction is solved based on the phase continuity equation. Two-fluid approaches include Eulerian-Eulerian (typically referred to as the two-fluid model) methods and Eulerian-Lagrangian methods. All dispersed flow models require closure terms to account for the interaction between phases. In Eulerian-Eulerian (EE) methods, dispersed phase conservation equations are ensemble averaged to obtain a set of Eulerian equations for each phase and then spatially filtered by the phase fraction in each cell. In Eulerian-Lagrangian (EL) methods, which are also known as Lagrangian particle tracking (LPT) methods, the liquid phase is treated as continuous, and Newton's second law of motion is used to track the movement of each bubble in the dispersed phase. In general, the advantages of dispersed flow models are less computational cost and resolution required compared to interface tracking methods. The primary disadvantage is that dispersed phase models require empirical closure models to include interphase exchange since this interaction is not resolved on the grid. The empirical closures work well for well-established situations, but it is sometimes difficult to find suitable relationships for complex flow regimes and transitions between flow regimes.

2.2. One-Fluid Approach (Mixture Model)

According to Ishii and Hibiki (2011), in the one-fluid approach for gas-liquid flows, the fluids in both phases are treated as one fluid in a mathematical smoothed way. Physical properties of the fluids in both phases are calculated through volume averaging in this method, which retains individual fluid properties far from the interface. The volume-averaged conservation equations for continuity, volume fraction, and momentum of the mixture are as follows (Ishii and Hibiki, 2011, ANSYS, Inc., 2009):

$$\frac{\partial \rho_m}{\partial t} + \nabla \cdot (\rho_m \vec{u}_m) = 0 \tag{2.1}$$

$$\frac{\partial}{\partial t}(\alpha_d \rho_d) + \nabla \cdot (\alpha_d \rho_d \vec{u}_m) = -\nabla \cdot \left(\alpha_d \rho_d \vec{u}_{drift,d}\right) + S_d \tag{2.2}$$

$$\frac{\partial}{\partial t}(\rho_m \vec{u}_m) + \nabla \cdot (\rho_m \vec{u}_m \vec{u}_m) = -\nabla p + \nabla \cdot \left(\mu_m (\nabla \vec{u}_m + \nabla \vec{u}_m^T)\right) + \rho_m \vec{g} + \vec{M} + \nabla \cdot \left(\sum_{i=1}^{n} \alpha_i \rho_i \vec{u}_{drift,i} \vec{u}_{drift,i}\right) \tag{2.3}$$

where ρ_m, $\vec{u}_m$, and μ_m represent the average density, velocity, and viscosity of the mixture, respectively; α_d, ρ_d, $\vec{u}_{drift,i}$, and S_d are the volume fraction, density, drift velocity, and source term of the dispersed phase, respectively; p, $\rho_m \vec{g}$, and $\vec{M}$ stand for the pressure, gravity, and volumetric body forces, respectively. The relative velocity between the continuous and dispersed phase can be calculated using a force balance on the dispersed phase.

The main advantage of the mixture model is that the formulation is simpler than the two-fluid approach, but the drawback is that some of the important characteristics of two-phase flows are lost due to the assumptions of the model (Ishii and Hibiki, 2011). According to Manninen et al. (1996), the simplicity of the mixture model is that one set of velocity components is solved based on the differential equation for the conservation of momentum and the dispersed phase velocity can be solved using the algebraic equations. The computational cost is therefore reduced. The volume fraction of the dispersed phase is solved using scalar equations with the consideration of the correction of the drift velocity in the convection term. The mixture model assumes that the motion of the dispersed bubbles is based on their terminal velocities relative to the continuous phase.

The mixture model can be applied in gas-liquid and particle-liquid flows where only relatively small bubbles and particles exist. However, it is not suitable for the gas-particle flows due to the long length scales related to the acceleration of the particles. Also, the model cannot be used if the particles and bubbles are clustered due to the increase of the drag force (Manninen et al.,1996).

2.3. Two-Fluid Approach

2.3.1. Eulerian-Eulerian Method

Both phases are treated as interpenetrating fluids in EE models. The dispersed phase is assumed to interpenetrate the continuous phase, and ensemble-averaged mass and momentum equations are used to solve for both phases. The EE method is commonly referred to as the two-fluid method.

The governing equations for two-fluid flows are shown below:

$$\frac{\partial}{\partial t}(\alpha_k \rho_k) + \nabla \cdot (\alpha_k \rho_k \vec{u}_k) = 0 \tag{2.4}$$

Eq. 2.4 is the continuity equation for both phases and the subscript k indicates the phase (i.e., k = gas, liquid), where α is the volume fraction, ρ represents the density, and u is the velocity vector. The momentum equations can be written as follows:

$$\frac{\partial}{\partial t}(\alpha_k \rho_k \vec{u}_k) + \nabla \cdot (\alpha_k \rho_k \vec{u}_k \vec{u}_k) = -\nabla \cdot (\alpha_k \tau_k) + \alpha_k \nabla P + \alpha_k \rho_k \vec{g} + \vec{M}_k \tag{2.5}$$

The terms on the left-hand side of Eq. 2.5 represent the momentum temporal rate of change and the momentum convective flux. The terms on the right-hand side represent the viscous stress, the pressure gradient, gravity/body forces, and the interphase momentum exchange (Deen et al., 2001).

EE models often have lower computational costs compared to EL methods because there is one set of conservation equations for each phase that are valid in the whole domain (Fraga et al., 2016). This makes the method suitable for large-scale industrial simulations. According to Buwa et al. (2006), there is a good agreement between EE models and experiments when predicting time-averaged flow properties and predicting the low frequency oscillations of meandering bubble plumes. Also, EE models can predict more

detailed phase specific interactions than the one-fluid model because the transfer processes of each phase are expressed using their own balance equations (Ishii and Hibiki, 2011).

Despite these advantages, EE models do not retain very much local information about the dispersed phase. Empirical relationships are needed to provide closure for the subgrid force balance and other conservation equations (Badreddine et al., 2015), and these closure laws cannot be developed based on detailed local (particle level) interactions between the phases. The EE method cannot capture the physical details of the interaction between the carrier fluid and dispersed phase. Therefore, it cannot be used to solve for turbulence scales that are close to the bubble size because the ensemble averaging limits the potential mesh refinement (Fraga et al., 2016). According to Fraga et al. (2016), with the proper non-diffusive convection schemes, EE could have the same accuracy as EL when predicting the average flow structure. However, the inability to resolve local phenomena is the primary weakness of the EE method relative to the EL technique.

Deen et al. (2001) have studied and simulated gas-liquid flow in a square cross-section bubble column using an EE approach with large eddy simulations (LES) and Reynolds-averaged Navier-Stokes (RANS) turbulence models. They found that the transient behaviour that was observed in experiments can be captured when the lift force, drag force, and virtual mass force are applied. Two turbulence models, the Smagorinsky (1963) (LES) subgrid-scale (SGS) model and the k-ε (RANS) model, were used and compared. However, the LES model was considered better than the RANS model after comparing to the experimental data. LES predicted the transient movement of the bubble plume, while the RANS model overestimated the turbulent viscosity and could only predict low frequency unsteady flow.

Dhotre and Smith (2007) have performed numerical simulations of gas-liquid flow in a tank based on the experiments conducted by Simiano (2005) using an EE approach in. It was shown that there was good agreement between the experimental data and the numerical simulations for dispersed phase fraction, axial liquid velocity, and axial gas velocity at higher measurement levels; however, there were some differences in the low plume region close to the injector. This may be caused by inadequacies in the standard k-ε turbulence

model, which needs to be explored further. The turbulent kinetic energy was overpredicted near the injector and underpredicted at higher levels. Dhotre et al. (2008) simulated gas-liquid flow in a square cross-section bubble column using the EE method with both LES and RANS turbulence models. The experimental data from Deen et al. (2001) was used for comparison with the simulations. The RANS simulation showed good agreement with the experimental data except for the axial and radial distribution of the fluctuating liquid velocity and turbulent kinetic energy near the wall. Dhotre et al. (2009) performed EE-LES for the experiments conducted by Simiano (2005). In this study, they compared their LES simulation results to the experiments for validation and to their previous work in 2007 that used a RANS model as the turbulence model. It was found that both approaches showed good agreement compared to the experimental data except near the injector. EE-LES showed better performance when capturing the turbulent kinetic energy than the k-ε model at higher elevations.

The key challenge in the simulation of bubbly flows is to find appropriate interphase momentum exchange models and turbulence models that provide good agreement with published experimental studies. Table 2.1 summarizes the coupling closure models, turbulence models, and modifications on the source terms in some recent studies. The table is not intended to be comprehensive, but it is intended to provide a snapshot of some commonly used approaches in recent literature.

2.3.2. Eulerian-Lagrangian Method

In EL models, the continuous phase can be modelled using volume-averaged mass and momentum equations, which is the same as in the Eulerian framework. Newton's second law of motion is used to track the displacement of the dispersed phase, which is the Lagrangian framework. Empirical correlations are used to model the forces acting on each individual bubble. Additionally, the momentum equation should include the equivalent force of the bubbles acting on their surroundings (Hu and Celik, 2008). In bubbly flows, each bubble is treated as a Lagrangian point that moves across the Eulerian mesh (Fraga et al., 2016), and it must therefore be tracked on the computational grid. The bubble trajectories are time averaged to obtain predictions at steady state (Rafique et al., 2004).

EL models include bubble dynamics and liquid phase hydrodynamics. Bubble dynamics consists of quantifying the force balance acting on the bubbles. Typically, this includes the drag, lift, virtual mass, buoyancy, and gravity forces. These forces will be discussed in section 2.4. The governing equations for the liquid phase are the same as for the EE model. However, in EL models, only the liquid phase is described by the Eulerian framework. Therefore, the subscript k in Eqs. 2.4 and 2.5 would be just l, which stands for the liquid phase. For the gas phase, each gas bubble is tracked in the Lagrangian frame, which uses Newton's equation of motion to calculate the trajectory and the velocity of each gas bubble (Gruber et al., 2013).

$$\Delta x_b = \vec{u}_b \Delta t \tag{2.6}$$

$$\rho_b V_b \Delta \vec{u}_b = \Delta t \sum F \tag{2.7}$$

where Δx_b, $\vec{u}_b$, Δt, ρ_b, V_b, and $\sum F$ represent the position change of the bubble in one time step, the velocity of the bubble, time step, the density of gas, the bubble volume, and the forces acting on the bubble, respectively.

According to Buwa et al. (2006), the challenges that are encountered in the numerical implementation of EL models include the forces acting on bubbles, coupling of the interphase exchange between the dispersed phase and the continuous phase, and bubble trajectory prediction in turbulent flows and turbulence models especially bubble-induced turbulence. A summary of the closure models and the turbulence models used in recent studies of the EL approach can be seen in Table 2.1.

Buwa et al. (2006) simulated a three-dimensional unsteady gas-liquid flow using an EL approach in a rectangular bubble column to study the dynamics of bubble plumes. The effects of aerated liquid height to column width ratio and superficial gas velocity were investigated. Drag, gravity, buoyancy, lift, virtual mass, and turbulent dispersion force were included in their computational model. For the turbulence model, the standard k-ε model with the source terms for k and ε that are suggested by Lain et al. (2002) was used to obtain better agreement between the simulation and the experiment.

Fraga et al. (2016) simulated the dynamics of a bubble plume in a cubic tank using the EL approach with a LES turbulence model. The tank contained quiescent water initially. They

introduced a novel interpolation method that employed second-order smoothed delta functions when coupling the liquid and gas phases. Their results showed good agreement when compared to the experimental data; however, their model underpredicted the fluctuations of the streamwise turbulence in the core of the bubble plume. They concluded that the EL model may have limitations on capturing small turbulence scales when a given mesh resolution is exceeded. They also suggested that the bubble-induced turbulence should be further investigated in the LES subgrid-scale models.

Van Wachem and Almstedt (2003) introduced two models for fluid-solid flows that employed the Lagrangian framework: the hard-sphere approach and the soft-sphere approach. In the hard-sphere approach, the particles are assumed to be rigid spheres and the collisions of particles are assumed to be instantaneous and binary. Although this model works well in dilute flows, as the concentration of particles increases, the likelihood that particle collisions are exclusively binary decreases. To calculate the larger particles that are formed by collision, linear and angular momentum balances are considered. The energy released during collisions has a large effect on rebound; therefore, restitution coefficients of the tangential and normal velocity components at the contact point were also considered. This hard-sphere model can be used for particle-particle collisions and particle-wall collisions.

Another approach that is commonly used in the Lagrangian framework is called soft-sphere approach, where particles can interact and overlap. This approach can be modelled using the slider-spring-dashpot method, with associated damping, spring, and friction coefficients. However, the equations become stiff and hard to solve numerically when physically realistic values for the coefficients are chosen. In the soft-sphere model, a potential force is used to model the interactions of particles. Two particles deform during the collision. The driving force in this model is the degree of overlap between the two particles., which increases the repulsive force with increasing overlap displacement. A frictional force occurs when two particles slide under a normal force. The effect of deformation is simulated by the spring, the effect of the damping is simulated by the dashpot, and the friction slider simulates the sliding force of the two particles.

The spring-dashpot system can be utilized to model the collisions between bubbles and the contact time of bubbles in bubbly flow (Xue et al., 2017). Xue et al. (2017) stated that the hard-sphere model that was used to simulate the bubble-bubble interactions in previous research had limitations on the bubble contact time. The bubble contact time cannot be taken into account directly in the collision model during the collision processes. They used the Deen et al. (2001) study to validate bubble coalescence using the spring-dashpot model. They included the buoyancy, gravity, drag, lift, and virtual mass forces. They used the Tomiyama et al. (1998) drag model, as well as a constant coefficient of 0.5 for both the lift and virtual mass forces. They considered the spring-dashpot model as the collision model, coalescence model, and break-up model in their simulations to record the bubble contact time accurately. They compared their results with the coalescence model and break-up model on and off (the collision model was always on) with the experimental data from Deen et al. (2001). The results showed that model agreement was improved if the coalescence and break-up models were turned off. They concluded that the parameters in the spring-dashpot model, coalescence model, and break-up model play an important role in the simulations and that those parameters should be determined by direct numerical simulations or the micro-scale experiments. The coefficients in the spring-dashpot model, coalescence model, and break-up model, as well as the numerical algorithms in the detection of the collision and the record method of the contact time, should be further studied in the future.

Table 2.1: Summary of the Coupling Closure Models and Turbulence Models in Recent Studies for EE and EL Methods

Reference	Model	Geometry
Deen et al. (2001)	C_D: Ishii and Zuber (1975) C_L: 0.5 C_{VM}: 0.5 C_{TD}: N/A Turbulence: RANS: k-ε LES: Smagorinsky (1963) SGS model Bubble-induced turbulence: Sato and Sekoguchi (1975)	Square bubble column
Dhotre and Smith (2007)	C_D: 0.44 C_L: 0.1 C_{VM}: 0.5 C_{TD}: Davidson (1990) Turbulence: RANS (k-ε) with the source terms from Simonin and Viollet (1988) Bubble-induced turbulence: Sato et al. (1981)	Cylindrical tank (bubble plume)
Dhotre et al. (2008)	C_D: Ishii and Zuber (1975) C_L: 0.5 C_{VM}: 0.5 C_{TD}: 0.2 Turbulence: RANS: k-ε with the source terms from Simonin and Viollet (1988) LES: Smagorinsky (1963) SGS model Bubble-induced turbulence: Sato et al. (1981)	Square bubble column
Dhotre et al. (2009)	C_D: 0.44 C_L: 0.5 C_{VM}: 0.5 C_{TD}: N/A Turbulence: LES with Smagorinsky (1963) SGS model Bubble-induced turbulence: Sato et al. (1981)	Cylindrical tank (bubble plume)
Buwa et al. (2006)	C_D: Tsuchiya et al. (1997) C_L: Tomiyama et al. (2002) C_{VM}: 0.5 C_{TD}: Gosman and Ioannides (1983) Turbulence: RANS (k-ε) Bubble-induced turbulence: N/A	Rectangular bubble column
Fraga et al. (2016)	C_D: Clift (1978) C_L: 0.53 C_{VM}: 0.5 C_{TD}: N/A Turbulence: LES with Smagorinsky (1963) SGS model Bubble-induced turbulence: N/A	Cubic water tank (bubble plume)
Xue et al. (2007)	C_D: Tomiyama et al. (1998) C_L: 0.5 C_{VM}: 0.5 C_{TD}: N/A Turbulence: LES with Smagorinsky (1963) SGS model Bubble-induced turbulence: N/A	Square bubble column

2.4. Interphase Momentum Exchange

The forces that act on the bubbles that play an important role in the coupling between the continuous and dispersed phases can be divided into two categories: established forces and non-established forces. The expressions of the forces acting on bubbles in both the EE and EL models are described below. The force balance on a particle can be written as follows:

$$m_d \frac{d\vec{u}_d}{dt} = \sum F \tag{2.8}$$

where $\vec{u}_d$ is the velocity of the dispersed phase element, m_d is the mass of dispersed phase, and F is the total force acting on the particle. The interphase momentum exchange term in Eq. 2.5, where V_{cell} is the computational cell volume, can be calculated using the following expression (Asad et al., 2017):

$$M = -\frac{1}{V_{cell}} \sum F \tag{2.9}$$

On the right-hand side of Eq. 2.5, the interfacial forces acting on the particle usually include the buoyancy, gravity, drag, lift, virtual mass, and turbulent dispersion forces.

The established forces refer to the forces that are fundamental in nature, for which formulations do not change often in literature. These forces include gravity, buoyancy, and virtual mass. The buoyancy force, F_B, and gravity, F_G, can be calculated as follows:

$$F_B + F_G = \frac{(\rho_b - \rho_l)\pi d_b^3 \vec{g}}{6} \tag{2.10}$$

where ρ_l is the density of the liquid, ρ_b is the density of the bubble, d_b is the diameter of the gas bubble, and $\vec{g}$ is acceleration due to gravity.

The virtual mass force is akin to the drag force on the bubbles due to the difference in acceleration between the gas and liquid phases. It can be represented as follows (Chuang and Hibiki, 2017; Asad et al., 2017):

$$F_{VM} = -C_{VM}\rho_l V_b \left(\frac{D\vec{u}_b}{Dt} - \frac{D\vec{u}_l}{Dt}\right) \tag{2.11}$$

where F_{VM} is the virtual mass force, C_{VM} is the virtual mass coefficient, and $\vec{u}_l$ is the liquid velocity. Typically, a constant coefficient value of 0.5 is used in the literature reviewed.

The non-established forces, on the other hand, refer to the forces whose coefficients or formulation vary significantly with the type of application. Drag, lift, and turbulent dispersion forces fall into this category. The drag force acts as a resistance to bubble motion and can be defined using the following expression (Chuang and Hibiki, 2017):

$$F_D = \frac{1}{2} C_D \rho_l A_p |\vec{u}_b - \vec{u}_l| (\vec{u}_b - \vec{u}_l) \tag{2.12}$$

where F_D is the drag force, C_D is the drag coefficient, and A_p is the projected area of particle.

Tomiyama et al. (1998) developed a drag model for bubbles with clean surfaces, slightly contaminated interfaces, and contaminated interfaces.

The model for clean interfaces is as follows:

$$C_D = \max\left(min\left(\frac{16}{Re_\infty}(1 + 0.15Re_\infty^{0.678}), \frac{48}{Re_\infty}\right), \frac{8}{3}\frac{E\ddot{o}}{E\ddot{o}+4}\right) \tag{2.13}$$

The model for slightly contaminated interfaces is as follows:

$$C_D = \max\left(min\left(\frac{24}{Re_\infty}(1 + 0.15Re_\infty^{0.678}), \frac{72}{Re_\infty}\right), \frac{8}{3}\frac{E\ddot{o}}{E\ddot{o}+4}\right) \tag{2.14}$$

The model for contaminated interfaces is as follows:

$$C_D = \max\left(\frac{24}{Re_\infty}(1 + 0.15Re_\infty^{0.678}), \frac{8}{3}\frac{E\ddot{o}}{E\ddot{o}+4}\right) \tag{2.15}$$

$$Re_\infty = \frac{\rho_l |\vec{u}_b - \vec{u}_l|_\infty \, d_b}{\mu_m} \tag{2.16}$$

$$E\ddot{o} = \frac{\vec{g}\Delta\rho d_b{}^2}{\sigma_{ST}} \tag{2.17}$$

where the single-bubble Reynolds number (Re_∞) is given by Eq. 2.16, $|u_b - u_l|_\infty$ is the relative velocity between liquid phase and single bubble, and the Eötvös number ($E\ddot{o}$) is given by Eq. 2.17.

It is necessary to carefully consider the effect of the dispersed phase volume fraction on the drag coefficient when applying Tomiyama's model for multi-bubble systems. According to Chuang and Hibiki (2017), Tomiyama's drag model is valid for $10^{-2} < E\ddot{o} < 10^3$ and $10^{-3} < Re < 10^5$.

Tsuji et al. (1982) included a correction for the interaction of the bubbles at higher volume fractions:

$$C_{D,corrected} = C_D \left(1 - \left(\frac{3\alpha}{\pi}\right)^{\frac{2}{3}}\right) \tag{2.18}$$

where C_D is the drag coefficient from a suitable single-bubble drag coefficient correlation.

Roghair et al. (2011) developed a drag model to include the effect of bubble swarms:

$$\frac{C_{D,Roghair}}{C_{D,\infty}(1-\alpha_{local})} = 1 + \left(\frac{18}{E\ddot{o}}\right)\alpha_{local} \tag{2.19}$$

where α_{local} is the local volume fraction, which is calculated instantaneously for every computational cell during the simulation. $C_{D,\infty}$ can be calculated using the following equation:

$$C_{D,\infty} = \sqrt{C_D(Re_b)^2 + C_D(E\ddot{o})^2} \tag{2.20}$$

and

$$C_D(Re_b) = \frac{16}{Re_b}\left(1 + \frac{2}{1+\frac{16}{Re_b}+\frac{3.315}{\sqrt{Re_b}}}\right) \tag{2.21}$$

$$C_D(E\ddot{o}) = \frac{4E\ddot{o}}{E\ddot{o}+9.5} \tag{2.22}$$

The lift force acts on a bubble in the lateral direction. F_L is the shear-induced lift force for the bubble and can be expressed as follows (Asad et al., 2017):

$$F_L = -C_L\rho_l V_b(\vec{u}_b - \vec{u}_l) \times (\nabla \times \vec{u}_l) \tag{2.23}$$

where C_L is the coefficient for the shear-induced lift force. The lift coefficient is positive for spherical bubbles and the lift force acts in the direction of decreasing liquid velocity. Therefore, it usually acts laterally and to disperse the plume.

Tomiyama et al. (2002) stated that the lift coefficient can be negative and in this case the force would act in the direction of increasing liquid velocity due to the substantial deformation of bubbles. According to the model of Tomiyama et al. (2002), the lift coefficient is calculated using the following expression:

$$C_L = \begin{cases} \min\left(0.288 + tanh(0.121Re_b), f(E\ddot{o}_d)\right); & E\ddot{o}_d < 4 \\ f(E\ddot{o}_d); & 4 \le E\ddot{o}_d \le 10.7 \\ -0.27; & E\ddot{o}_d > 10 \end{cases} \quad (2.24)$$

where

$$E\ddot{o}_d = \frac{E\ddot{o}}{E^{2/3}} \; and \; E = (1 + 0.163E\ddot{o}^{0.757})^{-1} \quad (2.25)$$

$$f(E\ddot{o}) = 0.00105E\ddot{o}_d^3 - 0.00159E\ddot{o}_d^2 - 0.0204E\ddot{o}_{\mathrm{d}} + 0.474 \quad (2.26)$$

The turbulent dispersion force is caused by the fluctuating component of the forces acting on bubbles. Lopez de Bertodano (1992) developed a turbulent dispersion force model in which they assumed that the motion of bubbles is proportional to the phase fraction gradient.

$$F_{TD} = -C_{TD}V_b\rho_l\, k_l\, \nabla\alpha_b \quad (2.27)$$

where k_l is the turbulent kinetic energy of liquid phase, and C_{TD} is the turbulent dispersion coefficient, which has a recommended value between 0.1 and 0.5.

Gosman and Ioannides (1983) developed a turbulent dispersion force model for particles to estimate the liquid fluctuation velocity. This model is commonly called the discrete random walk (DRW) model or the eddy lifetime model. In this model, the liquid fluctuation velocity is added to the mean liquid velocity. The eddy is calculated using the Gaussian distributed random velocity fluctuations in the *x*, *y*, and *z* directions and the eddy life time. The standard deviation, σ_{sd}, can be calculated as follows:

$$\sigma_{sd} = \sqrt{\frac{2k}{3}} \quad (2.28)$$

where *k* is the turbulent kinetic energy. The dissipation length scale, l_e, can be obtained using the following expression:

$$l_e = \frac{C_\mu^{\frac{1}{2}} k^{\frac{3}{2}}}{\varepsilon} \quad (2.29)$$

where $C_\mu = 0.09$ and ε is the turbulent dissipation rate. The eddy life time can be calculated by the division of the dissipation length scale and the magnitude of the liquid fluctuation velocity.

2.5. Hybrid Methods

Since dispersed flow models typically cannot model the gas-liquid free surface without modification, hybrid approaches that combine the LPT and the VOF model have been developed to simulate free surface motion in dispersed flows. This hybrid method uses LPT to model the bubbly flows in the liquid phase and only uses VOF method to simulate the free surface.

Jain et al. (2014) have studied a hybrid approach of the VOF method and the Discrete Bubble Model (VOF-DBM) to simulate free surface in bubble column. VOF is used to simulate the free surface and the DBM, which is a form of LPT model, is used to track the hydrodynamics of the dispersed bubbles. They found that the coalescence calibration factor and the critical Weber number can be optimized by considering the bubble coalescence and breakup, respectively. They also found that the bubble coalescence occurs mainly in the region near the injector and the bubble breakup happens near the interface. Their model was compared with the experimental liquid particle image velocimetry (PIV) results from Deen et al. (2001). Their results showed that the model was not sensitive enough to predict the coalescence calibration factor value and a more realistic size distribution of the inlet bubble could have improved the quality of the results.

Asad et al. (2017) also used the LPT-VOF approach in their studies. They applied the LPT method to track the bubbles and the VOF method to simulate the gas-liquid interface in the bubble column using OpenFOAM. They used the Deen et al. (2001) case as the basis for their simulations. The purposes of their studies were to investigate the inlet conditions and to compare three different drag models: Tomiyama et al. (1998) model, Ishii and Zuber (1975) model, and Roghair et al. (2011) model. They used Tomiyama et al. (2002) as the lift model and 0.5 as the coefficient of the virtual mass force. The buoyancy force and gravity were also included. The Spalart-Allmaras delayed detached eddy simulation (SpalartAllmarasDDES) (Spalart et al., 2006) model, which is one of the LES models, was used in their model as the turbulence model. They also implemented the bubble removal technique, which removes the bubbles when they reach the free surface in the bubble column. They concluded that the Roghair et al. (2011) drag model gave better agreement with the experimental data, and that the bubble size distribution as well as the bubble

injection rate play an important role when predicting the flow behavior and the mean velocities for both the bubbles and the liquid phase. They also mentioned that bubble-induced turbulence and lift force should be investigated further.

Skjetne and Olsen (2012) used the Discrete Phase Model (DPM) coupled with a VOF solver to model bubble plume releases from five different depths. They also included methane gas dissolution in their model. They found that the rise velocity of the bubble plume decreases with increasing depth of release. They also conclude that the plume dynamics are significantly affected by gas dissolution and most of the gas will be dissolved for the plumes that are released at deep depths. Olsen and Skjetne (2016) used the geometry from Milgram (1983) to simulate bubble plumes with four different gas injection rates. They included gravity, buoyancy, virtual mass, turbulent dispersion, gas expansion, and gas dissolution in their simulation. The turbulence model they used in this paper was the standard k-ε model. They stated that the lift force has no effect in bubble plumes and that is the reason why they did not include the lift force in their simulations. The main reasons that cause the change of bubble size in dense plumes are breakup and coalescence due to turbulence, while gas expansion due to the pressure gradient and gas dissolution are dominant in dilute plumes. They used the model that was developed by Laux and Johansen (1999) as their bubble size model. They concluded that the consistency between their model and the experimental results is quite good. However, their model underpredicted the spreading of the bubble plume and the reasons for this difference could be the choice of the turbulence model and that bubble-induced turbulence was neglected in their model. They also stated that the choice of the correlation for the mass transfer coefficient is important to predict the gas dissolution in the bubble plume, and the correlations for contaminated systems seem to be more suitable for the bubble plumes. Olsen et al. (2017) simulated the bubble plumes using another turbulence model called very large eddy simulation (VLES) instead of the standard k- ε model. The VLES simulations underpredicted the spreading of the bubble plume, which could be because the bubble-induced turbulence and the lift force were neglected in their model.

2.6. Mass Transfer

Mass transfer between the continuous and dispersed phases is another important part of dispersed multiphase flows. Since the mass transfer occurs below grid resolution, dispersed phase mass transfer is modelled using empirical relationships for the overall mass transfer coefficient. However, the mass transfer coefficient depends on the resistances on both sides of the interface and also requires a jump condition to be specified at the phase boundary due to differences in solubility. Although diffusion and advection from the interface occurs on both sides, the rate of gas diffusion is higher. Therefore, the liquid side resistance is often more important (Olsen et al., 2017) in gas dissolution. Therefore, the overall mass transfer coefficient is usually based on the liquid side mass transfer coefficient. The governing equation of the mass transfer of species *i* from a bubble to the surrounding water can be written as follows (Ranz and Marshall, 1952):

$$\dot{m}_{b,i}^{j} = A_b J_i^j = \pi d_b^2 k_l^j (C_{l,i}^{j,sol} - C_{l,i}^{j}) \tag{2.32}$$

where d_b, k_l^j, $C_{l,i}^{j,sol}$, and $C_{l,i}^{j}$ are the bubble diameter, mass transfer coefficient, the solubility, and the concentration of species *i* in the surrounding liquid, respectively. *j* denotes the parcel number in a computational cell.

For an ideal gas mixture, Henry's law can be applied, and Eq. 2.32 can be rewritten as follows (Darmana et al., 2005):

$$\dot{m}_{b,i}^{j} = \pi d_b^2 k_l^j \rho_l (Y_{l,i}^{j*} - Y_{l,i}^{j}) \tag{2.33}$$

$$Y_{l,i}^{j*} = H_i Y_{b,i}^{j} \frac{\rho_b}{\rho_l} \tag{2.34}$$

where $Y_{l,i}^{j*}$, $Y_{l,i}^{j}$, H_i, and $Y_{b,i}^{j}$ are the solubility of species *i* in the surrounding liquid, the mass fraction of species *i* in the surrounding liquid, the Henry's law constant for species *i* in dimensionless form, and mass fraction of species *i* in the bubble, respectively. As stated earlier, *j* represents the parcel number in a computational cell.

There are many correlations for the mass transfer coefficient, including for different flow regimes and levels of interface contamination.

The Higbie (1935) model for clean systems:

$$k_l^j = \frac{2}{\sqrt{\pi}}\sqrt{ReSc}\,\frac{D_{ab}}{d_b} \tag{2.35}$$

The Clift (1978) model for partly contaminated systems:

$$k_l^j = \frac{2}{\sqrt{\pi}}\sqrt{1 - \frac{2.89}{max(2.89,\sqrt{Re})}}\,Re^{1/2}Sc^{1/2}\,\frac{D_{ab}}{d_b} \tag{2.36}$$

The Bird et al. (1960) model for contaminated systems:

$$k_l^j = \sqrt{4 + 1.21Re^{2/3}Sc^{2/3}}\,\frac{D_{ab}}{d_b} \tag{2.37}$$

The Hughmark (1967) model for contaminated systems:

$$k_l^j = (2 + 0.95Re^{1/2}Sc^{1/3})\,\frac{D_{ab}}{d_b} \tag{2.38}$$

The Frössling (1938) model for contaminated systems:

$$k_l^j = 0.6\sqrt{u_b/d_b}\,D_{ab}^{2/3}(\mu/\rho)^{-1/6} \tag{2.39}$$

where D_{ab} is the mass diffusivity between species *a* and the mixture *b* in the equations above.

2.7. Summary and Conclusions

In this chapter, approaches for the simulation of two-phase gas-liquid bubbly flows were reviewed. These approaches include mixture models, Eulerian-Eulerian methods, Eulerian-Lagrangian methods, and hybrid methods. Each approach has advantages and disadvantages. The mixture models are not suitable for modelling bubbly flows that have large bubble clusters in the system due to the simplicity of the formulation, but they are the least computationally demanding. EE methods have shown good agreement between predictions and experiments when time-averaged flow properties and the low frequency oscillations of meandering bubble plumes are analyzed. However, EE models cannot provide local information about the interactions between the dispersed and continuous phases. Therefore, empirical closure models cannot be developed based on particle-scale information. Conversely, EL models give detailed information for the positions, velocities, and forces for each individual bubble. Therefore, it is relatively easier to account for particle size distributions because each particle only has one motion equation. In gas-liquid flows, bubble-bubble interactions and bubble-induced turbulence can be added more

realistically using EL models because of the available local information. Other closure models can also use more of the available local information. The main disadvantage of the EL method is the computational cost when a very large number of bubbles must be simulated. However, it is often possible to combine the motion of groups of bubbles into parcels to reduce the number of equations that need to be solved.

In this study, a hybrid LPT-VOF approach is used to simulate bubble plumes because LPT is suitable to track individual bubbles in the liquid phase, while the effects of the free surface can be modelled by VOF. Gas dissolution is also included in the proposed study to investigate transfer into and out of the bubbles in the water. The LPT-VOF method provides a scalable algorithm for modelling bubble plumes. The main weakness is that the method implemented in this study only permits transition from LPT to VOF and not from VOF to LPT. This means that the model could not be used to predict the bubbles generated from the breakup of a gas jet in a liquid. Although it would be possible to implement such an algorithm, the implementation of VOF to LPT transition modelling was considered to be outside the scope of this study.

Chapter 3: Solver Development and Verifications

3.1. Introduction

This chapter describes the development of the LPT-VOF solver. It also summarizes the verification cases used to test the adjustments made in the fluid dynamics and mass transfer models. The discussion starts with an overview of the solver algorithm, with a flowchart provided to illustrate the structure of the solution procedure. Then, the process of evolving the dispersed phase using Lagrangian particle tracking (LPT) is discussed. Subsequently, the derivations of the phase continuity, pressure, species, and momentum equations for the volume-of fluid (VOF) method are discussed, along with a description of the coupling to the LPT model. Coupling between the continuous phase and the dispersed phase is achieved by correcting the continuous phase fraction and including interphase exchange sources in the phase continuity, pressure, species, and momentum equations. Finally, two simple cases were simulated to verify the implementation of the mass transfer model. The first case was a single stationary bubble positioned in the middle of a box with the water flowing slowly in the upward direction, while the second case was a single bubble rising from the central bottom of a box with stationary water in the box.

3.2. Algorithm Overview

A coupled LPT-VOF solver was developed in OpenFOAM. Figure 3.1 shows the algorithm of the developed solver, which is based on OpenFOAM's `compressibleInterFoam` solver and the pre-existing Lagrangian library. Modifications were made to the solver and the Lagragian library to facilitate coupling. The Lagrangian library was extended to model gas bubble dissolution and the motion of compressible gas bubbles.

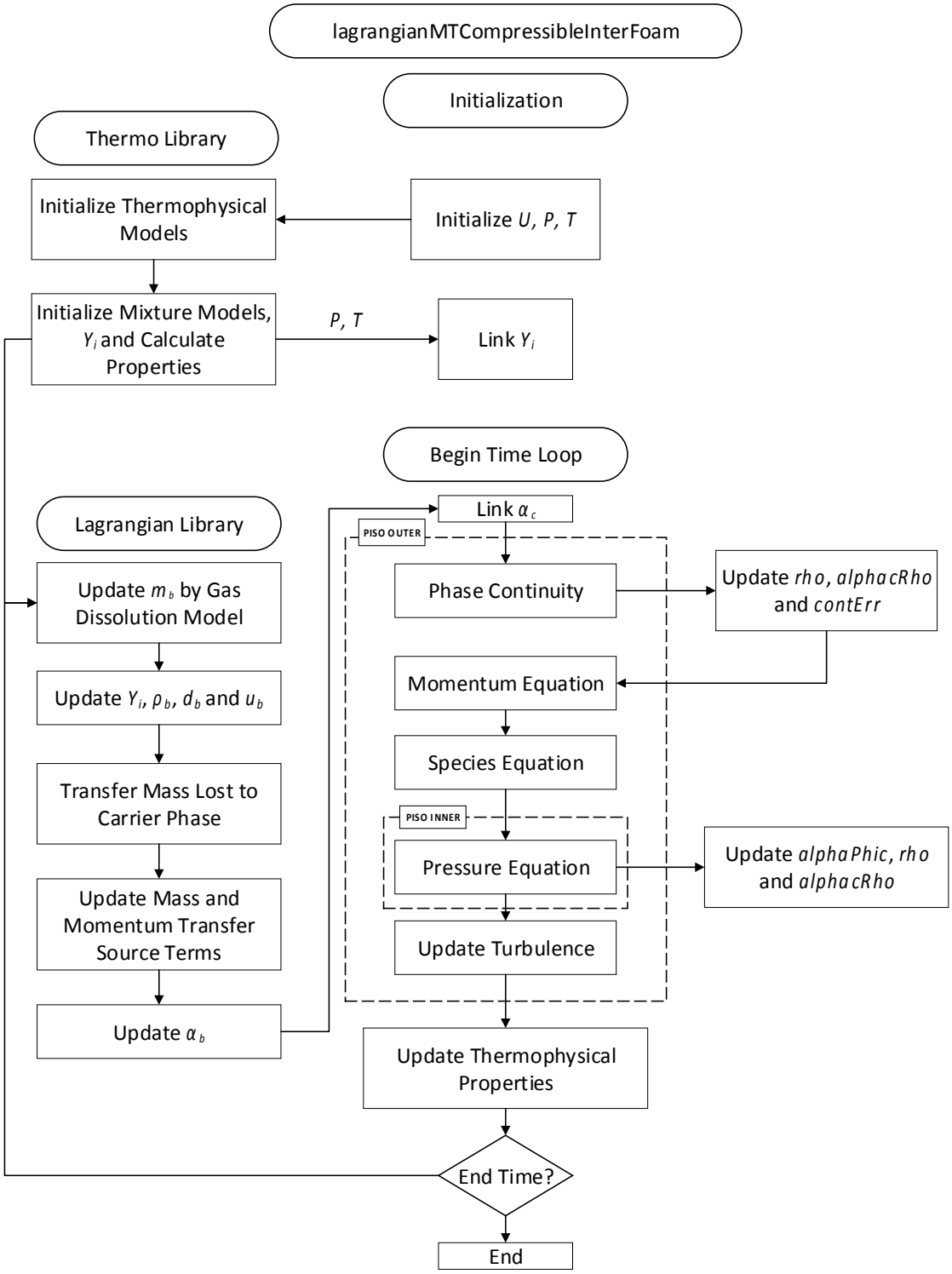

Figure 3.1: Overall algorithm of `lagrangianMTCompressibleInterFoam`.

The velocity is read from the case directory, and the thermophysical library is created. This generates the pressure and temperature fields based on the user inputs in the case directory.

The mass fractions of all species, $Y_{i,}$ are created by the generation of the chosen mixture model in the thermophysical library. The Lagrangian library is created, which also generates the field variables to track the dispersed phase volume fraction on the Eulerian grid. When the time loop begins, the Lagrangian library is evolved first to update the amount of bubbles injected into the system. Subsequently, the impact of bulk fluid motion and the force balance are used to estimate the final position of the tracked particles. The size and shape of the bubbles are updated based on the background pressure and mass transfer rates, which are then calculated for the next time step. The results of the force balance and mass transfer are passed, via volumetric source terms stored on the Eulerian grid, to the VOF algorithm.

The VOF solver implements OpenFOAM's PIMPLE algorithm, which combines the pressure-implicit with splitting of operators (PISO) method and the semi-implicit momentum linked equations (SIMPLE) methods. Once the continuous phase fraction is known, the phase continuity equation can be solved. Subsequently, the total density of phases 1 and 2 (`rho`), the density of the continuous phase (`alphacRho`), and the continuity error (`contErr`) can be updated. After the update, the momentum equation, species equations, and pressure equation are solved inside the PISO loop. At the end of the pressure equation, the velocity of the continuous phase at the face (`alphaPhic`), the total density of phases 1 and 2 (`rho`), and the density of the continuous phase (`alphacRho`) are updated. The turbulence parameters are updated at the end of the PISO loop. For extra stability, the PISO loop can be repeated within each time step to achieve better convergence, which is similar to the SIMPLE method. The thermophysical properties are updated based on the updated density in the pressure equation. In this study, the temperature effect was not included for the thermophysical properties update and the energy equation was not included in the solver because only approximately isothermal conditions were considered in the validation cases. Following the PISO loop, if the end time is reached, the solver stops; if not, time is incremented based on the specified time step. The PISO outer loop includes the phase continuity, momentum, species, and pressure equations, while the PISO inner loop only contains the pressure equation. The number of

correctors for the inner and outer PISO loops can be specified to achieve the desired level of convergence within each time step.

3.3. Bubble Properties Calculations

Figure 3.2 shows the illustration of the phase fractions in the system. Eqs. 3.1 through 3.3 describe the relationships of the phase fractions in the system. α_b and α_c represent the bubble/Lagrangian phase fraction and the continuous phase fraction, respectively. α_1 and α_2 are the liquid phase fraction and the gas phase fraction in the VOF algorithm, respectively. α_c is introduced in this case to correct the units of α_1 and α_2. Typically, α_1 and α_2 in the VOF method are phase fractions with units of m^3 of phase *i* (e.g., gas) per m^3 total. However, since the VOF method may not occupy the entire cell volume when a Lagrangian bubble is present, they have units of m^3 of phase *i* per m^3 occupied by the continuous phase. α_c has units of m^3 occupied by the continuous phase per m^3 total. Thus, after multiplying by α_c, the units of the gas phase fraction and the liquid phase fraction are back to the normal units used in the VOF method. The relationships of phase fractions in the system are shown as Eq. 3.1. This equation remains consistent with Eq. 3.3 because the phase fractions in the VOF method should be sum to one (Eq. 3.2), which makes sense because there is only one continuous phase and one dispersed phase in the whole system.

$$\alpha_b + \alpha_c(\alpha_1 + \alpha_2) = 1 \tag{3.1}$$

$$\alpha_1 + \alpha_2 = 1 \tag{3.2}$$

$$\alpha_b + \alpha_c = 1 \tag{3.3}$$

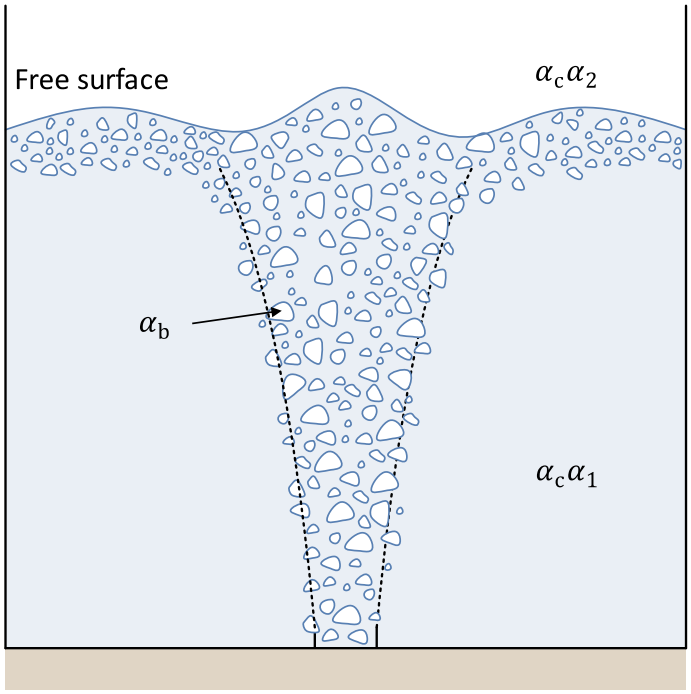

Figure 3.2: Illustration of the different definitions of phase volume fraction in a bubble plume.

In LPT, the change of the mass of the bubble, Δm_b, due to mass transfer can be calculated using the following equation:

$$\frac{dm_b^j}{dt} = \sum_i A_b k_l^j \rho_l (H_i Y_{b,i}^j \frac{\rho_b}{\rho_l} - Y_{l,i}^j) \tag{3.4}$$

This equation can be solved using any technique for solving ordinary differential equations, but Euler's method is commonly used.

The mass fraction for species *i* in the bubble can be updated using the following expression:

$$Y_{b,i}^j = \frac{\Delta m_{b,i}^j}{\sum_i \Delta m_{b,i}^j} \tag{3.5}$$

where $\Delta m_{b,i}^j$ represents the mass change for species *i* in bubble (or parcel) *j* and $\sum_i \Delta m_{b,i}^j$ is the sum of the mass change for all the species in bubble (or parcel) *j*.

In OpenFOAM, the default implementation of the Lagrangian library assumes constant bubble size in incompressible flow conditions. However, for compressible systems, the

density of the gas phase will change with pressure (and temperature), meaning that the diameter will change based on the internal pressure as a result.

From the ideal gas law, the density of the gas bubble can be calculated as follows:

$$\rho_b = \frac{p_c W}{R T_c} \tag{3.6}$$

where p_c and T_c are the pressure and temperature of the carrier phase, W is the molecular weight of gas mixture in the bubble, and R is the universal gas constant.

The diameter of the gas bubble can be calculated using the updated mass and density as follows:

$$d_b = \sqrt[3]{\frac{6m_b}{\pi \rho_b}} \tag{3.7}$$

The velocity of the bubble can be calculated and updated by Newton's equation of motion:

$$\frac{du_b}{dt} = \frac{\sum F}{m_b} \tag{3.8}$$

The gas volume fraction, α_b, can be calculated by taking the ratio of the total gas volume in a computational cell (number of bubbles times the volume of a bubble) and the volume of the computational cell. Then, the continuous phase fraction can be easily calculated since they must both sum to one.

3.4. Phase Fraction Conservation Equation (VOF)

The phase fraction conservation equations for phases 1 and 2 (1 – liquid and 2 – gas) tracked by the VOF solver are shown below:

$$\frac{\partial(\rho_1 \alpha_1 \alpha_c)}{\partial t} + \nabla \cdot (\rho_1 \alpha_1 \alpha_c \vec{u}_1) = \sum_i \frac{\sum_j \frac{dm_{b,i}^j}{dt}}{V_{cell}} = \sum_i S_{M,i} = S_1 \tag{3.9}$$

$$\frac{\partial(\rho_2 \alpha_2 \alpha_c)}{\partial t} + \nabla \cdot (\rho_2 \alpha_2 \alpha_c \vec{u}_2) = \sum_i \frac{\sum_j Y_{b,i}^j \left(\frac{dm_b^j}{dt}\right)_{LPT \to VOF}}{V_{cell}} = \sum_i S_{2,i} = S_2 \tag{3.10}$$

where ρ is the density, $\vec{u}$ is the velocity, $S_{M,i}$ is the mass transfer source term from the Lagrangian phase to the VOF liquid phase for species *i*, and $S_{2,i}$ is the mass transfer source term from Lagrangian phase to the VOF gas phase for species *i*. Since Eq. 3.9 refers to the

entire liquid phase, the mass sources for each species are summed and designated S_1. S_2 is the mass source term due to the bubble removal above the free surface and is added to the VOF gas phase with the consideration of mass conservation in the system. These two source terms will be discussed in section 3.8.

After expanding and rearranging Eqs. 3.9 and 3.10 and then moving the densities to the right-hand side, they can be written as follows:

$$\frac{\partial \alpha_c \alpha_1}{\partial t} + \nabla \cdot (\alpha_c \alpha_1 \vec{u}_1) = \frac{S_1}{\rho_1} - \frac{\alpha_c \alpha_1}{\rho_1}\left[\frac{\partial \rho_1}{\partial t} + \vec{u}_1 \cdot \nabla \rho_1\right] \tag{3.11}$$

$$\frac{\partial \alpha_c \alpha_2}{\partial t} + \nabla \cdot (\alpha_c \alpha_2 \vec{u}_2) = \frac{S_2}{\rho_2} - \frac{\alpha_c \alpha_2}{\rho_2}\left[\frac{\partial \rho_2}{\partial t} + \vec{u}_2 \cdot \nabla \rho_2\right] \tag{3.12}$$

Adding Eq. 3.11 and Eq. 3.12, and combining with Eq. 3.2, the total continuity can be recovered:

$$\begin{aligned} &\frac{\partial \alpha_c}{\partial t} + \nabla \cdot \alpha_c(\alpha_1 \vec{u}_1 + \alpha_2 \vec{u}_2) = \frac{S_1}{\rho_1} + \frac{S_2}{\rho_2} \\ &- \frac{\alpha_c \alpha_1}{\rho_1}\left[\frac{\partial \rho_1}{\partial t} + \vec{u}_1 \cdot \nabla \rho_1\right] - \frac{\alpha_c \alpha_2}{\rho_2}\left[\frac{\partial \rho_2}{\partial t} + \vec{u}_2 \cdot \nabla \rho_2\right] \end{aligned} \tag{3.13}$$

The volume-averaged mixture velocity is defined as follows:

$$\vec{u} = \alpha_1 \vec{u}_1 + \alpha_2 \vec{u}_2 \tag{3.14}$$

Therefore, after combining with Eq. 3.14 and rearranging, Eq. 3.13 can be written as follows:

$$\begin{aligned} \nabla \cdot (\alpha_c \vec{u}) = &-\frac{\partial \alpha_c}{\partial t} + \frac{S_1}{\rho_1} + \frac{S_2}{\rho_2} - \frac{\alpha_c \alpha_1}{\rho_1}\left[\frac{\partial \rho_1}{\partial t} + \vec{u}_1 \cdot \nabla \rho_1\right] \\ &- \frac{\alpha_c \alpha_2}{\rho_2}\left[\frac{\partial \rho_2}{\partial t} + \vec{u}_2 \cdot \nabla \rho_2\right] \end{aligned} \tag{3.15}$$

Note that Eq. 3.15 is important and will be used later in the derivation of the phase fraction equation and the pressure equation. Since OpenFOAM cannot solve for $\vec{u}_1$ and $\vec{u}_2$ separately, the mixture velocity that can be solved in OpenFOAM is introduced. After adding this extra term, Eq. 3.11 can be rewritten to give the following equation:

$$\begin{aligned} &\frac{\partial \alpha_c \alpha_1}{\partial t} + \nabla \cdot (\alpha_c \alpha_1 \vec{u}) + \nabla \cdot (\alpha_c \alpha_1 \vec{u}_1) - \nabla \cdot (\alpha_c \alpha_1 \vec{u}) \\ &= \frac{S_1}{\rho_1} - \frac{\alpha_c \alpha_1}{\rho_1}\left[\frac{\partial \rho_1}{\partial t} + \vec{u}_1 \cdot \nabla \rho_1\right] \end{aligned} \tag{3.16}$$

Eq. 3.16 can then be rearranged using Eqs. 3.2 and 3.14. After introducing the relative velocity, $\vec{u}_R$, which is just the difference between $\vec{u}_1$ and $\vec{u}_2$, Eq. 3.16 can be rewritten as follows:

$$\frac{\partial \alpha_c \alpha_1}{\partial t} + \nabla \cdot (\alpha_c \alpha_1 \vec{u}) + \nabla \cdot (\alpha_c \alpha_1 \alpha_2 \vec{u}_R) = \frac{S_1}{\rho_1} - \frac{\alpha_c \alpha_1}{\rho_1}\left[\frac{\partial \rho_1}{\partial t} + \vec{u}_1 \cdot \nabla \rho_1\right] \quad (3.17)$$

Then, if the $\alpha_1 \nabla \cdot (\alpha_c \vec{u})$ is added and subtracted to include the mixture velocity, Eq. 3.17 can be rewritten in the following form:

$$\frac{\partial \alpha_c \alpha_1}{\partial t} + \nabla \cdot (\alpha_c \alpha_1 \vec{u}) + \nabla \cdot (\alpha_c \alpha_1 \alpha_2 \vec{u}_R) = \frac{S_1}{\rho_1} - \frac{\alpha_c \alpha_1}{\rho_1}\left[\frac{\partial \rho_1}{\partial t} + \vec{u}_1 \cdot \nabla \rho_1\right] + \alpha_1 \nabla \cdot (\alpha_c \vec{u}) - \alpha_1 \nabla \cdot (\alpha_c \vec{u}) \quad (3.18)$$

After rearranging and grouping Eq. 3.18, it can be rearranged as follows:

$$\frac{\partial \alpha_c \alpha_1}{\partial t} + \nabla \cdot (\alpha_c \alpha_1 \vec{u}) + \nabla \cdot (\alpha_c \alpha_1 \alpha_2 \vec{u}_R) = \alpha_2 \left\{\frac{S_1}{\rho_1} - \frac{\alpha_c \alpha_1}{\rho_1}\left[\frac{\partial \rho_1}{\partial t} + \vec{u}_1 \cdot \nabla \rho_1\right]\right\} + \alpha_1 \left\{\frac{\alpha_c \alpha_2}{\rho_2}\left[\frac{\partial \rho_2}{\partial t} + \vec{u}_2 \cdot \nabla \rho_2\right] - \frac{S_2}{\rho_2}\right\} + \alpha_1 \frac{\partial \alpha_c}{\partial t} + \alpha_1 \nabla \cdot (\alpha_c \vec{u}) \quad (3.19)$$

In the OpenFOAM code, a term called `dgdt` is used to represent the following portion of the equation:

$$dgdt = \alpha_2 \left\{\frac{S_1}{\rho_1} - \frac{\alpha_c \alpha_1}{\rho_1}\left[\frac{\partial \rho_1}{\partial t} + \vec{u}_1 \cdot \nabla \rho_1\right]\right\} + \alpha_1 \left\{\frac{\alpha_c \alpha_2}{\rho_2}\left[\frac{\partial \rho_2}{\partial t} + \vec{u}_2 \cdot \nabla \rho_2\right] - \frac{S_2}{\rho_2}\right\} \quad (3.20)$$

After introducing this term, Eq. 3.20 can be written as follows:

$$\frac{\partial \alpha_c \alpha_1}{\partial t} + \nabla \cdot (\alpha_c \alpha_1 \vec{u}) + \nabla \cdot (\alpha_c \alpha_1 \alpha_2 \vec{u}_R) = dgdt + \alpha_1 \frac{\partial \alpha_c}{\partial t} + \alpha_1 \nabla \cdot (\alpha_c \vec{u}) \quad (3.21)$$

In OpenFOAM, the implicit and the explicit source terms are defined as:

$$S_P = -\frac{dgdt}{\alpha_2} \quad (3.22)$$

$$S_U = \frac{dgdt}{\alpha_2} \quad (3.23)$$

The `dgdt` term is therefore related to S_U and S_P as follows:

$$S_U + \alpha_1 S_P = \frac{dgdt}{\alpha_2} - \alpha_1 \frac{dgdt}{\alpha_2} = \frac{dgdt}{\alpha_2}(1 - \alpha_1) = dgdt \quad (3.24)$$

After replacing the `dgdt` term by Eq. 3.24 and moving $\alpha_1 \frac{\partial \alpha_c}{\partial t}$ and $\alpha_1 \nabla \cdot (\alpha_c \vec{u})$ to the left-hand side, Eq. 3.21 can be rearranged to give the following expression:

$$\frac{\partial \alpha_c \alpha_1}{\partial t} + \nabla \cdot (\alpha_c \alpha_1 \vec{u}) + \nabla \cdot (\alpha_c \alpha_1 \alpha_2 \vec{u}_R) - \alpha_1 \frac{\partial \alpha_c}{\partial t} - \alpha_1 \nabla \cdot (\alpha_c \vec{u}) = S_U + \alpha_1 S_P \quad (3.25)$$

Eq. 3.25 is the final form of the equation used in the VOF solver.

3.5. Momentum Conservation Equation

The momentum conservation equation is derived from the general volume-averaged Navier-Stokes equation that would normally be used for a VOF solver, which is shown as Eq. 3.26. As seen in Eq. 3.27, a new pressure term, p_{rgh}, is introduced to exclude the hydrostatic pressure. Eq. 3.28 can be obtained after taking the gradient of p_{rgh}. Eq. 3.29 is the modified Navier-Stokes equation that can be derived by substituting ∇p into Eq. 3.26. The modified Navier-Stokes equation includes the continuous phase fraction, α_c, and the interphase exchange from the Lagrangian phase to the continuous phase, which is denoted as F_d. F_{ST} represents the surface tension force.

$$\frac{\partial (\rho \vec{u})}{\partial t} + \nabla \cdot (\rho \vec{u} \vec{u}) = -\nabla p + \rho \vec{g} + F_{ST} - \nabla \cdot \tau \quad (3.26)$$

$$p_{rgh} = p - \rho \vec{g} \cdot \vec{h} \quad (3.27)$$

$$\nabla p_{rgh} = \nabla p - \vec{g} \cdot \vec{h} \nabla \rho - \rho \vec{g} \quad (3.28)$$

$$\frac{\partial (\alpha_c \rho \vec{u})}{\partial t} + \nabla \cdot (\alpha_c \rho \vec{u} \vec{u}) + \nabla \cdot \tau = F_d + F_{ST} - \vec{g} h \nabla \rho - \nabla P_{rgh} \quad (3.29)$$

F_d can be calculated using the following expression:

$$F_d = S_{U,l} + S_{U,g} \quad (3.30)$$

The starting point for the derivation of the momentum conservation equation is Eq. 3.29. After combining Eqs. 3.29 and 3.30, it can be rearranged as follows:

$$\frac{\partial (\alpha_c \rho \vec{u})}{\partial t} + \nabla \cdot (\alpha_c \rho \vec{u} \vec{u}) + \nabla \cdot \tau = S_{U,l} + S_{U,g} + F_{ST} - \vec{g} h \nabla \rho - \nabla P_{rgh} \quad (3.31)$$

In OpenFOAM, the non-conservative form of the momentum equation is solved. This equation is given by the following expression:

$$\frac{\partial (\alpha_c \rho \vec{u})}{\partial t} + \nabla \cdot (\alpha_c \rho \vec{u} \vec{u}) - \vec{u} \frac{\partial (\alpha_c \rho)}{\partial t} - \vec{u} \cdot \nabla (\alpha_c \rho \vec{u}) - \vec{u} S_1 - \vec{u} S_2 + \nabla \cdot \tau = S_{U,l} + S_{U,g} + F_{ST} - \vec{g} h \nabla \rho - \nabla P_{rgh} \quad (3.32)$$

The third to the sixth terms in Eq. 3.32 is referred as the continuity error.

3.6. Pressure Equation

Since the momentum equation contains two independent variables (velocity and pressure), a single equation is insufficient to solve the system. The momentum equation must be combined with the continuity equation to derive an explicit equation for pressure. One algorithm to calculate pressure and velocity is known as the pressure-implicit with splitting of operators (PISO) algorithm.

The PISO algorithm starts with the momentum conservation equation, which is Eq. 3.32. Following discretization, the predicted velocity can be determined from the decomposed equation matrix:

$$\vec{u}^{**} = A^{-1}H + A^{-1}F_P + A^{-1}F_{ST} - A^{-1}\nabla P_{rgh} - A^{-1}(\vec{g}h\nabla\rho) \tag{3.33}$$

where A and H are the diagonal and off-diagonal components of the coefficient matrix in the discretized momentum equation. Since the continuous phase does not occupy all of a cell volume, this equation must be multiplied by α_c to become consistent with Eq. 3.32. The divergence can then be taken to give the following expression:

$$\nabla\cdot\ (\alpha_c\vec{u}) = \nabla\cdot\left[\alpha_c(\mathrm{A}^{-1}H + \mathrm{A}^{-1}F_P + \mathrm{A}^{-1}F_{ST} - \mathrm{A}^{-1}\nabla P_{rgh} - \mathrm{A}^{-1}(\vec{g}h\nabla\rho))\right] \tag{3.34}$$

The solution to continuity was derived in Eq. 3.25. Using a rearranged form of Eq. 3.25, Eq. 3.34 can be rewritten as follows:

$$\begin{aligned}\nabla^2\left(\alpha_c\mathrm{A}^{-1}P_{rgh}\right) &= \nabla\cdot\left[\alpha_c\left(\mathrm{A}^{-1}H + \mathrm{A}^{-1}F_P + \mathrm{A}^{-1}F_{ST} - \mathrm{A}^{-1}(\vec{g}h\nabla\rho)\right)\right] \\ &+\frac{\partial\alpha_c}{\partial t} - \frac{S_1}{\rho_1} - \frac{S_2}{\rho_2} + \frac{1}{\rho_1}\left(\frac{\partial(\alpha_c\alpha_1\rho_1)}{\partial t} + \nabla\cdot\left(\alpha_c\alpha_{1f}\phi\rho_{1f}\right)\right) - \frac{\partial(\alpha_c\alpha_1)}{\partial t} \\ &-\nabla\cdot(\alpha_c\alpha_{1f}\phi) + \frac{1}{\rho_2}\left(\frac{\partial(\alpha_c\alpha_2\rho_2)}{\partial t} + \nabla\cdot(\alpha_c\alpha_{2f}\phi\rho_{2f})\right) \\ &-\frac{\partial(\alpha_c\alpha_2)}{\partial t} - \nabla\cdot(\alpha_c\alpha_{2f}\phi)\end{aligned} \tag{3.35}$$

The pressure equation can be split into incompressible and compressible terms. To simplify implementation in OpenFOAM, the incompressible and compressible terms are defined separately.

The incompressible term is defined as follows:

$$\nabla \cdot \{\alpha_{cf}[\mathrm{A}^{-1}H + \mathrm{A}^{-1}F_P + \mathrm{A}^{-1}F_{ST} - \mathrm{A}^{-1}(\vec{g}h\nabla\rho)]\} - \nabla^2\left(\alpha_{cf}\mathrm{A}^{-1}P_{rgh}\right) + \frac{\partial\alpha_c}{\partial t} \tag{3.36}$$

The compressible term for phase 1 is defined by the following expression:

$$\frac{1}{\rho_1}\left(\frac{\partial(\alpha_c\alpha_1\rho_1)}{\partial t} + \nabla\cdot(\alpha_c\alpha_{1f}\phi\rho_{1f})\right) - \frac{\partial(\alpha_c\alpha_1)}{\partial t} - \nabla\cdot(\alpha_c\alpha_{1f}\phi) - \frac{S_1}{\rho_1} \tag{3.37}$$

The compressible term for phase 2 is defined by the following expression:

$$\frac{1}{\rho_2}\left(\frac{\partial(\alpha_c\alpha_2\rho_2)}{\partial t} + \nabla\cdot(\alpha_c\alpha_{2f}\phi\rho_{2f})\right) - \frac{\partial(\alpha_c\alpha_2)}{\partial t} - \nabla\cdot(\alpha_c\alpha_{2f}\phi) - \frac{S_2}{\rho_2} \tag{3.38}$$

3.7. Species Conservation Equations

The mass fractions of species in the continuous phase can be calculated using the species conservation equations:

$$\frac{\partial(\alpha_c\alpha_1\rho_1Y_{1,i})}{\partial t} + \nabla\cdot(\alpha_c\alpha_1\rho_1\vec{u}Y_{1,i})$$

$$-\nabla\cdot\left(\alpha_c\alpha_1\left(\mu_t\frac{\rho_1}{Sc_1} + \mu\frac{\rho_1}{Sc}\right)\nabla Y_{1,i}\right) = \frac{\sum_j\frac{dm_{b,i}^j}{dt}}{V_{cell}} = S_{M,i} \tag{3.39}$$

$$\frac{\partial(\alpha_c\alpha_2\rho_2Y_{2,i})}{\partial t} + \nabla\cdot(\alpha_c\alpha_2\rho_2\vec{u}Y_{2,i})$$

$$-\nabla\cdot\left(\alpha_c\alpha_2\left(\mu_t\frac{\rho_2}{Sc_2} + \mu\frac{\rho_2}{Sc}\right)\nabla Y_{2,i}\right) = \frac{\sum_j Y_{b,i}^j\left(\frac{dm_b^j}{dt}\right)_{LPT\to VOF}}{V_{cell}} = S_{2,i} \tag{3.40}$$

where Y_i represents the mass fraction of species i, $S_{M,i}$ is the mass transfer source term for species i in the VOF liquid phase, and $S_{2,i}$ is the mass source term that should be added to the VOF gas phase due to transfer from the LPT phase.

3.8. Interphase Exchange Sources

Coupling between the continuous phase and the dispersed phase is achieved by correcting the continuous phase fraction through interphase exchange sources that are included in the phase continuity, pressure, species, and momentum equations.

As mentioned in section 3.4, $S_{M,i}$ is the mass transfer source term from the Lagrangian phase to the VOF liquid phase for species i. The mass sources for each species are summed in the VOF liquid phase and denoted as S_1 in Eq. 3.9. S_1 is the total mass source transferred from the Lagrangian phase to the VOF liquid phase and it is added in the pressure equation and the phase fraction equation.

As seen in Eq. 3.10, S_2 is a mass source term that sums up the mass of particles that is removed from the LPT phase when they reach the free surface and this term is added to the VOF gas phase to ensure that the mass is conserved in the whole system. It is included in the pressure, phase fraction, and species equations. Particles are removed when they reach the free surface because this is where the gas in the bubbles is transferred to the continuous gas phase.

As shown in Eq. 3.30, the momentum interphase exchange term, F_d, contains two terms: $S_{U,l}$ and $S_{U,g}$. The first term calculates the momentum sources transferred from the Lagrangian phase to the VOF liquid phase; therefore, it is added to the momentum equation to include the momentum transfer from the Lagrangian phase to the VOF liquid phase. The second term sums up the momentum of the particles that is removed at the free surface. This is added to the momentum equation to ensure that the momentum is conserved in the whole system. All the source terms mentioned above, as well as the particle removal, were implemented in the Lagrangian library.

In the current study, gravity, buoyancy, drag, lift, virtual mass, and turbulent dispersion forces were considered as the forces acting on the bubbles. Collision model was not included due to the lack of the experimental data and/or empirical correlations in order to choose the model parameters to include the interactions of the bubbles inside each parcel.

Ming et al. (2017) included bubble-surface interactions within the Lagrangian framework to model bubble bursting at the free surface. However, the surface resistance was not included in the current study. Such a model could be implemented in the future to include the effects of the surface resistance for bubble disengagement at the free surface in bubble plumes.

3.9. Verification Cases

Two cases were simulated to verify the performance of the mass transfer model. The mass transfer performance can be quantified by the prediction of the mass fraction of dissolved gases, the estimation of the mass transfer coefficient, and the bubble shrinkage rate. The first case was used to investigate the mass transfer of a single stationary bubble sitting in the middle of a three-dimensional box, while the second case was a single rising bubble that was initially injected through the bottom of a box. The second case was simulated to validate both the gas dissolution and compressibility effects with depth. A constant mass transfer coefficient was used in both verification cases to facilitate comparisons between the theoretical and numerical results.

3.9.1. Bubble in Box

The geometry of the bubble in box case is shown below. A single stationary bubble that contains only oxygen sits in the middle of the box with water slowly flow upward in the vertical direction. Figure 3.3 shows a graphical representation of the case, while Table 3.1 through Table 3.3 list the parameters characterizing the study.

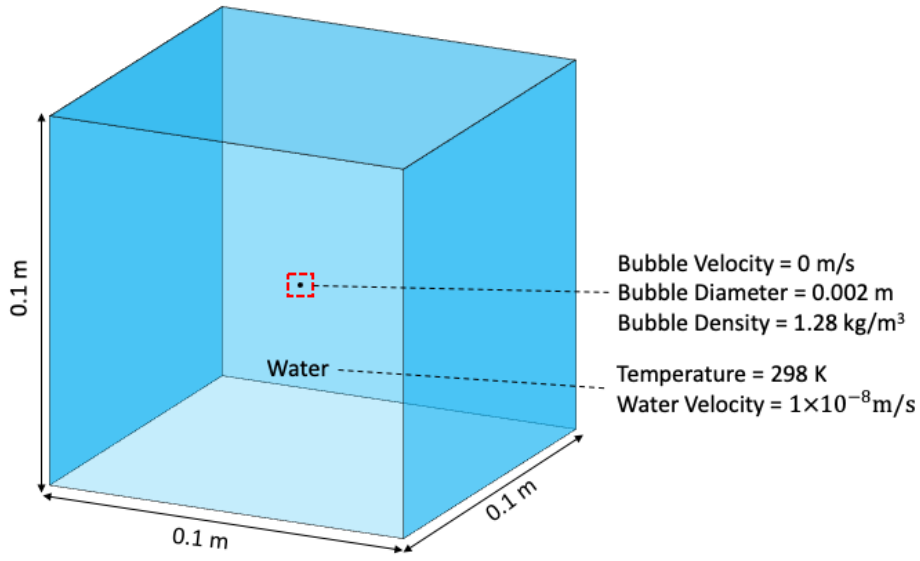

Figure 3.3: Geometry and conditions used in the bubble in box case.

Table 3.1: Initial Conditions for the Bubble in Box Cases

Variable	Initial Condition
Liquid volume fraction, α_1 (-)	$\alpha_1 = 1$ (below the free surface) $\alpha_1 = 0$ (above the free surface) *
Temperature, T (K)	298
Velocity, $\vec{u}$ (m/s)	1.0×10^{-8}
Modified pressure, P_{rgh} (Pa)	101 325
Turbulent kinematic viscosity, ν_t (m^2/s)	1.0×10^{-11}
O_2 (liquid) mass fraction, Y_{1,O_2} (-)	0
N_2 (liquid) mass fraction, Y_{1,N_2} (-)	0

* This condition is used in the second verification case

Table 3.2: Liquid Phase Properties (Welty et. al., 2008)

Property	Value
Density, ρ (kg/m^3)	996.7
Specific heat capacity, c_p (J kg^{-1} K^{-1})	4 180
Dynamic viscosity, μ (Pa s)	9.0×10^{-4}
Prandtl number, Pr (-)	6.30

Table 3.3: Oxygen Properties (Welty et al., 2008; Sander, 2015)

Property	Value
Density, ρ (kg/m^3)	Ideal Gas Law
Specific heat capacity, c_p (J kg^{-1} K^{-1})	920.0
Henry's Law constant, H (-)	0.02973
Diffusivity coefficient, D_{ab} (m/s)	2.4×10^{-9}

Two sub-cases were set up and simulated to evaluate the mass transfer. The first case simulated the bubble inside the box without mass transfer on. Since the bubble was set to be stationary, the diameter should not change with a set pressure. The second simulation turned the mass transfer model on. In this case, the bubble shrinkage should only be the result of mass transfer since the bubble is stationary. The mass transfer model used was a constant model with a Sherwood number of 2000.

The following equations were used to calculate the theoretical results for the mass transfer model.

1. Check the mass fraction of oxygen in water, Y_1.

Eq. 3.9 can be simplified to the following equation in this case:

$$\frac{\partial(\alpha_c \alpha_1 \rho_1 Y_1)}{\partial t} = S_{M,i} \tag{3.41}$$

where $\alpha_c \alpha_1 = 1$ and ρ_1 is constant. Therefore, Eq. 3.41 can be written as follows:

$$\rho_1 \frac{dY_1}{dt} = S_{M,i} \tag{3.42}$$

Moving ρ_1 to the RHS, Eq. 3.42 can be rearranged as follows:

$$\frac{dY_1}{dt} = \frac{S_{M,i}}{\rho_1} \tag{3.43}$$

Performing the integration results in the following expression:

$$\Delta Y_1 = \int \frac{S_{M,i}}{\rho_1} dt = \sum \frac{S_{M,i}}{\rho_1} \Delta t \tag{3.44}$$

2. Check the shrinkage of the bubble, Δd_b.

The expansion of Eq. 3.4 is shown below:

$$\frac{dm_{b,i}^j}{dt} = \sum \pi d_b^2 k_l^j \rho_1 (H_i Y_{b,i}^j \frac{\rho_b}{\rho_1} - Y_{1,i}^j) \tag{3.45}$$

In the Lagrangian library, the left-hand side equals to the mass source term times the volume of the cell:

$$S_{M,i} V_{cell} = \sum_j \frac{dm_{b,i}^j}{dt} \tag{3.46}$$

The left-hand side of Eq. 3.46 can be written to involve the d_b as follows:

$$\frac{dm_{b,i}^j}{dt} = \frac{d(\rho_b V_b)}{dt} = \rho_b \frac{dV_b}{dt} = \frac{\pi}{6} \rho_b \frac{d(d_b^3)}{dt} = \frac{\pi}{2} \rho_b d_b^2 \frac{d(d_b)}{dt} \tag{3.47}$$

This equation can be rearranged as follows:

$$\frac{\pi}{2} \rho_b d_b^2 \frac{d(d_b)}{dt} = S_{M,i} V_{cell} \tag{3.48}$$

Integrating this expression and making some rearrangements results in the final expression that was used to track the diameter change:

$$\int d_b^2 d(d_b) = \frac{2}{\pi} \int \frac{S_{M,i} V_{cell}}{\rho_b} dt \tag{3.49}$$

$$\frac{1}{3}d_{b,0}^3 - \frac{1}{3}d_{b,f}^3 = \frac{2}{\pi}\sum\frac{S_{M,i}V_{cell}}{\rho_b}\Delta t \tag{3.50}$$

$$d_{b,0}^3 - d_{b,f}^3 = \frac{6}{\pi}\sum\frac{S_{M,i}V_{cell}}{\rho_b}\Delta t \tag{3.51}$$

$$d_{b,f}^3 = d_{b,0}^3 - \frac{6}{\pi}\sum\frac{S_{M,i}V_{cell}}{\rho_b}\Delta t \tag{3.52}$$

$$d_{b,f}^3 = \sqrt[3]{d_{b,0}^3 - \frac{6}{\pi}\sum\frac{S_{M,i}V_{cell}}{\rho_b}\Delta t} \tag{3.53}$$

3. Check the mass transfer coefficient, k_l^j.

   The mass transfer coefficient can be calculated using the following equation:

$$k_l^j = \frac{Sh\ D_{ab}}{d_b} \tag{3.54}$$

   where Sh and D_{ab} are Sherwood number and diffusivity coefficient, respectively.

In the first case, as shown in Figure 3.4, the bubble diameter did not change when the mass transfer model was turned off as expected.

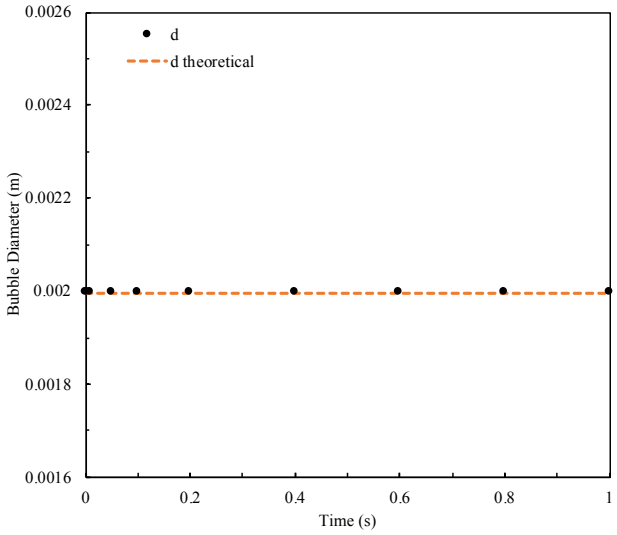

Figure 3.4: Comparisons between the predicted bubble diameter (black dots) and theoretical bubble diameter (orange dashed line) for the bubble in box without mass transfer case.

The other case was intended to verify the mass transfer performance when the mass transfer model was turned on. To clarify, in Figure 3.5, Y_{O2} represents the theoretical right-hand side of Eq. 3.44 and is the mass fraction of oxygen in the water. `O2.water` is the mass

fraction of oxygen dissolved in the water as obtained from the solver output. As seen in Figure 3.5, the theoretical mass fraction of dissolved oxygen matches the mass fraction of oxygen in water calculated by OpenFOAM.

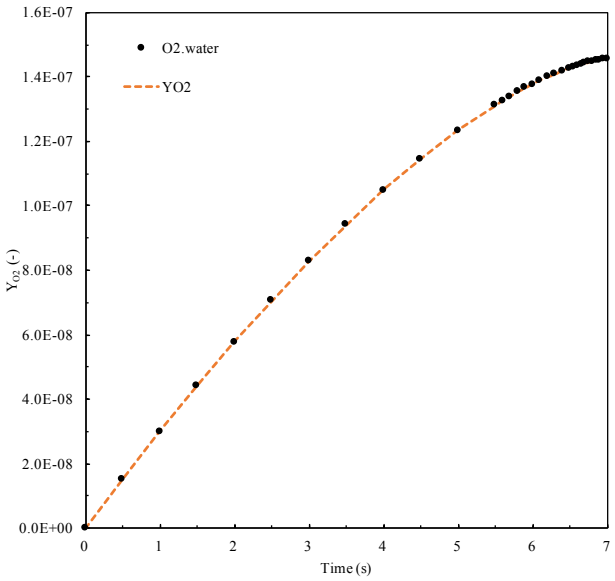

Figure 3.5: Comparisons between the predicted mass fraction of oxygen in water (black dots) and theoretical mass fraction of oxygen in water (orange dashed line) for the bubble in box with mass transfer case.

The second component was testing the bubble shrinkage rate. As shown in Figure 3.6, the values and trend of bubble diameters from the solver output and the theoretical results that were calculated using Eq. 3.53 match each other. This indicates that the additions to the Lagrangian library are behaving as expected based on their mathematical derivation.

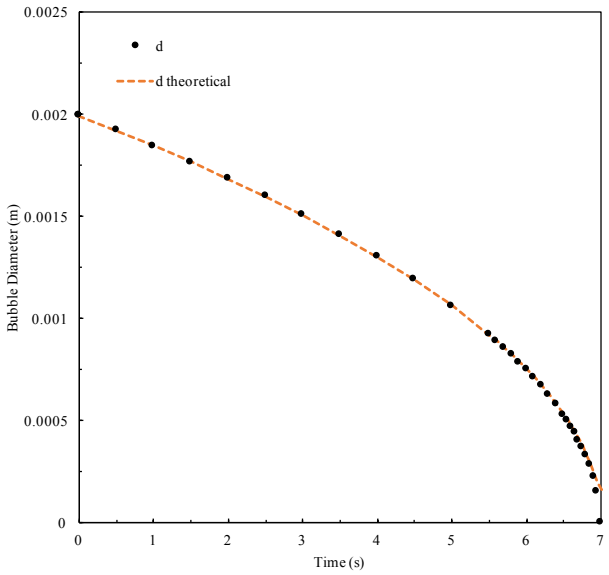

Figure 3.6: Comparisons between the predicted bubble diameter (black dots) and theoretical bubble diameter (orange dashed line) for the bubble in box with mass transfer case.

Similarly, as shown in Figure 3.7, the values and trend of mass transfer coefficient obtained from OpenFOAM match the theoretical results calculated by Eq. 3.54. Based on the mass transfer performance described above, the numerical performance of the gas dissolution model is confirmed. The theoretical value close to the point where the bubble is completely dissolved is not accurate due to limitations in the accuracy of the numerical integration. Based on the results in Figure 3.5 through Figure 3.7, the solver functioned properly even when the entire bubble dissolves. When tested with a completely saturated liquid phase, the bubble size did not change and the solver still worked.

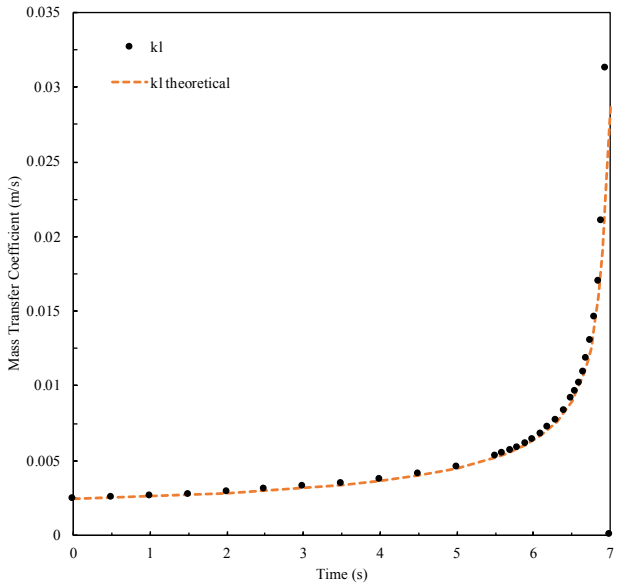

Figure 3.7: Comparisons between the predicted mass transfer coefficient (black dots) and theoretical mass transfer coefficient (orange dashed line) for the bubble in box with mass transfer case.

3.9.2. Single Rising Bubble

The geometry of the single rising bubble case is shown in Figure 3.8. A single rising oxygen bubble was injected in the middle of the box and the water stays stationary. The properties were the same as mentioned in Table 3.1 through Table 3.3. The mass transfer model used was the same as the previous verification case (i.e., constant Sherwood number of 2000). A constant drag coefficient of 0.54 was used in this verification case.

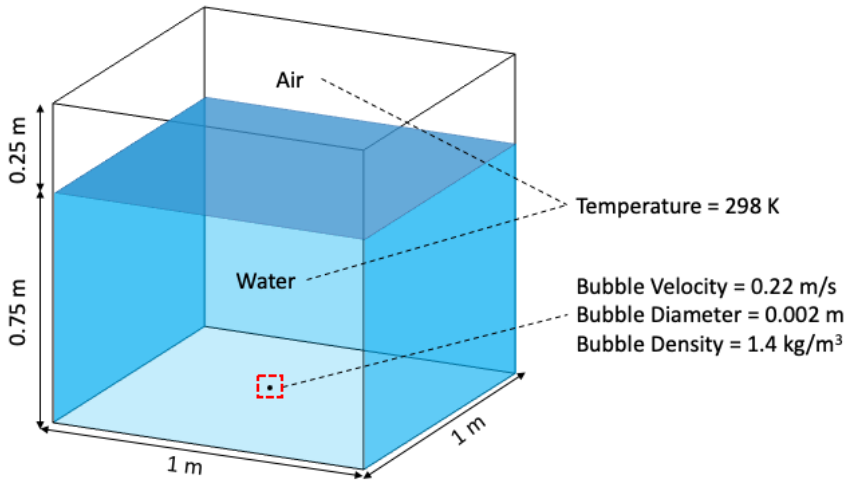

Figure 3.8: Geometry and conditions used in the single rising bubble case.

Two sub-cases were used for this verification case. The first case excludes the mass transfer model, and the second case includes the mass transfer model. The purpose of the former case was to evaluate the implementation of gas expansion at different depths. The case that includes the mass transfer model was set up to verify both the mass transfer model and the gas expansion working in tandem. In this verification case, the pressure was set to vary with depth by the following equation:

$$P\,[Pa] = 101325 + 996.7 \times 9.81 \times \text{Depth} \tag{3.55}$$

In the initial test, the mass transfer was off; therefore, the bubble diameter was expected to increase due to the pressure and bubble density as it rose. The bubble density and diameter were updated in the Lagrangian library using Eqs. 3.6 and 3.7 and were recorded at each time step.

The following equations were used to calculate the theoretical results for bubble position and diameter changes in this case. The bubble position, h_b, can be determined using Eq. 3.56:

$$\frac{dh_b}{dt} = \sqrt{\frac{4}{3}\frac{(\rho_l - \rho_b)}{\rho_l}\frac{d_b\vec{g}}{C_D}} \tag{3.56}$$

The corresponding pressure for the bubble at certain position can be calculated using the following equation:

$$P\,[Pa] = 101325 + 996.7 \times 9.81 \times (\text{Water Level} - h_b) \tag{3.57}$$

The bubble density was calculated using the ideal gas law (Eq. 3.6) with the pressure of the bubble at a specific position updated by Eq. 3.57.

The mass of the bubble can be updated using the following equation:

$$\frac{dm_{b,i}^j}{dt} = \sum \pi d_b^2 k_l^j H_i \rho_b \tag{3.58}$$

The bubble diameter can then calculated using Eq. 3.7 with the mass was calculated from Eq. 3.58 and the pressure-dependent density.

The mass of the bubble did not change for the first case because there was no mass transfer in this case. As seen in the Figure 3.9, the bubble diameter and position determined using

OpenFOAM match the theoretical results. This verifies that the model predicts the correct density based on the pressure, which in turn calculates the correct bubble diameter from the volume.

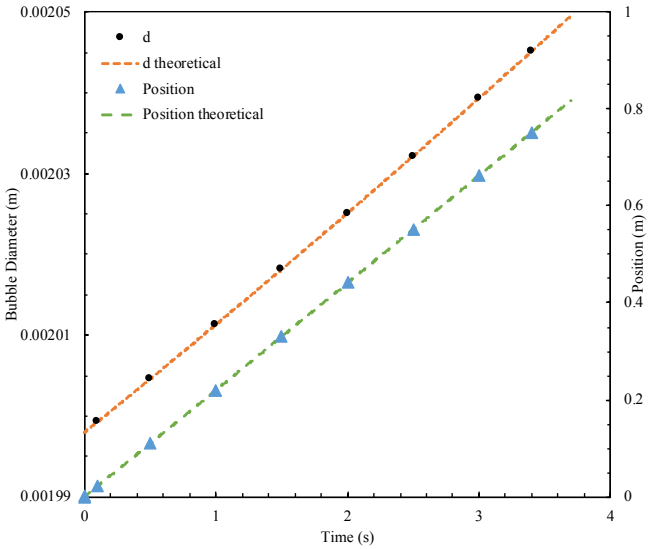

Figure 3.9: Comparisons between the predicted (black dots) and theoretical (orange dashed line) bubble diameter and predicted (blue triangles) and theoretical (green dashed line) bubble position versus time for the single rising bubble without mass transfer case.

For the second case, both gas expansion and mass transfer performance were evaluated. As mentioned in the bubble in box case, Y_{O2} and `O2.water` represent the theoretical and computational mass fraction of oxygen dissolved in the water, respectively. Figure 3.10 shows that the theoretical mass fraction of oxygen in water matches the computational results.

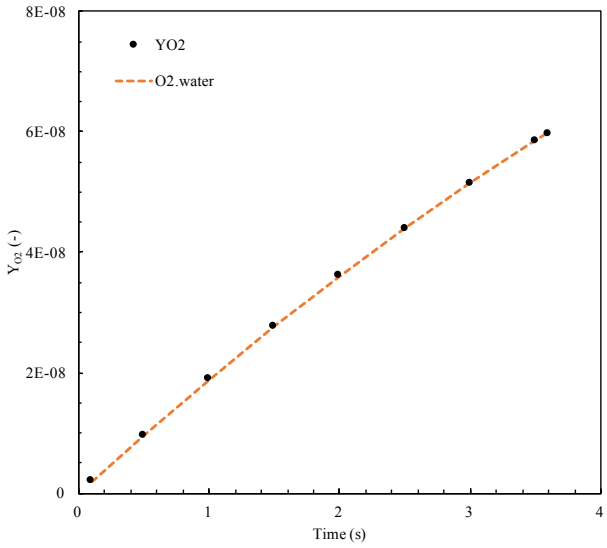

Figure 3.10: Comparisons between the predicted mass fraction of oxygen in water (black dots) and theoretical mass fraction of oxygen in water (orange dashed line) for the single rising bubble with mass transfer case.

The bubble diameter and position can be updated using the method described earlier (Eq. 3.56 – Eq. 3.58). The results in Figure 3.11 show that the computational results provide an exact fit to the theoretical calculations.

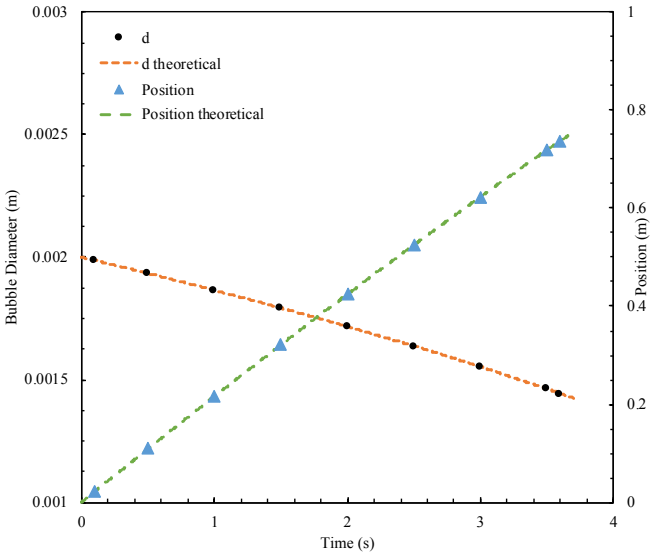

Figure 3.11: Comparisons between the predicted (black dots) and theoretical (orange dashed line) bubble diameter and predicted (blue triangles) and theoretical (green dashed line) bubble position versus time for the single rising bubble with mass transfer case.

As shown in Figure 3.12, the computational mass transfer coefficient matches the theoretical result that was calculated using Eq. 3.54. This case confirms that both the gas compressibility model and the gas dissolution model could predict local effects on bubble size based on pressure gradient and mass transfer.

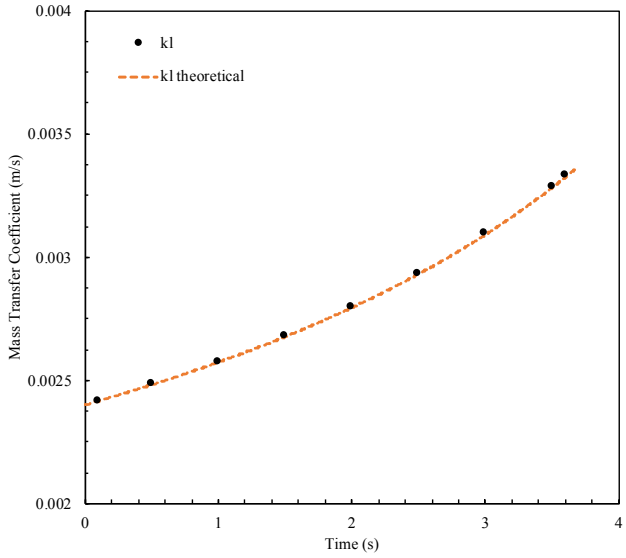

Figure 3.12: Comparisons between the predicted mass transfer coefficient (black dots) and theoretical mass transfer coefficient (orange dashed line) for the single rising bubble with mass transfer case.

3.10. Conclusions

A new solver called `lagrangianMTCompressibleInterFoam` was developed to combine a compressible VOF solver and the Lagrangian library in OpenFOAM to simulate bubble plumes. The VOF solver is used to model the free surface, while the LPT method tracks the dispersed phase in the liquid portion. Specifically, the solver used `compressibleInterFoam` with modifications to the phase fraction conservation equation, momentum conservation equation, pressure equation, and species conservation equations to account for the presence of Lagrangian particles occupying the same volume. Interphase mass, species and momentum exchange sources, the compressibility of gas, and a mass transfer model were implemented by modifying the Lagrangian library. The model implementation was verified by comparing simulation results for two sets of simple verification cases against theoretical calculations. The first of these two cases involved a

stationary oxygen bubble in a box full of quiescent, deoxygenated water. The model predicted no change in bubble size without mass transfer and matched theoretically predicted dissolution over time when mass transfer was turned on. The bubble shrinkage rate was also predicted according to theory. The second set of cases involved an oxygen bubble moving through quiescent, deoxygenated water. The effects of pressure on bubble size as well as the combined effects of bubble expansion and mass transfer were predicted well compared the theoretical results.

Chapter 4: Modelling Fluid Dynamics in Bubble Plumes

4.1. Introduction

The purpose of this chapter was to investigate and validate the hydrodynamics predictions of the newly developed solver for small-scale bubble plumes. The selected validation case used the experimental setup of Simiano (2005), and initial parameterization of the closure models was based on the simulation studies of Dhotre and Smith (2007) and Dhotre et al. (2009). Dhotre and Smith (2007) used the Eulerian-Eulerian (EE) approach with Reynolds-Averaged Navier-Stokes (RANS) turbulence modelling to simulate the experimental work of Simiano (2005). Dhotre et al. (2009) then further extended their study by repeating the simulations using an EE model with large eddy simulation (LES) for turbulence modelling. Although this is a small-scale case, the purpose of this validation study was to compare model predictions made using the new LPT-VOF solver to the available experimental data and results from EE simulations. Closure models were then tuned to better match the experimental data.

4.2. Case Studies

Dhotre and Smith (2007) and Dhotre et al. (2009) modelled an experiment conducted by Simiano (2005), in which air was injected into a cylindrical tank through a needle injector placed on the bottom of the tank along the centerline. The cylindrical tank had a diameter of 2 m and a height of 2 m with a water level of 1.5 m. The needle injector had a diameter of 0.15 m, and it consisted of 350 needles with inner diameters of 1 mm. In the studies of Dhotre and Smith (2007) and Dhotre et al. (2009), the gas injection rates were varied. However, they only used the gas injection rate of 7.5 NL/min for the three-dimensional simulations. Therefore, this flow rate was chosen to be the main gas injection rate investigated in the current study. The pressure and temperature were 1 atm and 293 K. The bubble size was approximately 2.5 mm, according to the average bubble size measured by Simiano (2005), and this was also the value used in Dhotre and Smith (2007) and Dhotre et al. (2009).

4.2.1. Geometry and Mesh

A sketch of the geometry used for the simulations is provided in Figure 4.1. It is difficult to reproduce the exact geometry of the needle injector in the CFD simulation. Therefore, approximations were made to try to represent the injector as accurately as possible based on the available information while also minimizing computational requirements. Bubble injection was specified to be on a 0.15 m diameter patch located at the centerline near the bottom of the tank. The inlet patch was located 0.05 m from the bottom of the tank to approximate the length of the needles (the actual length of the needles was not available from the literature). The bottom of this patch was specified to act as a wall and the top surface provided the area for bubble injection. To avoid liquid circulation under the inlet patch, the zone under the inlet patch was blocked using a porous zone. In the experiment, there would likely have been some liquid circulation between the needles, but this was difficult to implement in OpenFOAM because the configuration of the needles was not reported. If the zone under the inlet patch were left empty, it might have negative effects on the results due to liquid recirculation. Thus, setting up a blockage zone was considered to be a reasonable course of action for this case.

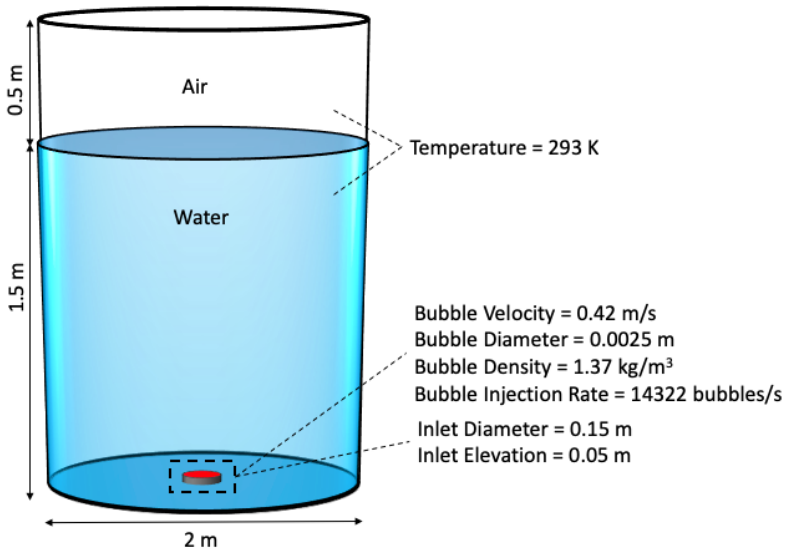

Figure 4.1: Geometry and conditions used in the Dhotre/Simiano case.

Two computational meshes were considered in this validation case to investigate the impact of mesh resolution. The chosen computational meshes are shown in Figure 4.2 and Figure 4.3.

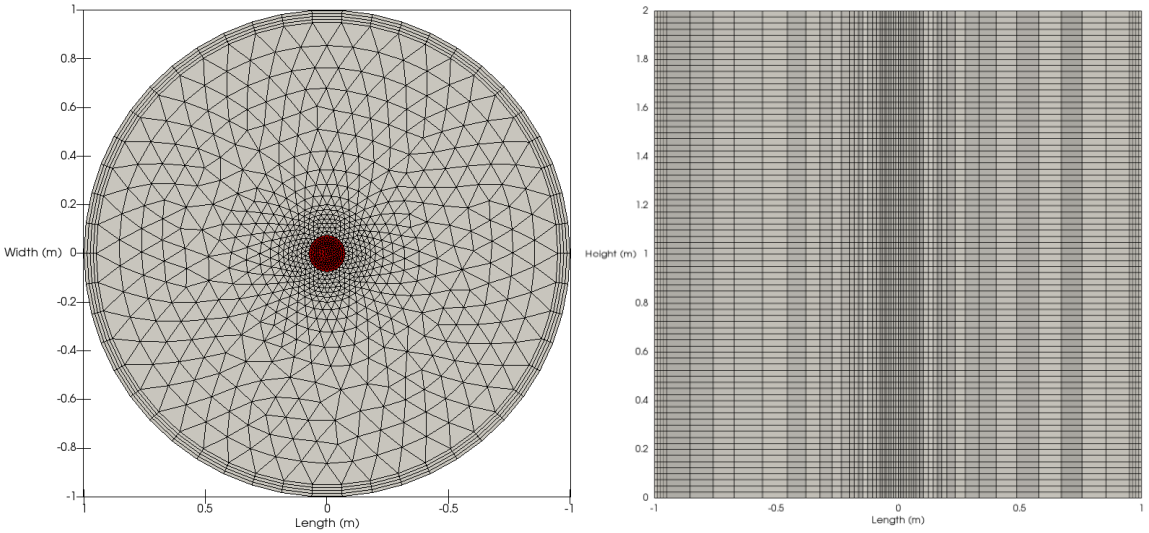

Figure 4.2: Coarse mesh used in the Dhotre/Simiano case showing the bottom view (left) and the side view (right). The mesh contains 154 560 computational cells and the injection patch is shown in red.

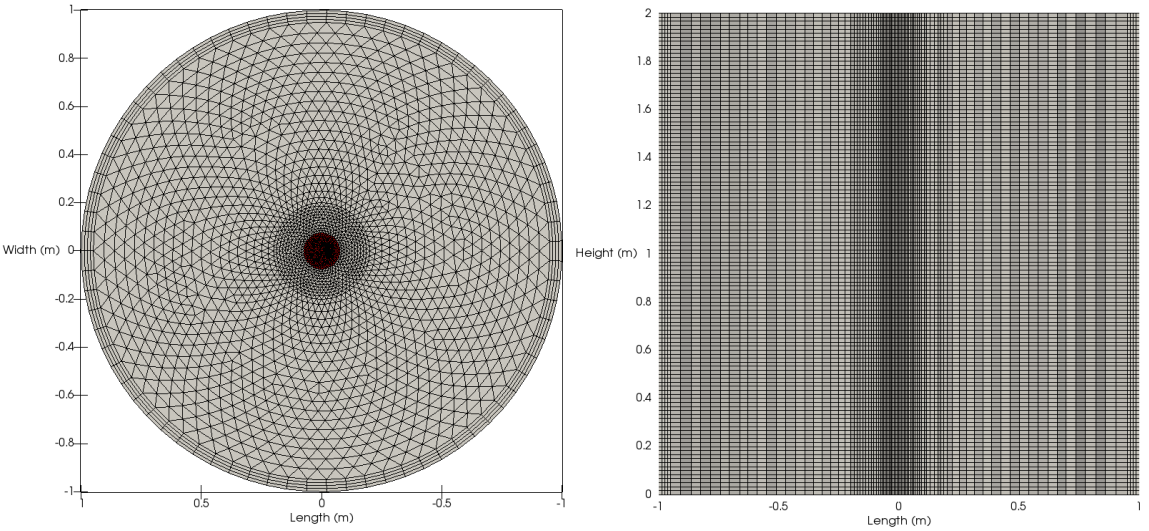

Figure 4.3: Fine mesh used in the Dhotre/Simiano case showing the bottom view (left) and the side view (right). The mesh contains 594 120 computational cells and the injection patch is shown in red.

4.2.2. Case Setup

All boundaries except for the inlet patch and the top are walls. A free-slip boundary condition was specified for the continuous phase on the inlet patch and bubbles were injected. The top was treated as an open boundary with a specified pressure. Table 4.1 lists the boundary conditions that were applied for the case.

Table 4.1: Boundary Conditions Used in the Dhotre/Simiano Case

Variable	Inlet Patch	Walls and Bottom	Top
Liquid volume fraction, α_1 (-)	Zero gradient	Zero gradient	Zero gradient
Temperature, T (K)	Zero gradient	Zero gradient	Zero gradient (outflow) T = 293 K (inflow)
Velocity, $\vec{u}$ (m/s)	Slip	No slip	Zero gradient (outflow) $\vec{u} = 0$ m/s (inflow)
Modified pressure, P_{rgh} (Pa)	Zero gradient	Zero gradient	101 325
Turbulent kinetic energy, k (m^2/s)*	Fixed value	Wall function	Zero gradient
Turbulent energy dissipation, ε (m^2/s^3)*	Fixed value	Wall function	Zero gradient
Lagrangian bubbles	Injection	Rebound	Escape**

*Turbulent kinetic energy and turbulent energy dissipation were used only for the RANS cases. **Although this was specified, bubbles are removed at the free surface.

The initial conditions used for the simulations are summarized in Table 4.2. Since a 1.5 m water depth is significant, the pressure field (not listed in the table) was initialized based on the depth.

Table 4.2: Initial Conditions Used in the Dhotre/Simiano Case

Variable	Initial Condition
Liquid volume fraction, α_1 (-)	$\alpha_1 = 1$ (below the free surface) $\alpha_1 = 0$ (above the free surface)
Temperature, T (K)	293
Velocity, $\vec{u}$ (m/s)	0
Modified pressure, P_{rgh} (Pa)	101 325
Turbulent kinematic viscosity, ν_t (m^2/s)	1.0×10^{-11}
Turbulent kinetic energy, k (m^2/s)*	6.8×10^{-4}
Turbulent energy dissipation, ε (m^2/s^3)*	4.2×10^{-2}

*Turbulent kinetic energy and turbulent energy dissipation were used only for the RANS cases.

Table 4.3 summarizes the thermophysical properties that were used for the liquid phase. Since the experiment was conducted at constant temperature and pressure effects on the liquid phase properties are negligible, constant properties were assumed.

Table 4.3: Liquid Water Properties Used in the Dhotre/Simiano Case (Welty et al., 2008)

Property	Value
Density, ρ (kg/m^3)	998.2
Specific heat capacity, c_p (J kg^{-1} K^{-1})	4 182
Dynamic viscosity, μ (Pa s)	9.93×10^{-4}
Prandtl number, Pr (-)	6.96

Simiano (2005) used a gas flow rate of 7.5 NL/min in the experiments, with reference conditions of 0 °C and atmospheric pressure. The actual injection flow rate at 293 K and the pressure at the bottom of the tank were calculated to be 1.17×10^{-4} m^3/s based on the gas density ratio. The gas density at the inlet was calculated to be 1.37 kg/m^3 using the ideal gas law at the corresponding pressure and temperature. The total area across the 350 injection needles was 2.75×10^{-4} m^2 and the corresponding injection velocity and bubble injection rate were calculated to be 0.42 m/s and 14 322 bubbles/s. The initial bubble size was set to be 2.5 mm and the size of the bubbles was allowed to change with pressure based on the ideal gas law model implemented in Chapter 3. Table 4.4 summarizes the air bubble properties used for the Lagrangian phase.

The bubble velocity at the injection point was determined using the cross-sectional area of the needles. This ensures that the correct amount of momentum is added to the system. However, in reality, the velocity of the bubbles at the end of the needles would be lower due formation of a bubble at the end of the needles. Since the bubbles attain their terminal velocity very quickly following injection, this is not expected to impact the results.

Table 4.4: Air Bubble Properties Used in the Dhotre/Simiano Case

Property	Parameter
Gas density at the inlet, $\rho_{b,inlet}$ (kg/m^3)	1.37
Bubble diameter at the inlet, d_b (mm)	2.5
Bubble velocity at the inlet, $\vec{u}_b$ (m/s)	0.42
Bubble injection rate (bubbles/s)	14 322
Temperature, T (K)	293

4.2.3. Closure Models

The gas phase was solved using LPT, which solves the force balance on each bubble. Therefore, appropriate force closure models must be specified to obtain an accurate solution and achieve coupling with the continuous phase. The gravity and buoyancy forces are well known and can be specified directly. However, the other closure models must be chosen based on consideration of the experimental conditions. In the experimental work of Simiano (2005), the slip velocity was measured, and the drag coefficient was calculated to be 0.44 (Dhotre and Smith, 2007). This value of the drag coefficient was also used in the simulations of Dhotre and Smith (2007) and Dhotre et al. (2009). No additional correction was made to the drag coefficient to account for swarm effects because the bubble plume was dilute (gas volume fractions were generally lower than 2%) in the experiments. The virtual mass force coefficient was also set to 0.5 based on the simulation study of Dhotre and Smith (2007).

The lift and the turbulent dispersion forces were also considered. Dhotre and Smith (2007) used 0.1 as the lift coefficient in their RANS simulations, while Dhotre et al. (2009) used a value of 0.5 in their LES simulations. Based on the Tomiyama (2002) lift model, the lift coefficient is between 0 and 0.288 for small bubbles with diameters less than 5 mm. However, Hessenkemper et al. (2019) performed experiments to investigate the lift coefficients for different bubble sizes and 0.5 seemed to be suitable for a bubble size around

2.5 mm. Therefore, the effect of the lift coefficient was investigated through a sensitivity study. Three lift coefficients were chosen in this study: 0.1, 0.288, and 0.5.

For the turbulent dispersion force, Dhotre and Smith (2007) used the Davidson (1990) model in their RANS simulations. However, Dhotre et al. (2009) did not include the turbulent dispersion force model in their LES simulations. Olsen and Skjetne (2016) used a random walk model from Gosman and Ioannides (1981) in their RANS simulations. In the literature, it is generally common practice to apply a turbulent dispersion model for RANS simulations, but it is not very common to apply such a model in LES. Thus, in this study, the turbulent dispersion model was only considered in the RANS cases. In these simulations, the random walk model from Gosman and Ioannides (1981) was used.

Both RANS and LES models were tested as turbulence modelling approaches in this validation case. The k-ε model with the bubble-induced turbulence model by Sato et al. (1981) was used in the RANS cases. For the LES cases, the Smagorinsky (1963) subgrid-scale (SGS) model with the coefficient, C_s, of 0.12 was used in conjunction with the Sato et al. (1981) model for bubble-induced turbulence.

4.3. Results and Discussion

This validation case was simulated using two turbulence models, two mesh refinements, and various lift coefficients to better understand the impact of these changes on the hydrodynamics predictions. Additionally, LES cases were simulated for different flow rates to study the effect that the flow rate has on the accuracy of the predictions. Supplemental RANS simulations were performed to evaluate the impact of the turbulent dispersion force model. The gas volume fraction, axial liquid velocity, axial gas velocity, and turbulent kinetic energy were plotted for the cases to facilitate comparisons and interpretation of the effects of different models.

4.3.1. LES Simulations

The validation case was first simulated using LES with the Smagorinsky (1963) SGS model and the Sato et al. (1981) model to account for bubble-induced turbulence. The LES cases include mesh refinement tests, a sensitivity study on the lift coefficient, and a study on the

impact of the injection flow rate. As mentioned earlier, three lift coefficients were chosen for the sensitivity analysis: 0.1, 0.288, and 0.5. The flow rate sensitivity study compared predictions at gas injection rates of 1.9, 7.5, and 15 NL/min. All simulations other than the flow rate sensitivity studies employed a gas flow rate of 7.5 NL/min. The presented results were time averaged for at least 100 seconds after the plume had reached steady state.

4.3.1.1. Mesh Refinement

For the two meshes tested, 0.5 was used as the lift coefficient to ensure consistency between the cases and to limit the number of influencing factors. Figure 4.4 shows the gas phase volume fraction profiles at three elevations. The gas phase fraction profiles obtained from the coarse and fine meshes are similar. Although the profile for the coarse mesh matches the experimental data along the centerline at 0.35 m, there is underprediction at 0.75 m and overprediction at 1.1 m. The fine mesh follows a similar trend, except that the 0.35 m profile overpredicts at the experimental value at the centerline. The underpredictions at the centerline are balanced by the increased width of the predicted profiles in the radial direction. Overall, the shapes match well, and the larger inconsistencies at the 1.1 m elevation could be effects from liquid circulation around the free surface (at 1.5 m).

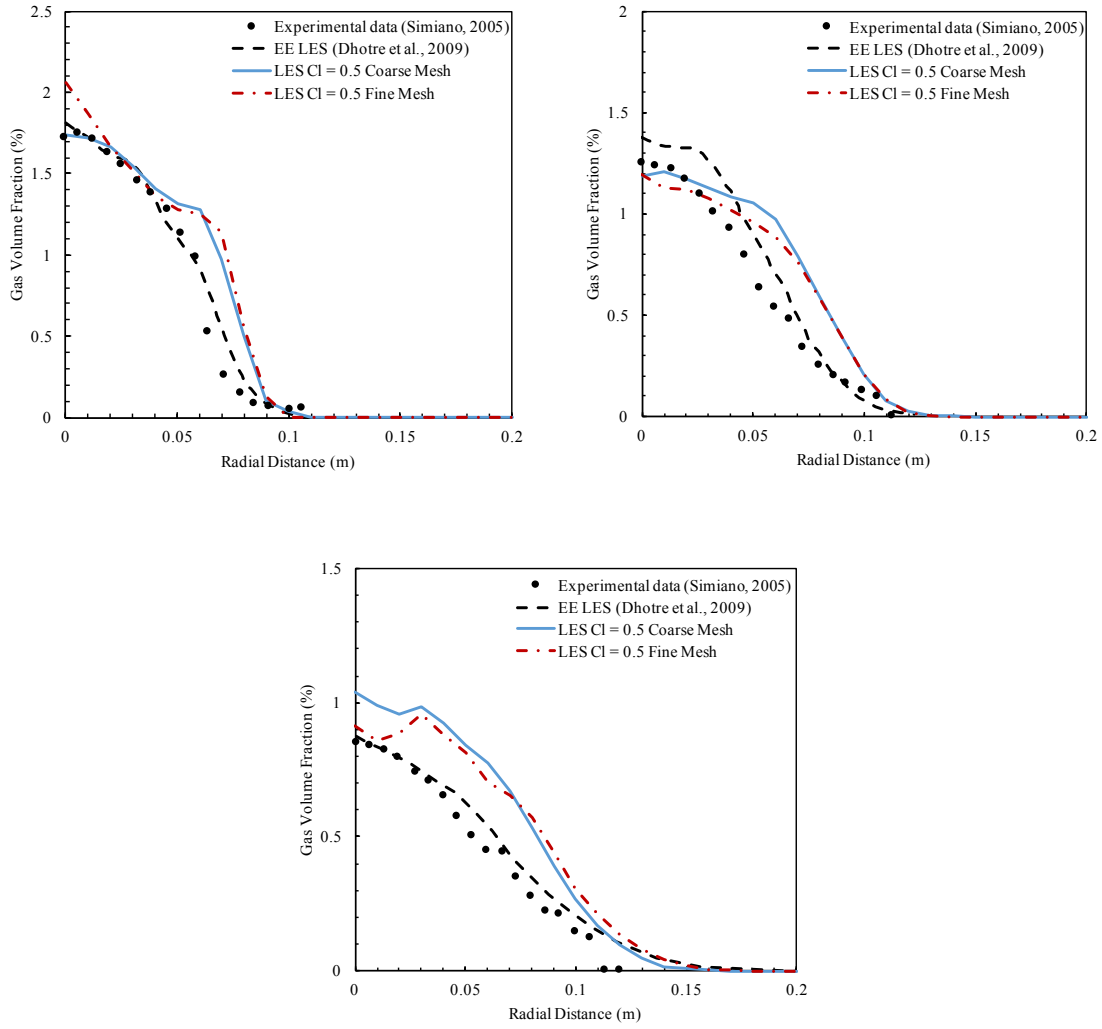

Figure 4.4: Gas volume fraction profiles at 0.35 m (top left), 0.75 m (top right), and 1.1 m (bottom) above the bottom of the tank for the LES mesh refinement simulations. The gas injection rate is 7.5 NL/min.

In the experiments of Simiano (2005), the gas volume fraction and the axial bubble velocity were measured by optical probes and the author stated that the optical probes always overestimate the axial bubble velocity by 2-4%. However, the author did not state the accuracy of the gas volume fraction measurements. Kiambi et al. (2003) performed calibration experiments using the same optical probes with bubbles of a similar size at 2.15 mm. They concluded that the optical probes underestimate the gas volume fraction by at least 14%. It is possible to use the gas volume fraction and gas velocity measurements from Simiano (2005) to calculate the measured gas flow rate at various elevations. Since the gas injection rate is known and the measurement error on the gas velocity is relatively low, it

is then possible to estimate the measurement underestimation error for the gas volume fraction based on the offset between the known and measured gas flow rates. Based on this analysis, the underestimation error of the gas phase volume fraction in the measurements was calculated to be approximately 42%. Considering this possible offset in the experimental measurements, the predicted gas volume fraction profiles are quite reasonable.

The axial gas velocity profiles for both meshes are shown in Figure 4.5. Both meshes predict similar results. The centerline velocity is overpredicted compared to the experimental data at all three heights, although this is less significant at 0.75 m and 1.1 m. These results are consistent with those presented in Figure 4.4. Note that the predicted axial gas velocity is incorrect at high radial distance due to the averaging error at very low phase fractions in the Lagrangian phase. The averaging method used to calculate the averaged bubble velocity takes the ratio of the total particle velocity and the total particle number in the same cell and averages it spatially. The averaging error of the bubble velocity at high radial distance is caused by the small number of bubbles that exist in the cells near the edge of the plume.

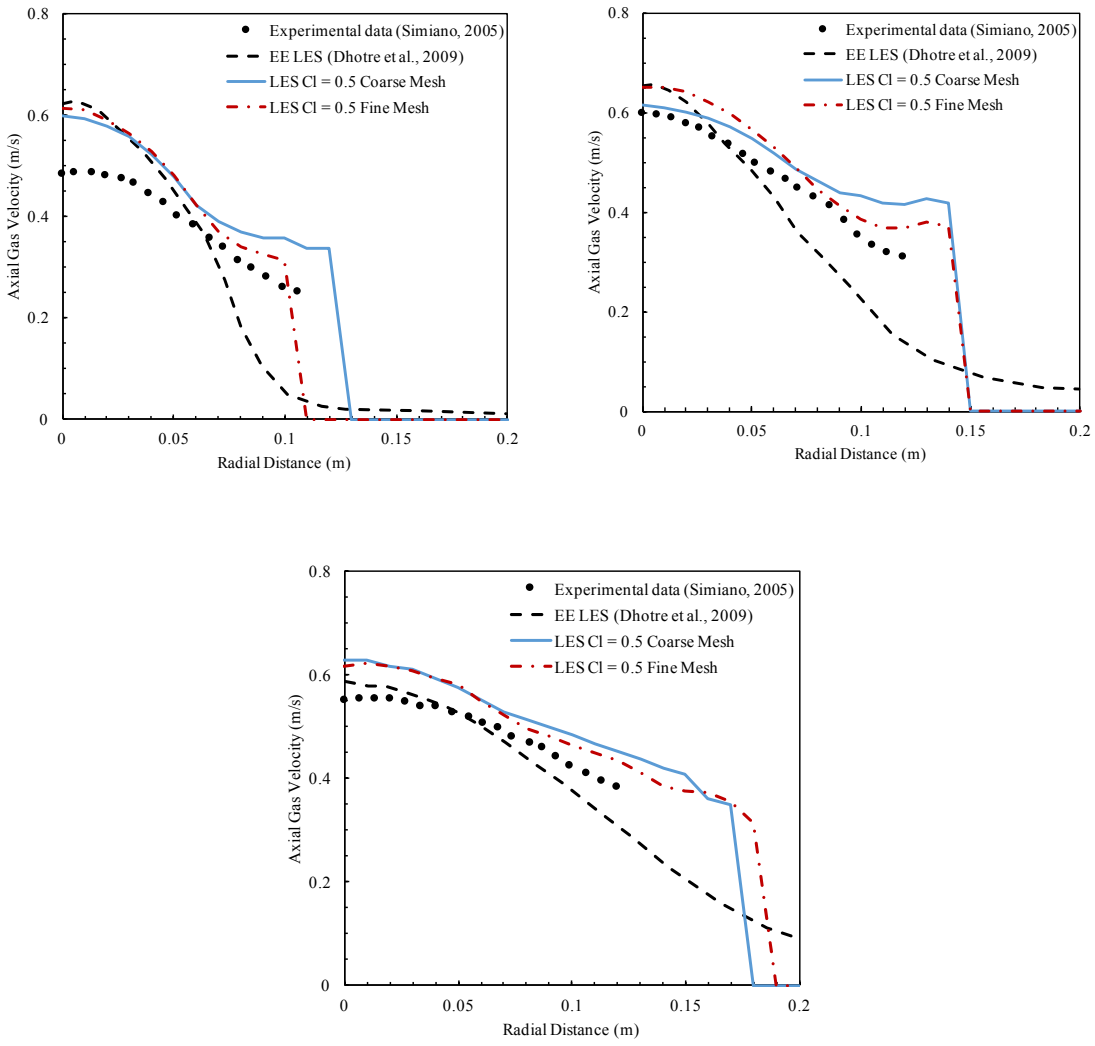

Figure 4.5: Axial gas velocity profiles at 0.35 m (top left), 0.75 m (top right), and 1.1 m (bottom) above the bottom of the tank for the LES mesh refinement simulations. The gas injection rate is 7.5 NL/min.

Figure 4.6 shows the axial liquid velocity profiles at three elevations. The generated profiles are similar for both meshes in terms of plume radius and centerline velocity value, except for the 0.75 m elevation. For the 0.75 m elevation, the coarse mesh yields an underprediction of the experimental value at the centerline and an overprediction at higher radial distance. In general, the centerline velocity is overpredicted for the 0.35 m elevation, while the values are much closer to the experimental results for 0.75 and 1.1 m elevations. At the 0.75 m elevation, the velocity tends to be overpredicted along the radius away from

the centerline. The results for the 0.35 and 1.1 m elevations match well with the simulated result of Dhotre et al. (2009).

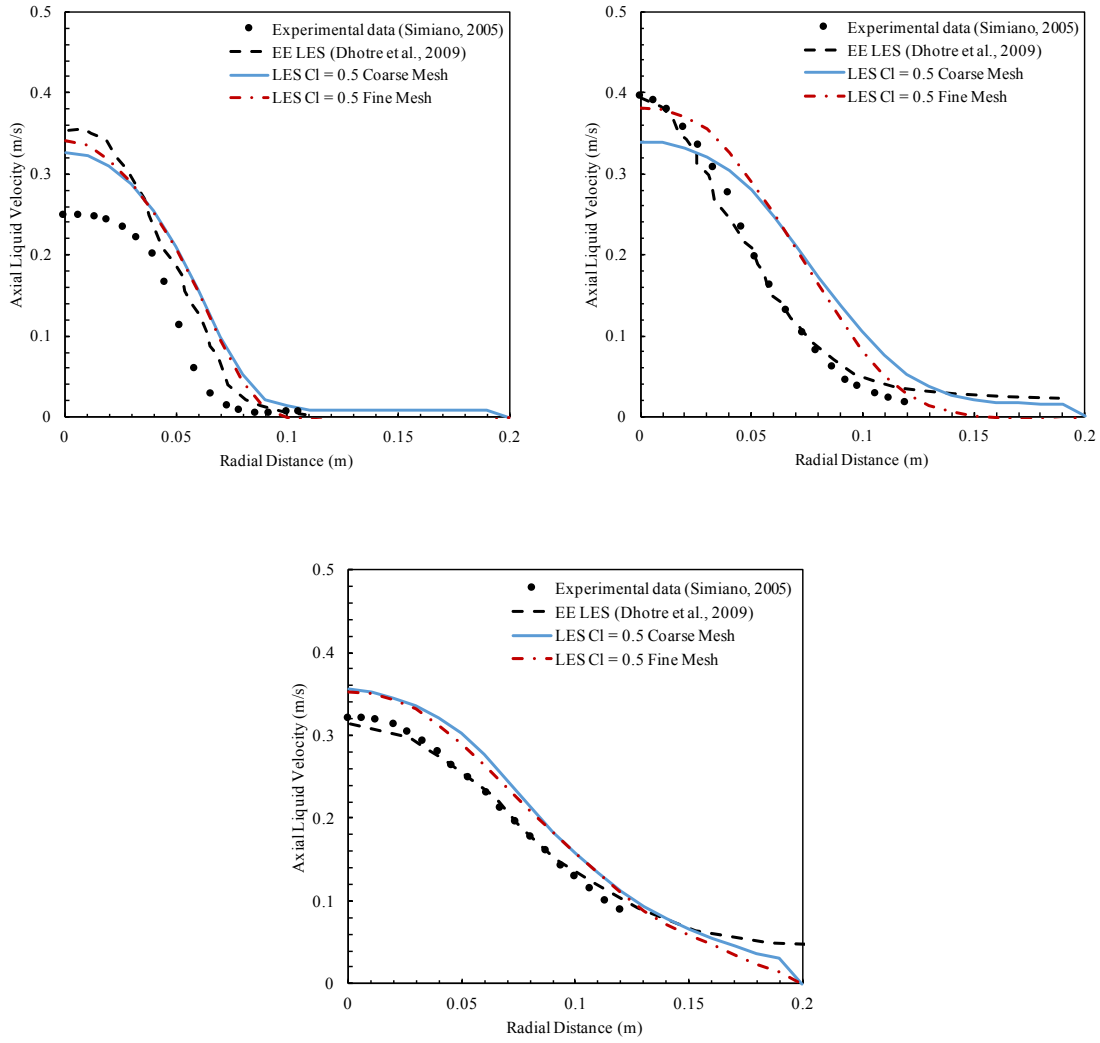

Figure 4.6: Axial liquid velocity profiles at 0.35 m (top left), 0.75 m (top right), and 1.1 m (bottom) above the bottom of the tank for the LES mesh refinement simulations. The gas injection rate is 7.5 NL/min.

The turbulent kinetic energy profiles are shown in Figure 4.7. The fine mesh provides a smoother profile than the coarse mesh. The profiles obtained from both meshes have similar shapes when compared to the data of Simiano (2005) and Dhotre et al. (2009). However, they have overpredicted the experimental and underpredicted the simulated turbulent kinetic energy at 0.35 m. The peak is still at the same location. At 0.75 m, the coarse mesh profile overpredicted the turbulent kinetic energy, while the fine mesh

underpredicted the peak but followed the measured shape more closely. Both meshes overpredicted the turbulent kinetic energy at 1.1 m, but the one from the fine mesh has a slightly closer centerline value when compared to the experimental data.

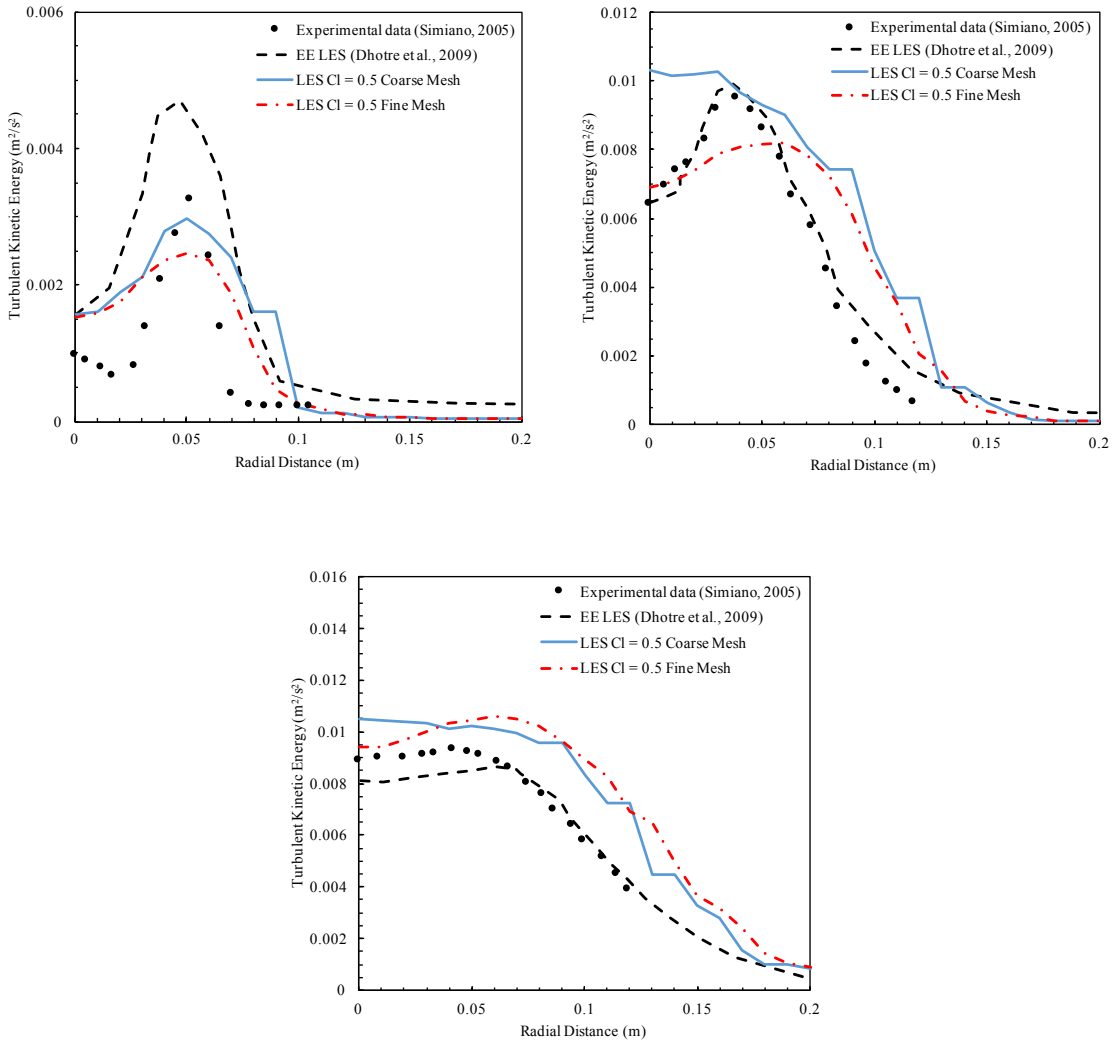

Figure 4.7: Turbulent kinetic energy profiles at 0.35 m (top left), 0.75 m (top right), and 1.1 m (bottom) above the bottom of the tank for the LES mesh refinement simulations. The gas injection rate is 7.5 NL/min.

The results seem to indicate that mesh refinement produces similar results for the LES model. Moreover, the general shape and approximate values predicted by the LPT-VOF model are in agreement with the experimental data and the simulation data from the EE model.

4.3.1.2. Lift Coefficient Study

The lift coefficient study used lift coefficients of 0.1, 0.288 and 0.5, and was performed on the coarse mesh to save computational time because the results obtained from both meshes were similar. Figure 4.8 shows the gas phase fraction profiles at three elevations. At 0.35 and 0.75 m, the cases with the lift coefficients of 0.1 and 0.288 overpredict the gas volume fraction towards the middle of the plume compared to the experimental data. The case with 0.5 as the lift coefficient provides the best overall fit, but overestimates the gas fraction away from the centerline at elevations of 0.35 and 0.75 m. All three profiles overpredict the gas volume fraction at 1.1 m, but a lift coefficient of 0.5 is the closest to the experimental data and the results from Dhotre et al. (2009). The predicted plume radius also matches the experimental data relatively well for a lift coefficient of 0.5. These results seem to indicate that a lift coefficient of 0.5 is the most suitable for bubble sizes around 2.5 mm.

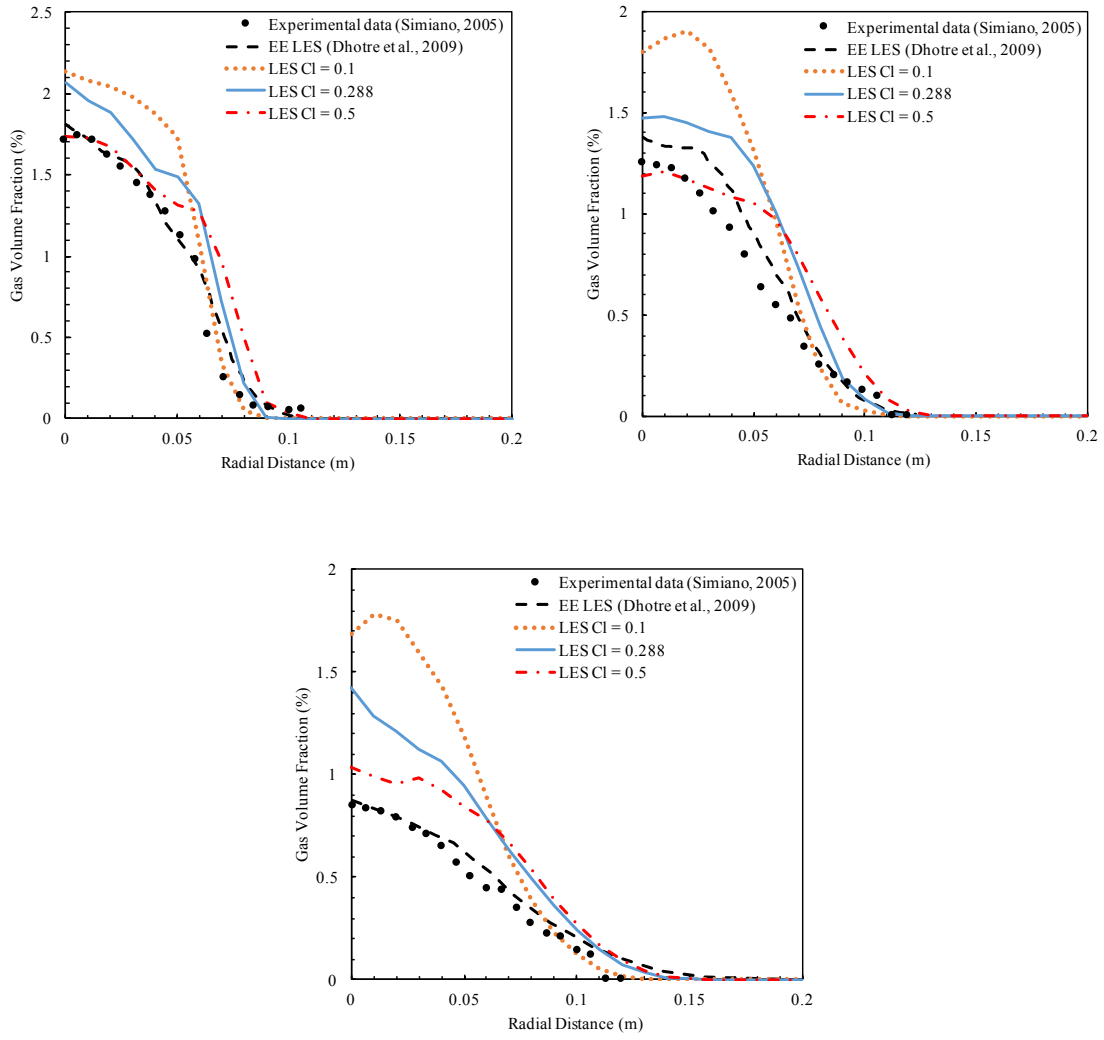

Figure 4.8: Gas volume fraction profiles at 0.35 m (top left), 0.75 m (top right), and 1.1 m (bottom) above the bottom of the tank for the LES lift coefficient study simulations. The gas injection rate is 7.5 NL/min.

The axial gas velocity profiles at three elevations are shown in Figure 4.9. All three profiles are very similar at an elevation of 0.35 m, but they all overestimate the axial gas velocity relative to the experimental data. At 0.75 m, all the three profiles overpredict the axial gas velocity, but the difference between the predictions and the experimental data has decreased. At 1.1 m, they all overestimate the axial gas velocity, but the overprediction is not very high.

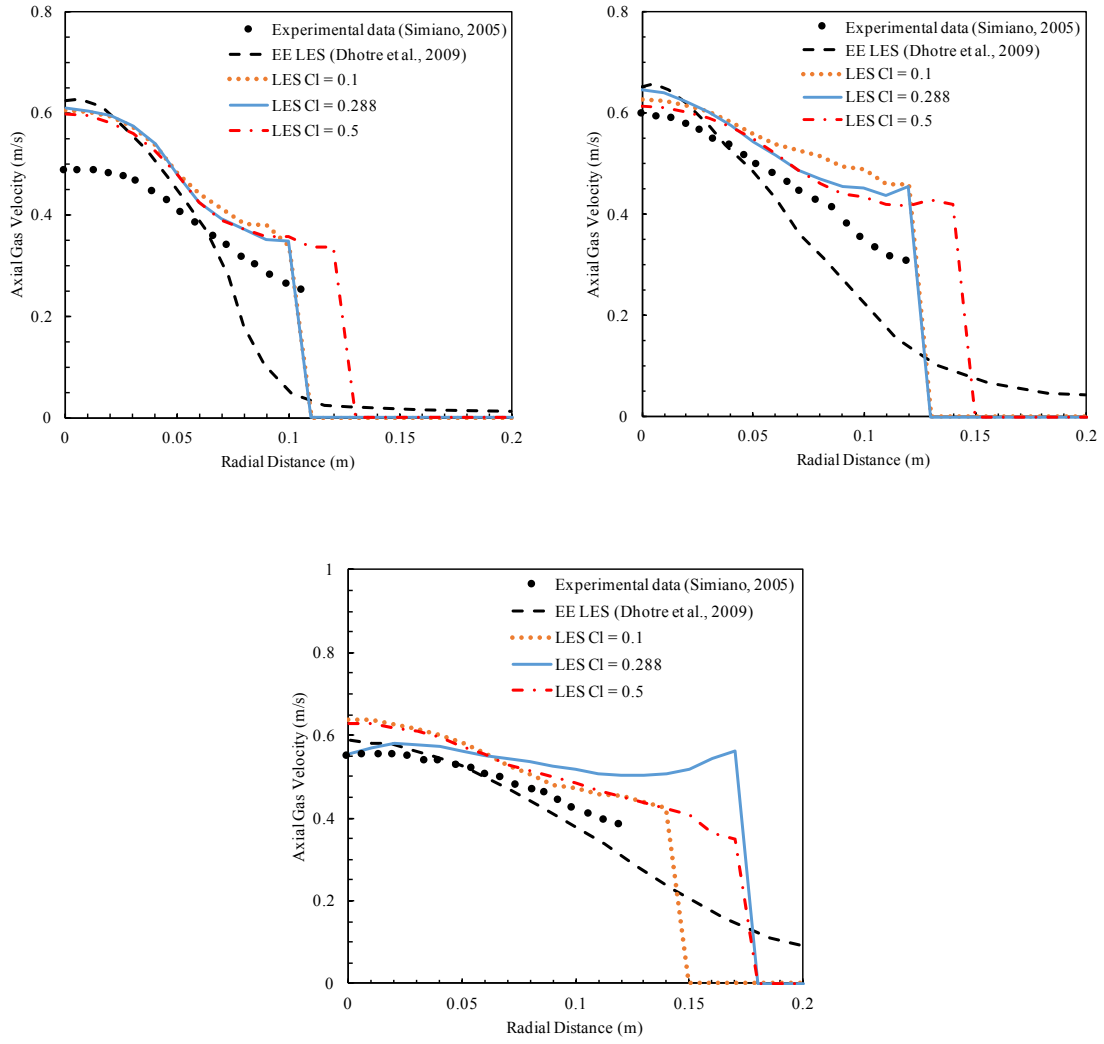

Figure 4.9: Axial gas velocity profiles at 0.35 m (top left), 0.75 m (top right), and 1.1 m (bottom) above the bottom of the tank for the LES lift coefficient study simulations. The gas injection rate is 7.5 NL/min.

Figure 4.10 shows the axial liquid velocity profiles at three elevations. The profiles are similar at all elevations, with the exception of the centerline prediction from the case with a lift coefficient of 0.288 at 1.1 m. In this case, the centerline velocity is underpredicted relative to the experimental data and the other simulations. The underprediction of centerline velocity at 1.1 m of elevation for the 0.288 lift coefficient is not currently understood, but it could be due to a small time averaging error. The liquid velocity is generally overpredicted by the simulations, but the predictions seem to improve at higher elevations for all the three cases.

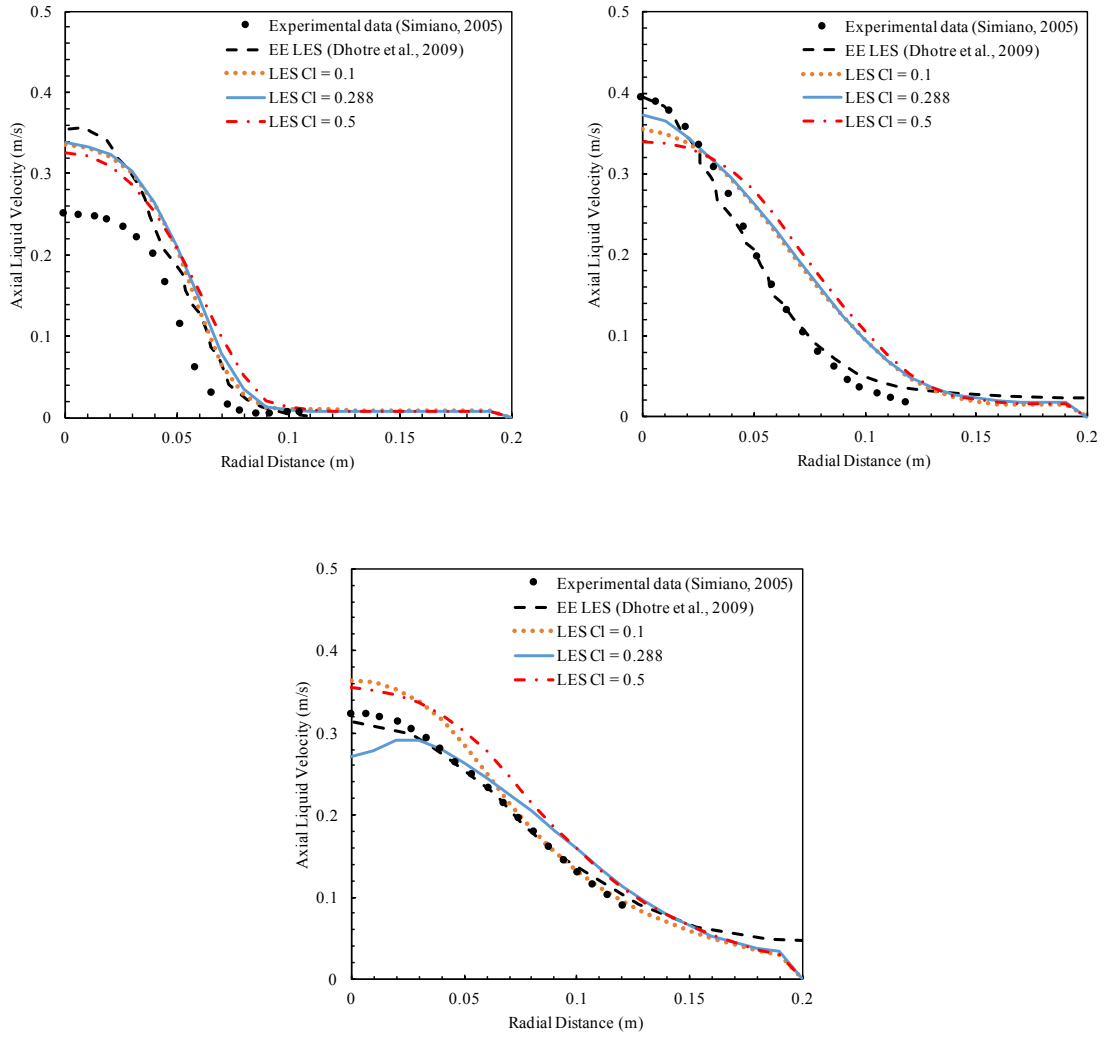

Figure 4.10: Axial liquid velocity profiles at 0.35 m (top left), 0.75 m (top right), and 1.1 m (bottom) above the bottom of the tank for the LES lift coefficient study simulations. The gas injection rate is 7.5 NL/min.

The turbulent kinetic energy profiles at three elevations are shown in Figure 4.11. The case with 0.1 as the lift coefficient overestimates the turbulent kinetic energy at 0.35 m, while the other two results are closer to the experimental data with small overpredictions. In general, increasing the lift coefficient seems to have a damping effect on the turbulent kinetic energy. All three cases overestimate the turbulent kinetic energy at 0.75 m and 1.1 m, but the case with the lift coefficient of 0.5 provides a prediction closer to the experimental data.

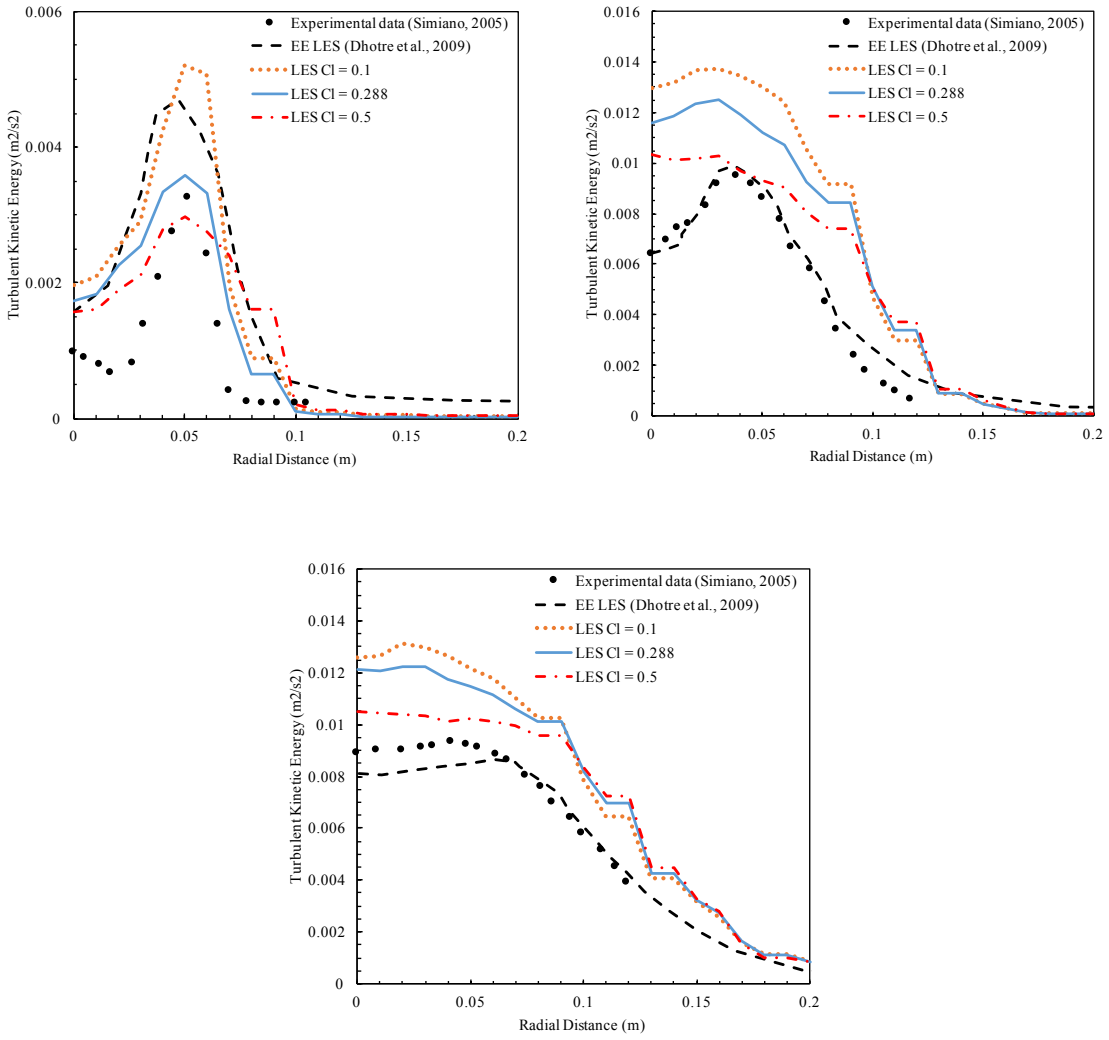

Figure 4.11: Turbulent kinetic energy profiles at 0.35 m (top left), 0.75 m (top right), and 1.1 m (bottom) above the bottom of the tank for the LES lift coefficient study simulations. The gas injection rate is 7.5 NL/min.

Although many researchers have used the Tomiyama (2002) lift model for smaller bubble sizes, the results show that a lift coefficient of 0.5 provides a better overall fit to the experimental data in this case. Based on the experiments by Hessenkemper et al. (2019), the lift coefficient for the bubble size around 2.5 mm is close to 0.5. It is not surprising that the Tomiyama (2002) lift model did not provide the optimal lift coefficient for this simulation because the current range of Reynolds number falls outside of the range used to develop this correlation.

The time-averaged and the instantaneous plume shapes from the LES case with a lift coefficient of 0.5 are displayed in Figure 4.12. The highly transparent blue planes above the plumes represent the free surface. The contours of 0.01% of the gas phase fractions are colored with a transparent light blue, while the bubbles are shown as the dark blue points within them. The instantaneous plume shows more wobbling than the time-averaged plume, as expected for an LES case.

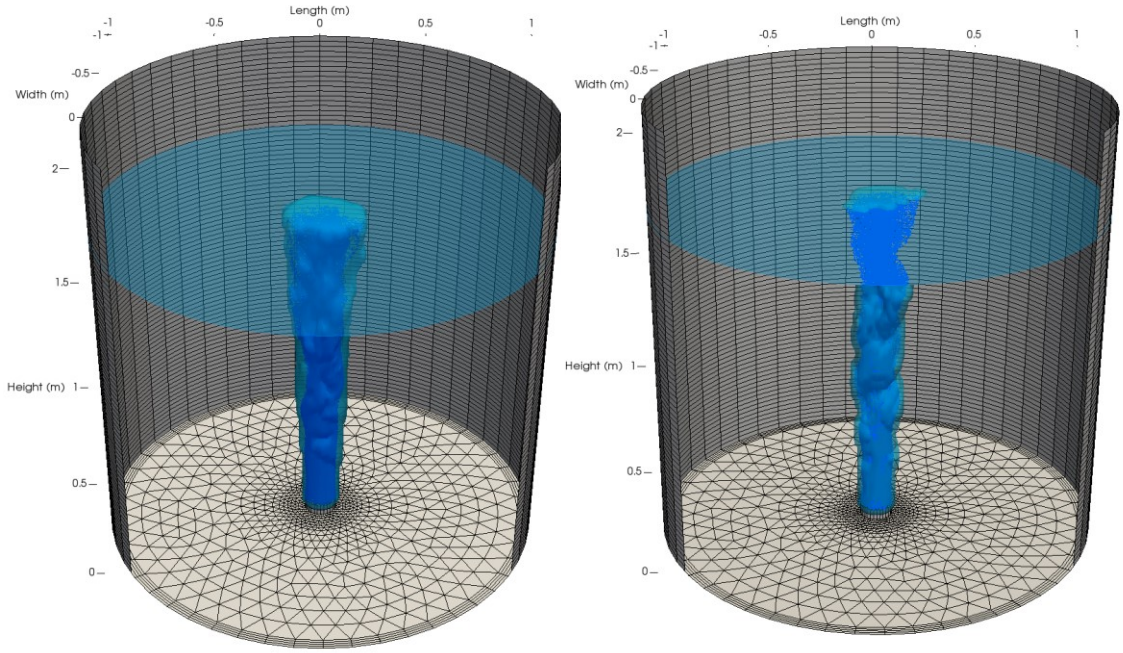

Figure 4.12: Screenshots of the three-dimensional time-averaged (left) and instantaneous (right) bubble plumes in the LES cases with the lift coefficient of 0.5. The gas injection rate is 7.5 NL/min.

In order to verify that no mass was lost in the transition between the LPT method and the VOF gas phase, the mass flow rate of the gas was calculated at the inlet, 0.35 m, 0.75 m, 1.1 m, and 1.95 m (just below the top boundary). The results showed that the mass flow rate differed by approximately 1.3% between the inlet and outlet. This indicated that the mass was conserved in the simulations to within numerical tolerances.

4.3.1.3. Flow Rate Comparisons

Two other gas injection flow rates were also simulated to investigate the effect of gas superficial velocity on the fluid dynamics predictions. The same LES configuration from above was also used in this study. The lift coefficient was set to 0.5 because this was shown

to provide the best overall fit in the previous section. Additionally, the coarse mesh was used to reduce computational time. One lower flow rate of 1.9 NL/min and one higher flow rate of 15 NL/min was chosen from the experimental data of Simiano (2005). Experimental data was only available for an elevation of 0.75 m for these flow rates. The flow rates were converted to bubble injection rates and bubble velocities using the method outlined in section 4.2.2 and specified as boundary conditions at the inlet. The corresponding changes to the Lagrangian phase boundary conditions at the inlet are summarized in Table 4.5.

Table 4.5: Air Bubble Inlet Conditions Used in the Flow Rate Study

Property	Value at 1.9 NL/min injection rate	Value at 15 NL/min injection rate
Bubble velocity at the inlet, $\vec{u}_b$ (m/s)	0.11	0.85
Bubble injection rate (bubbles/s)	3 628	28 644

Figure 4.13 shows a comparison between the experimental and predicted profiles for the gas volume fraction, axial gas velocity, and axial liquid velocity at a height of 0.75 m. For the lower flow rate case, the phase fraction is underpredicted at the centerline, and the radius of the plume is overpredicted. The axial gas velocity is also overpredicted, especially near the edge of the plume. For the higher flow rate case, the gas volume fraction, axial gas velocity, and plume radius are overpredicted. In this case, the axial liquid velocity near the centerline is predicted accurately, but the velocity is generally overpredicted. Generally, it seems that the results at higher flow rates are predicted more accurately by the current model parameterization.

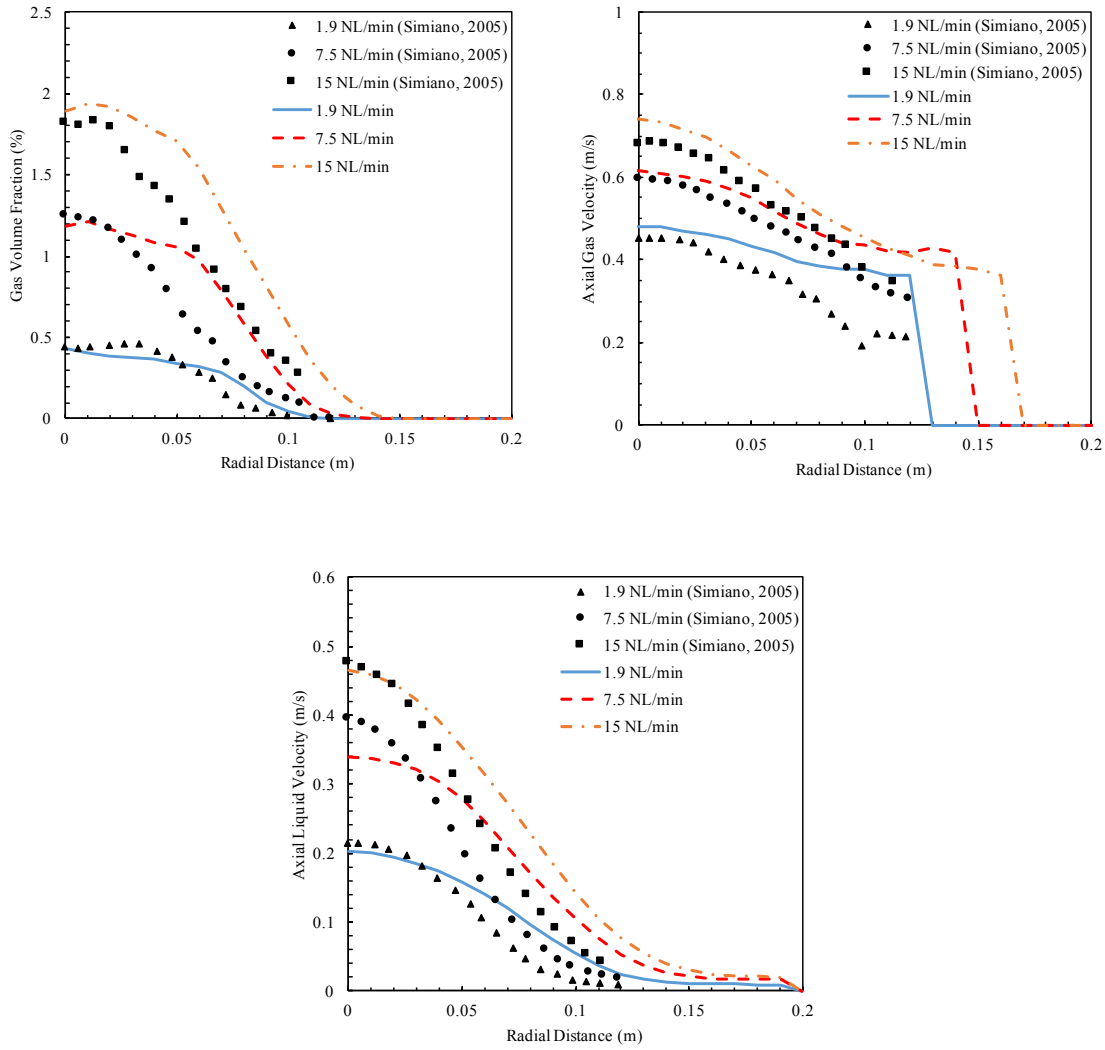

Figure 4.13: Gas volume fraction (top left), axial gas velocity (top right), and axial liquid velocity (bottom) profiles at 0.75 m above the bottom of the tank for the LES flow rate comparisons simulations.

4.3.2. RANS Simulations

The validation case was also simulated using RANS with the k-ε turbulence model and the Sato et al. (1981) model to account for bubble-induced turbulence. The RANS cases include mesh refinement tests, a sensitivity study on the turbulent dispersion force model, and a sensitivity study on the lift coefficient. Similar to the LES simulations, three lift coefficients were chosen for the sensitivity analysis: 0.1, 0.288, and 0.5. All simulations employed a gas flow rate of 7.5 NL/min. The presented results were time averaged for at least 100 seconds after the plume had reached steady state.

4.3.2.1. Mesh Refinement

A repeat of the mesh refinement test was performed for the RANS simulations to investigate the performance of the meshes with this turbulence modelling approach. The same two meshes (Figure 4.2 and Figure 4.3) were used in this study. The lift coefficient was chosen to be 0.5, based on the results from the LES cases, and the turbulent dispersion force was included in this test.

The predicted gas volume fraction profiles are shown in Figure 4.14. The results obtained from both meshes overpredict the gas volume fraction at all elevations, but the overprediction is greatest at the highest elevation. As shown in Figure 4.15, the predictions from both meshes give similar axial gas velocity profiles. Although the gas velocity is overpredicted compared to the experimental results, the predictions are closer at the centerline than the results of Dhotre and Smith (2007). The results from the fine mesh show slightly higher predictions of plume spreading. Considering the experimental accuracy associated with the gas volume fraction measurements, the predictions are relatively good.

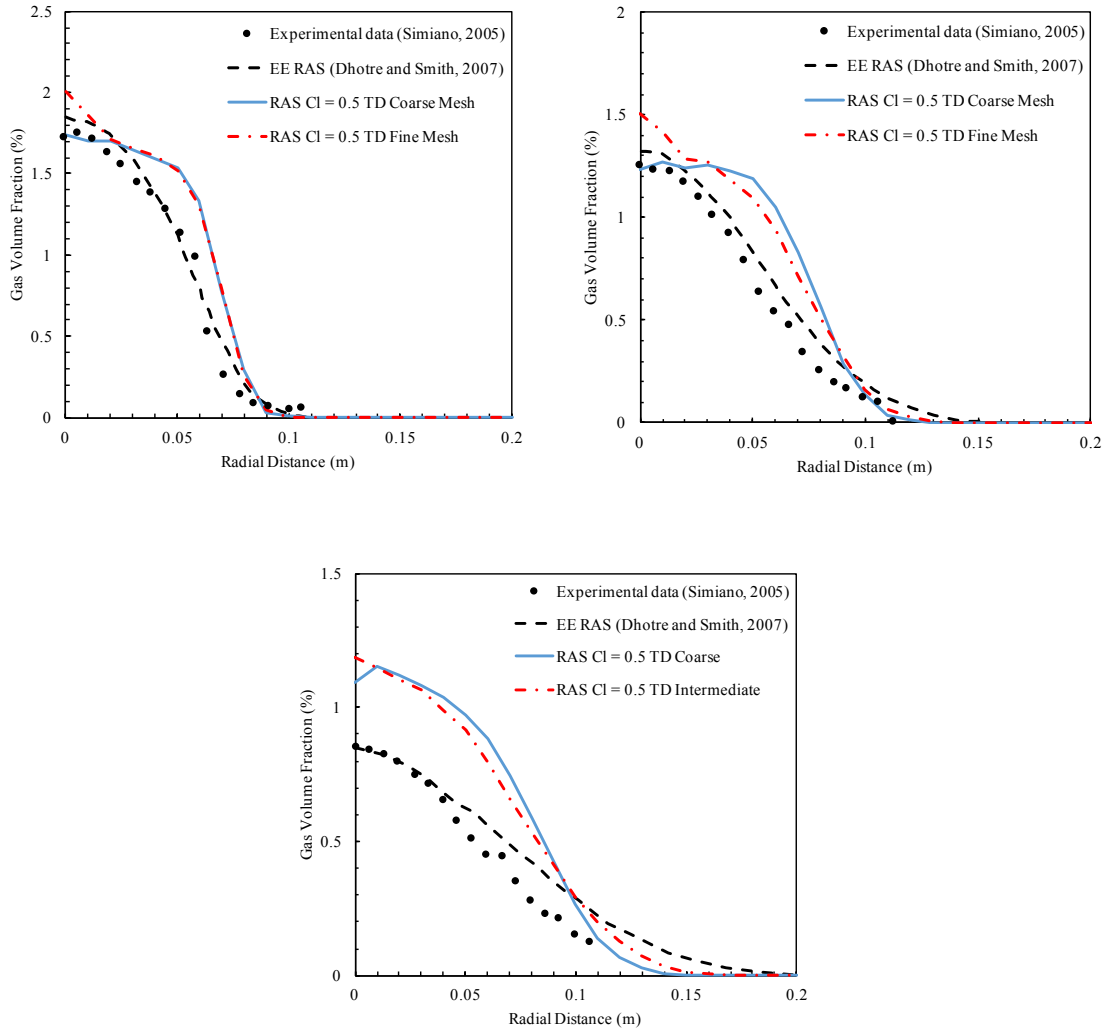

Figure 4.14: Gas volume fraction profiles at 0.35 m (top left), 0.75 m (top right), and 1.1 m (bottom) above the bottom of the tank for the RANS mesh refinement simulations. The gas injection rate is 7.5 NL/min.

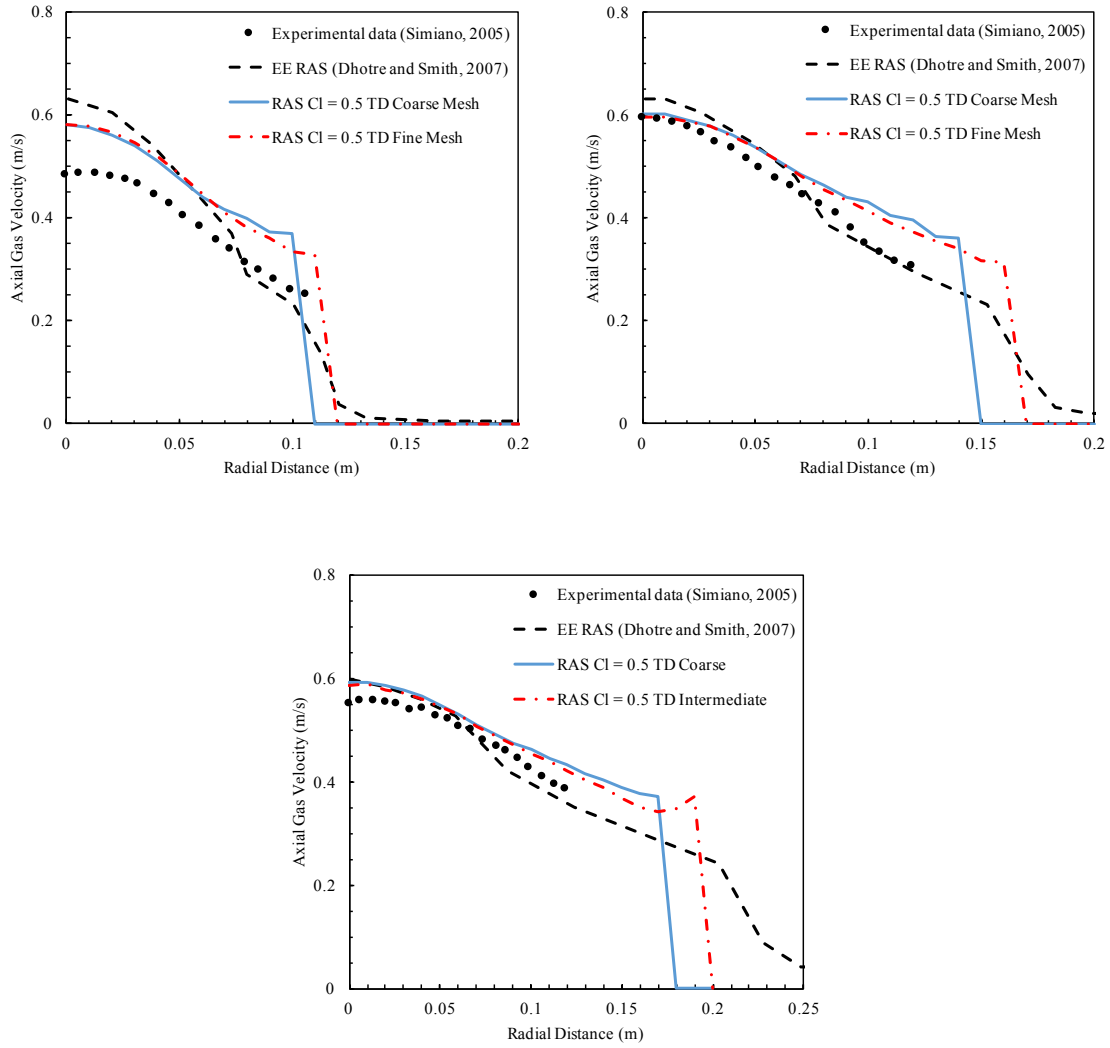

Figure 4.15: Axial gas velocity profiles at 0.35 m (top left), 0.75 m (top right), and 1.1 m (bottom) above the bottom of the tank for the RANS mesh refinement simulations. The gas injection rate is 7.5 NL/min.

The comparison between the predicted and experimental axial liquid velocities at three elevations is shown in Figure 4.16. The coarse mesh and the fine mesh give the similar predictions of the axial liquid velocity at all locations. Both meshes provide an overestimate of the axial liquid velocity at 0.35 m compared to the experimental data but provide a better prediction than the results from Dhotre and Smith (2007). The profiles obtained using both meshes underpredict the axial liquid velocity near the centerline at 0.75 m and overestimate it towards the edge of the plume, which follows a similar trend as predictions from Dhotre and Smith (2007). Similar conclusions can be made for the profiles

at 1.1 m, but the predictions are almost exactly the same as those of Dhotre and Smith (2007).

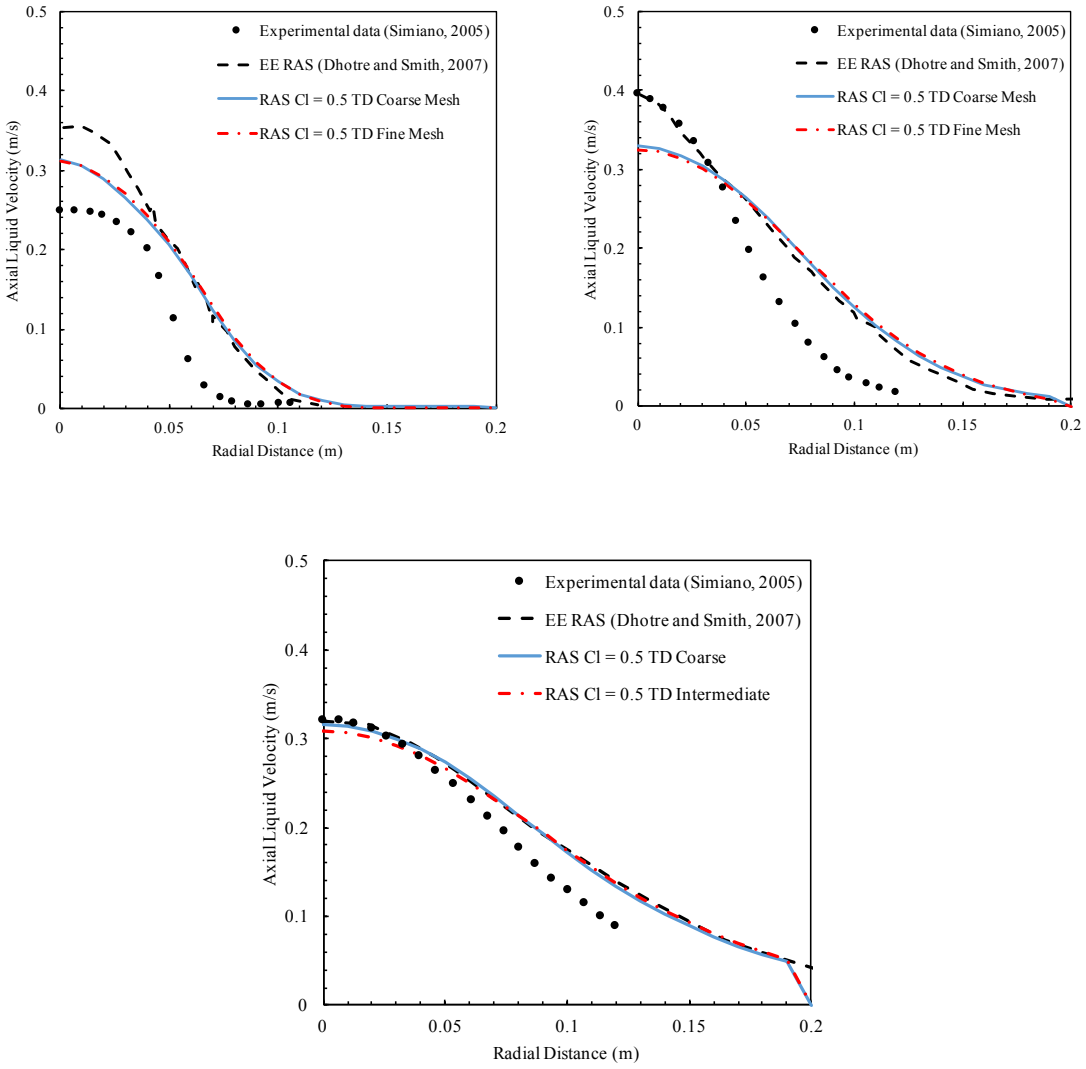

Figure 4.16: Axial liquid velocity profiles at 0.35 m (top left), 0.75 m (top right), and 1.1 m (bottom) above the bottom of the tank for the RANS mesh refinement simulations. The gas injection rate is 7.5 NL/min.

The turbulent kinetic energy profiles for both meshes at three elevations are shown in Figure 4.17. The two meshes provide similar predictions, with a small difference observed at the lowest elevation. The profiles generated by both meshes give similar shapes as the profiles from Dhotre and Smith (2007) at elevations of 0.35 and 0.75 m. The shapes of the two predicted profiles at 1.1 m are similar in shape to the experimental data and the

simulation results from Dhotre and Smith (2007). However, the turbulent kinetic energy away from the centerline is overpredicted.

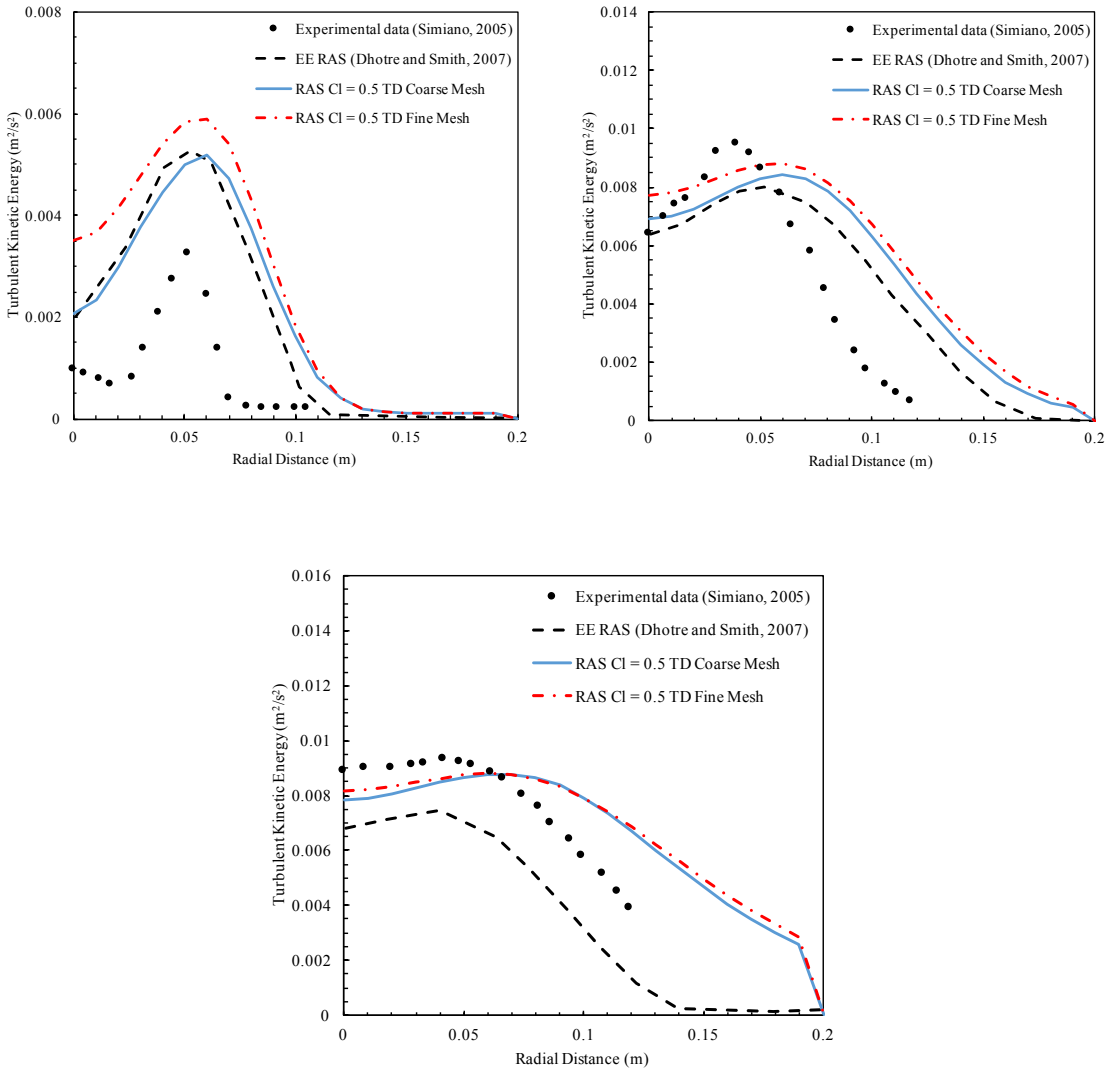

Figure 4.17: Turbulent kinetic energy profiles at 0.35 m (top left), 0.75 m (top right), and 1.1 m (bottom) above the bottom of the tank for the RANS mesh refinement simulations. The gas injection rate is 7.5 NL/min.

Overall, both meshes gave similar predictions for the gas volume fraction, axial gas velocity, axial liquid velocity, and turbulent kinetic energy profiles. The profiles for these variables were generally overpredicted by the simulation results, but the fit to the experimental data was generally good for the chosen parameterization. The predictions

were better at higher elevations for the axial gas and liquid velocities, while the gas volume fraction and turbulent kinetic energy predictions were better at lower elevations.

4.3.2.2. Turbulent Dispersion and Lift Coefficient Studies

The sensitivity of the predictions to the assumed lift coefficient and turbulent dispersion model were tested. The coarse mesh was chosen for these simulations to save computational time. The three lift coefficients were 0.1, 0.288 and 0.5, which are the same as the values used in the LES study. The effect of the turbulent dispersion model was also tested by performing simulations with and without the model for the case with a lift coefficient of 0.288.

The gas volume fraction profiles are shown in Figure 4.18. The results indicate that both the lift coefficient and the turbulent dispersion model have a significant impact on the predictions. The simulations that used a lift coefficient of 0.5 and the turbulent dispersion model included generally provided the best predictions of the gas volume fraction and plume radius. The turbulent dispersion model seems to primarily impact the shape of the predicted profile. Based on these results, it is clear that the turbulent dispersion model is necessary to provide reasonable predictions of the volume fraction profile shape. It is also apparent that a lift coefficient of 0.5 provides the best predictions. Although this value of the lift coefficient is reasonable based on available literature data, it is important to remember that there may not be a unique parameterization of the closure models that provides optimal results for all profiles.

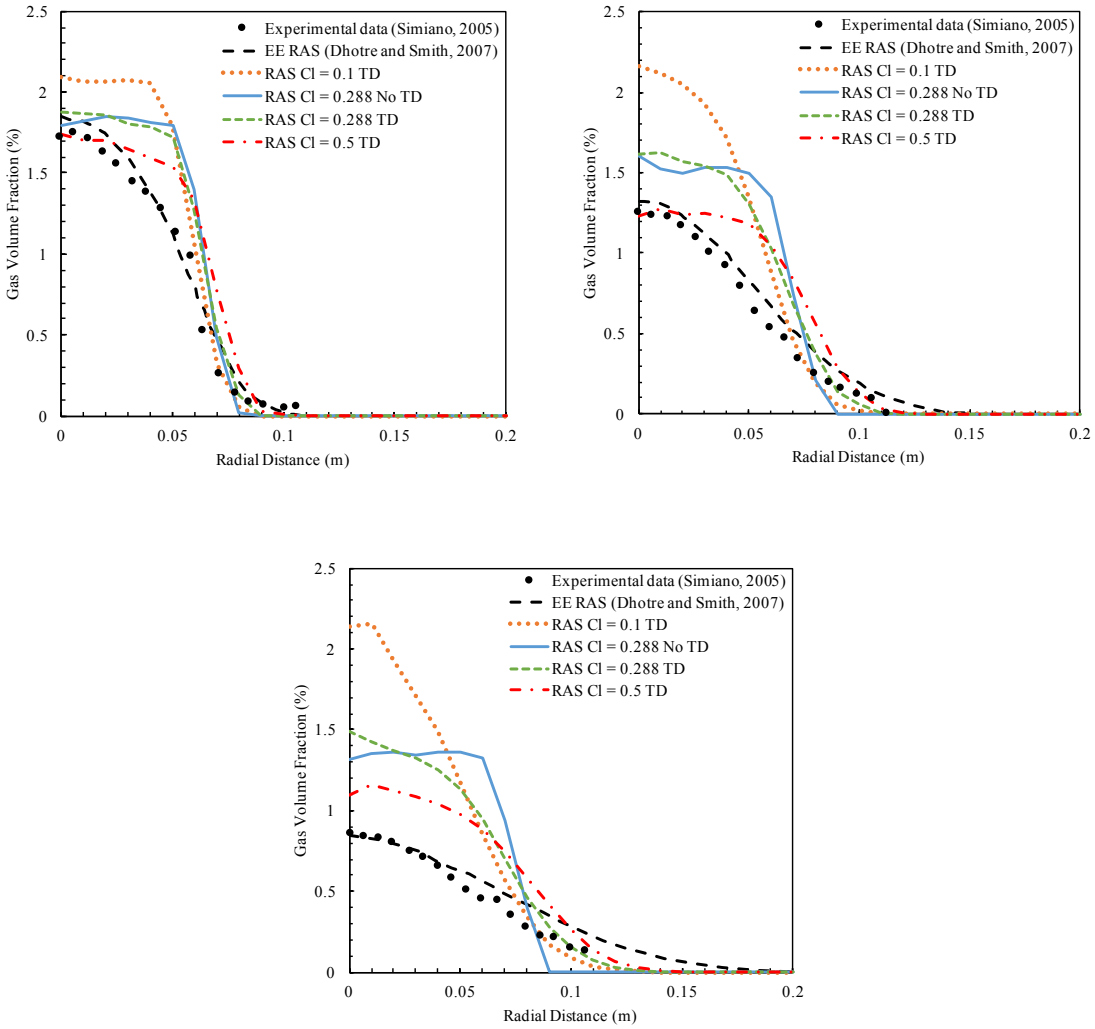

Figure 4.18: Gas volume fraction profiles at 0.35 m (top left), 0.75 m (top right), and 1.1 m (bottom) above the bottom of the tank for the RANS turbulent dispersion and lift coefficient studies simulations. The gas injection rate is 7.5 NL/min.

Figure 4.19 shows the axial gas velocity profiles at three elevations. The predicted profiles for the cases that used the turbulent dispersion model are very similar at all the three elevations, but the case with the lift coefficient of 0.5 shows more plume spreading at an elevation of 1.1 m. The predicted plume spreading is too narrow for the case that did not use the turbulent dispersion model. The predictions match the experimental data better at the elevations of 0.75 and 1.1 m. This is likely because the results at the lowest elevation are most strongly influenced by the gas injection configuration, which was difficult to match exactly in the simulations.

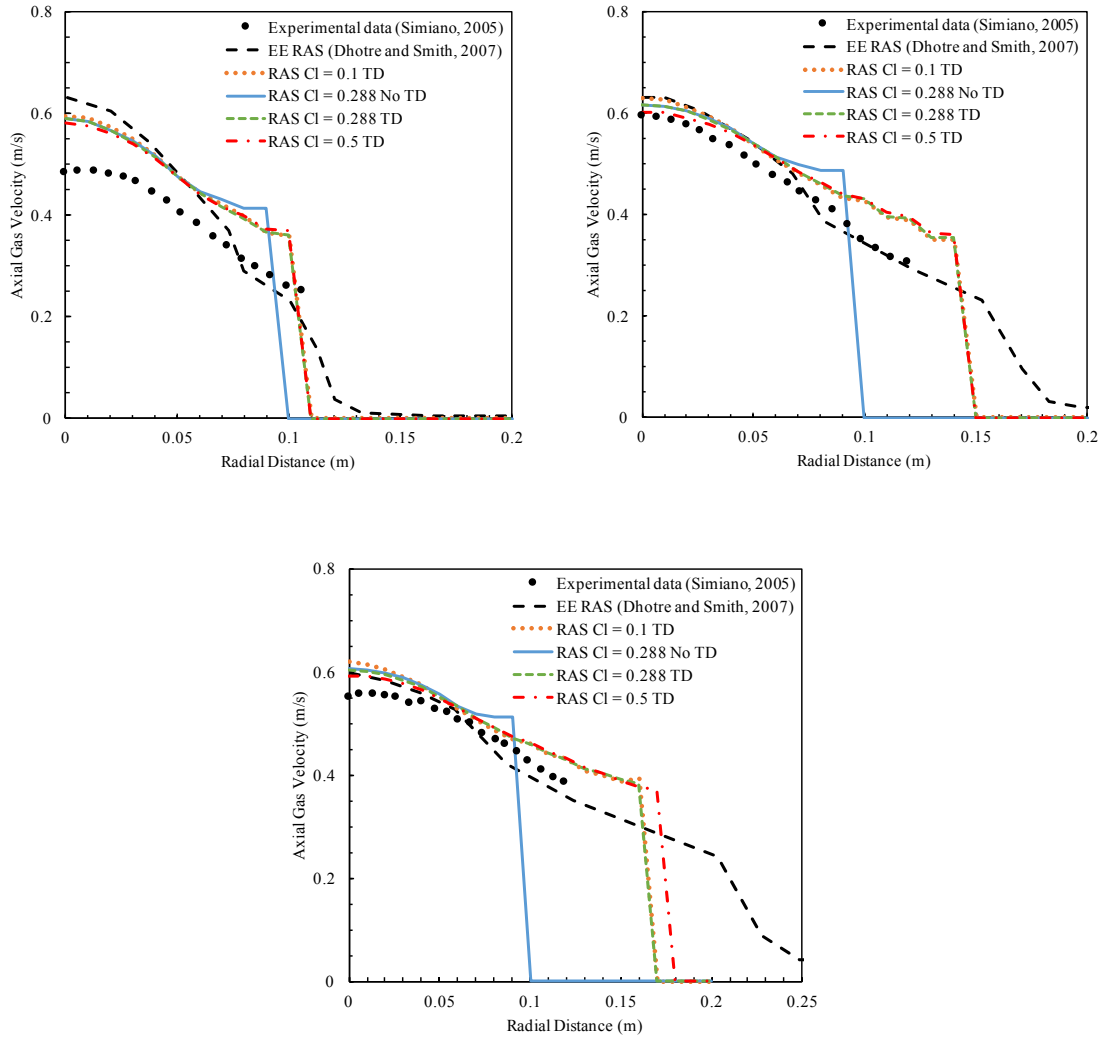

Figure 4.19: Axial gas velocity profiles at 0.35 m (top left), 0.75 m (top right), and 1.1 m (bottom) above the bottom of the tank for the RANS turbulent dispersion and lift coefficient studies simulations. The gas injection rate is 7.5 NL/min.

The axial liquid velocity profiles at three elevations are shown in the Figure 4.20. The results show that all four profiles are overlapping. Thus, the turbulent dispersion force and the lift coefficient do not seem to affect the axial liquid velocity significantly. The results at 0.35 m overpredict the axial liquid velocity compared to the experimental data, but they match better than the results from Dhotre and Smith (2007). The profiles underestimate the axial liquid velocity from the centerline to the radial distance of 0.03 m but overpredict it at greater radial distances compared to the experimental data at 0.75 m. The results match

the results from Dhotre and Smith (2007) at 1.1 m but slightly overestimate the axial liquid velocity compared to the experimental data.

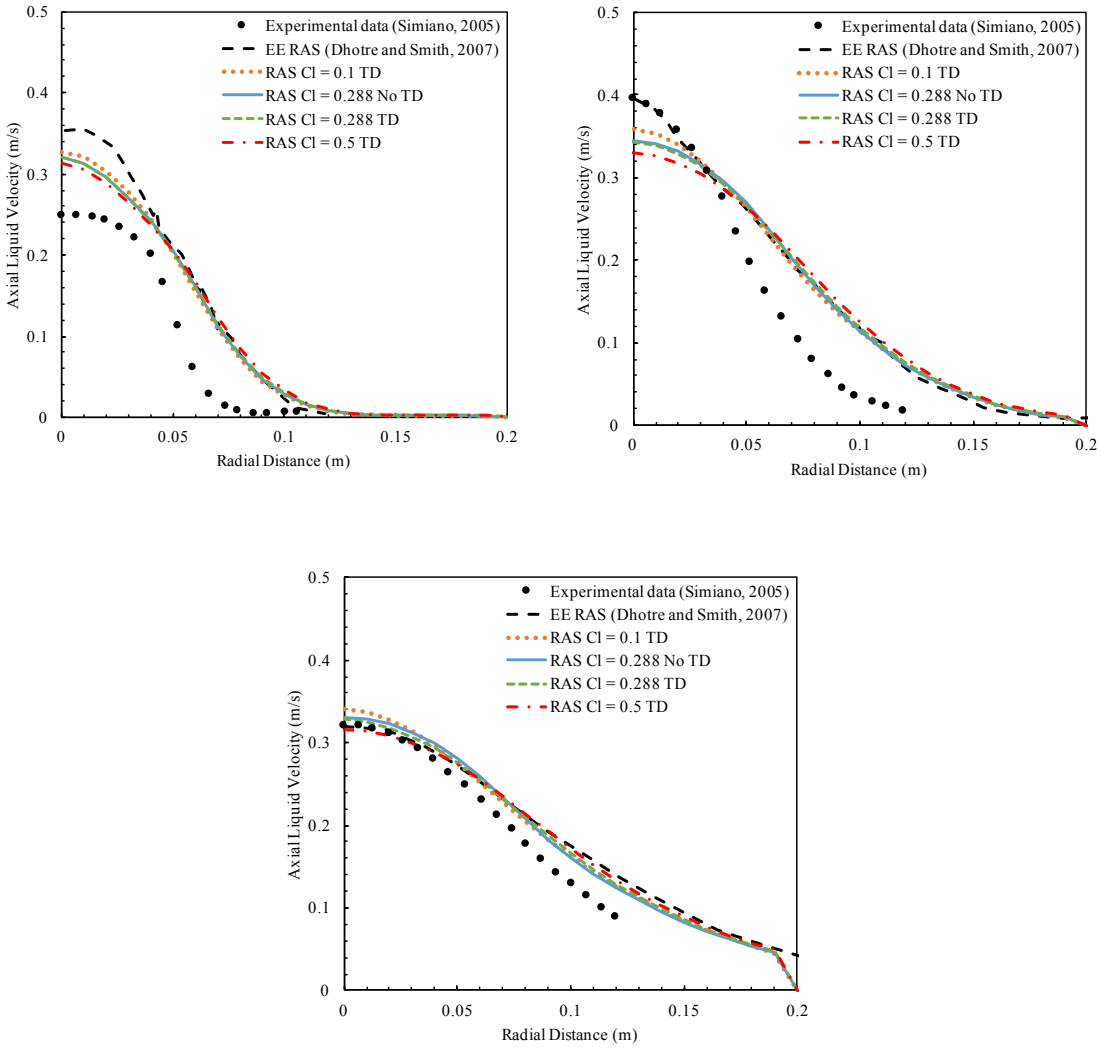

Figure 4.20: Axial liquid velocity profiles at 0.35 m (top left), 0.75 m (top right), and 1.1 m (bottom) above the bottom of the tank for the RANS turbulent dispersion and lift coefficient studies simulations. The gas injection rate is 7.5 NL/min.

Figure 4.21 shows the profiles of the turbulent kinetic energy at three elevations. At 0.35 m, the four model combinations provide similar predictions. The turbulent kinetic energy was overpredicted compared to the experimental data but matched the results from Dhotre and Smith (2007). At 0.75 and 1.1 m, the four profiles had similar shapes, but the cases with the lift coefficients of 0.1 and 0.288 overpredicted the turbulent kinetic energy

compared to the experimental data. Although the case with a lift coefficient of 0.5 does not match the experimental data exactly, it generally provides reasonable predictions of the profile shapes and turbulent kinetic energy levels.

From the results of the turbulent kinetic energy in both the LES and RANS simulations, it was challenging to match the experimental data and the results from the EE simulations. This is because the modelling method of phase fraction in the turbulence model is different between the EE method and the developed LPT-VOF solver. Further work should focus on developing improved turbulence modelling approaches and better parameterizations to improve model fit.

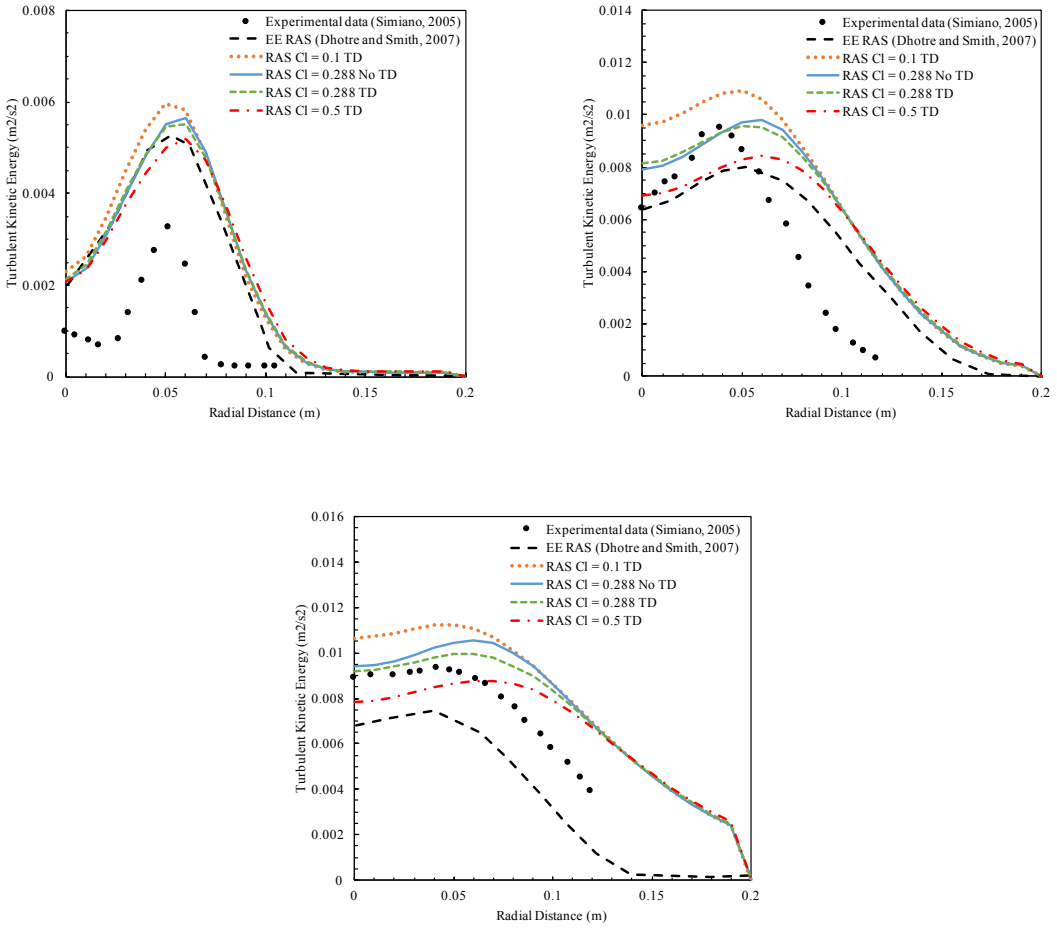

Figure 4.21: Turbulent kinetic energy profiles at 0.35 m (top left), 0.75 m (top right), and 1.1 m (bottom) above the bottom of the tank for the RANS turbulent dispersion and lift coefficient studies simulations. The gas injection rate is 7.5 NL/min.

Based on these results, it is clear that the turbulent dispersion affects the spreading of the bubble plumes, but it does not seem to have a significant impact on the axial liquid velocity and the turbulent kinetic energy. The lift coefficient does not seem to affect the axial gas and liquid velocities significantly, but it does strongly affect the gas volume fraction spreading and the turbulent kinetic energy peak. Higher lift coefficients result in more spreading of the plume in the radial direction, which leads to lower gas volume fraction near the centerline of the plumes. Overall, the lift coefficient of 0.5 seems to yield the best results for the current parameterization.

The time-averaged plume shape from the RANS simulation with the lift coefficient of 0.5 and the turbulent dispersion model is displayed in Figure 4.22. As mentioned in the LES section, the highly transparent blue plane above the plume represents the free surface and the contour of 0.01% of the gas fraction is colored by the light blue, while the bubbles are shown in dark blue. The plume generated by the RANS model had less wobbling than the plume in the LES cases due to the nature of the RANS model, but the time-averaged results were similar.

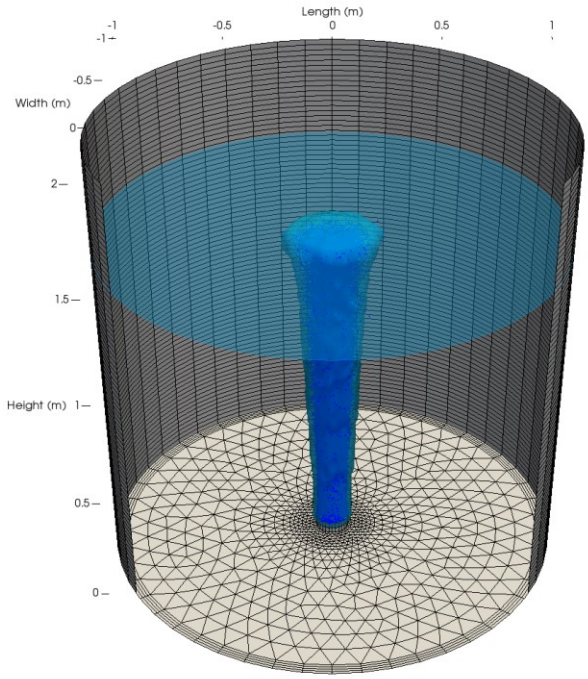

Figure 4.22: Screenshots of the three-dimensional time averaged bubble plume in the RANS cases with the lift coefficient of 0.5 and the turbulent dispersion model. The gas injection rate is 7.5 NL/min.

4.4. Conclusions

The purpose of the validation cases presented in this chapter was to test the hydrodynamics predictions of the developed LPT-VOF solver. The validation case was chosen because of the availability of a comprehensive dataset. The simulation results from Dhotre and Smith (2007) and Dhotre et al. (2009) were used to help in tuning the model parameters (closure models), and as another source of validation data with respect from an EE model. This validation case was simulated using two different turbulence models (LES – Smagorinsky (1963) SGS and RANS – k-ε), three lift coefficients (0.1, 0.288 and 0.5), and with the effects of a turbulent dispersion model (random walk). Additionally, two different meshes were used to examine mesh dependence. Three different gas flow rates were also simulated to investigate the effect of gas superficial velocity on hydrodynamics. The study was quantified based on comparison to experimental and EE simulated profiles for the gas volume fraction, axial gas and liquid velocities, and turbulent kinetic energy at three different elevations (0.35 m, 0.75 m and 1.1 m).

The solver predicted similar results for the gas volume fraction, axial gas and liquid velocities, and the turbulent kinetic energy for both the coarse and fine meshes in the LES and the RANS simulations. The fine mesh gave smoother profiles for the turbulent kinetic energy in the LES simulations. The results predicted by the two meshes with the chosen parameterization are in good agreement compared to the experimental data and the simulation from the EE simulations. Three lift coefficients were test in both the LES and the RANS simulations to investigate the effect of the lift coefficient on the plume modelling. It seems that the lift coefficient does not have significant impact on the axial gas and liquid velocities, but it has a strong effect on the gas volume fraction and the turbulent kinetic energy. Higher lift coefficients move the spreading of the plume in the radial direction, resulting in lower gas volume fraction values near the centerline. A lift coefficient of 0.5 seemed to give the best predictions among the three chosen lift coefficients. The effect of the turbulent dispersion model on the bubble plume was also tested only in the RANS simulations. The results showed that the turbulent dispersion model affects the spreading of the plume; however, it does not significantly impact the axial liquid velocity and turbulent kinetic energy predictions. The solver gives a good

agreement of the results compared to the results from the experiments and the EE simulations using both the LES and the RANS turbulence models. The effect of flow rate on the predictions was also studied using the LES model. Lower flow rates resulted in underprediction of the gas volume fraction at the centerline of the plume but gave an overprediction of the plume radius. Higher flow rates resulted in overpredictions of the results, but the results provided better fits to the experimental data and the simulation results from the EE model.

Chapter 5: Modelling Fluid Dynamics and Mass Transfer in Bubble Plumes

5.1. Introduction

Park and Yang (2017) investigated oxygenation of water in a rectangular tank. In these experiments, a rectangular tank contained water that was deoxygenated initially, and a mixture of air and water was horizontally injected into the tank. The water was continuously circulated through an external pipe and the flow rates for both air and water were varied. This validation case was chosen to test the combined hydrodynamics and mass transfer predictions for the LPT-VOF solver due to the completeness of the available dataset and because the complexity of the conditions pushes the boundaries of the solver. The objectives of this validation case were to evaluate the spreading lengths and widths of the bubble plumes, verify the LPT mass transfer model, and investigate the prediction of the bubble diameter by comparing the simulation results to the overall mass transfer coefficient values reported by Park and Yang (2017). The second validation case was the large-scale experiment of Milgram (1983). The main objective of the second validation case was to validate the fluid dynamics predictions of the solver for a large-scale bubble plume through comparison of the results with the experimental data. Simulations were performed with and without mass transfer because the experiments did not record the background dissolved oxygen concentration. Therefore, the simulations with and without mass transfer should bound the hydrodynamics solution.

5.2. Park and Yang Case

The first validation case was based on the experiments from Park and Yang (2017). The purpose of this validation case was to test both the fluid dynamics and the mass transfer predictions of the LPT-VOF solver for the case of horizontally-injected bubble plumes. The objectives of this case were to compare the spreading lengths and widths of the bubble plumes with the experimental data and to predict the bubble size based on the measured overall mass transfer coefficient.

5.2.1. Geometry and Mesh

A sketch of the geometry for the Park and Yang (2017) experiments is shown in Figure 5.1. In the experiments described by Park and Yang (2017), air and water were mixed before being horizontally injected into the water in the rectangular tank through a nozzle. The length of the tank was 1.8 m, and both the width and the height were 0.9 m. The water level was set to 0.55 m. The injection nozzle was located 0.2 m above the bottom of the tank, on one of the shorter walls. Water was recirculated back to the injection nozzle from the opposite side of the tank. A special injection nozzle was used to mix the air and water being injected into the tank. The experiments used three valves at 11 different primary nozzle distance ratios to vary the air and water flow rates. The bubble sizes were not measured. In this study, five cases were selected and simulated to make comparisons between the simulation results and the experimental data. The experiments were performed at atmospheric pressure and between 23.5 °C and 26.5 °C; therefore, an average temperature of 25 °C was used in the simulations.

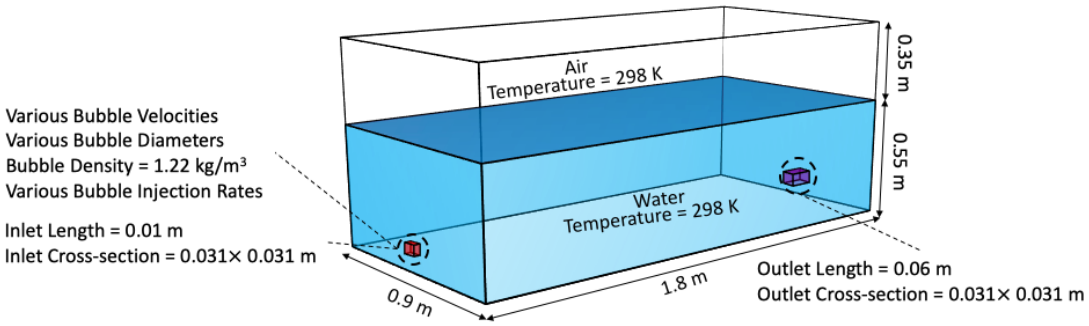

Figure 5.1: Geometry and conditions used in the Park and Yang case.

Three structured computational meshes were considered for this validation case to investigate the effect of mesh refinement. Figure 5.2, Figure 5.3 , and Figure 5.4 show the side and front views of the coarse, intermediate, and fine meshes. The numbers of the computational cells for these three meshes are 152 892, 416 781, and 1 411 036.

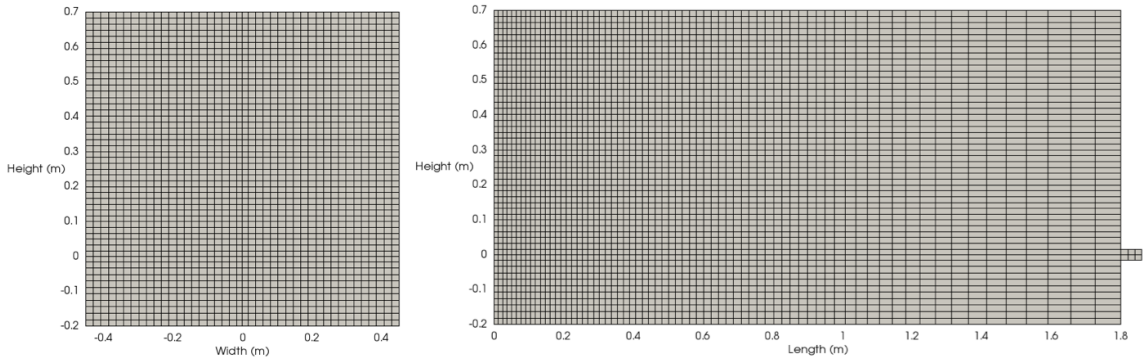

Figure 5.2: Coarse mesh used in the Park and Yang case. The mesh contains 152 892 computational cells.

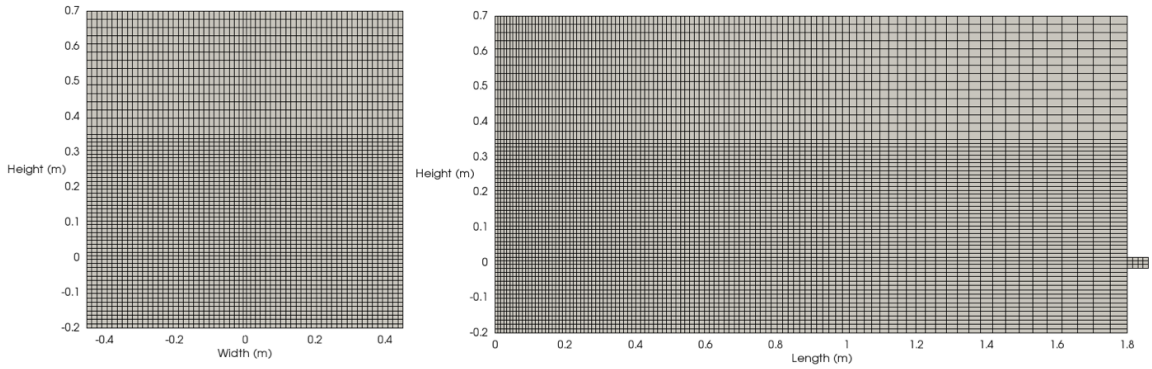

Figure 5.3: Intermediate mesh used in the Park and Yang case. The mesh contains 416 781 computational cells.

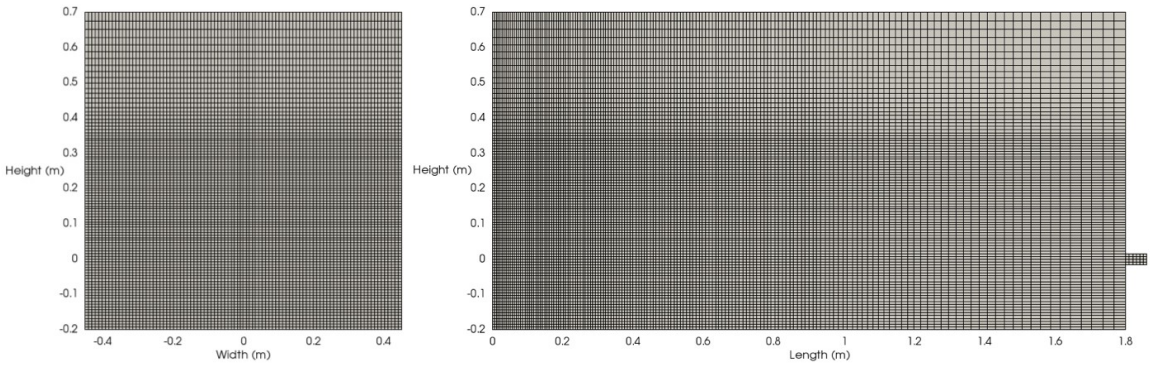

Figure 5.4: Fine mesh used in the Park and Yang case. The mesh contains 1 411 036 computational cells.

5.2.2. Case Setup

In the experiments, air and water were mixed and injected into the tank through an injection nozzle. Instead of trying to resolve the outlet of the injection nozzle in the simulations, it was assumed that the nozzle could be represented by a volumetric injection of gas and liquid into a small box adjacent to the left wall of the tank. The length of the injection box

was specified to be 0.031 m (corresponding to the average diameter in the nozzle) and the width was 0.01 m. The injection box was placed 0.2 m above the bottom of the tank from its center point to match the experimental setup. In other words, the air and water were injected into a small box having dimensions of 0.031 m × 0.031 m × 0.01 m. The injection of the water was accomplished via mass and momentum injection sources. The air was injected through 500 injection sites inside the same injection box as the water. The location of the 500 injection sites was generated randomly using a random number generator. Since the air and water were injected together, it was assumed that there was no relative velocity between the phases upon injection. This assumption was required because the experiments did not record the phase velocities at the outlet of the injection nozzle. In the experiments, an outlet on the right wall of the tank was used to recirculate water. In the simulations, a short pipe was added on the right wall of the tank to remove water at the injection rate and thereby ensure that the water level remained constant. The simulations were only performed for a short period of time. Therefore, the dissolved oxygen concentration at the outlet did not change significantly, and it was not necessary to recirculate the exiting concentration to the inlet in the simulations.

Five of the cases from Park and Yang (2017) were chosen for the simulations. The details of the injection conditions for the selected cases are summarized in Table 5.1.

Table 5.1: Summary of Conditions for the Simulated Cases from Park and Yang

Case	Inlet Gas Volume Fraction (-)	Bubble Inlet Velocity (m/s)	Water Outlet Velocity (m/s)	Water Injection Rate (kg/s)	Water Injection Momentum (kg m/s^2)
B25Q1-0.096	0.783	6.64	1.44	1.38	9.19
B25Q1-0.327	0.51	5.05	2.45	2.35	11.89
B25Q1-0.385	0.45	4.62	2.54	2.44	11.25
B25Q3-0.212	0.682	11.35	3.61	3.46	39.27
B25Q3-0.385	0.493	8.66	4.39	4.21	36.45

B25Q1 corresponds to a valve opening of one-fifth and B25Q3 corresponds to a full valve opening of the recirculation line. The numbers following the hyphen represent the primary nozzle distance ratios. B25Q3-0.385 was chosen to validate the fluid dynamics because it had relatively high flow rates and an injection gas volume fraction near 50%. All five cases

were simulated to evaluate the mass transfer coefficients. The boundary conditions, initial conditions used for the continuous phase, and water properties are summarized in Table 5.2, Table 5.3, and Table 5.4.

Table 5.2: Boundary Conditions Used for the Park and Yang Cases

Variable	Walls and Bottom	Outlet	Top
Liquid volume fraction, α_1 (-)	Zero gradient	Zero gradient	Zero gradient
Temperature, T (K)	Zero gradient	Zero gradient	Zero gradient (outflow) $T = 298$ K (inflow)
Velocity, $\vec{u}$ (m/s)	No slip	See Table 5.1	Zero gradient (outflow) $\vec{u} = 0$ m/s (inflow)
Modified pressure, P_{rgh} (Pa)	Fixed flux pressure	Fixed flux pressure	101325
O_2 mass fraction, Y_{1,O_2} (-)	Zero gradient	Zero gradient	Zero gradient (outflow) $Y_{1,O_2} = 0$ (inflow)
N_2 mass fraction, Y_{1,N_2} (-)	Zero gradient	Zero gradient	Zero gradient (outflow) $Y_{1,N_2} = 0$ (inflow)
Lagrangian bubbles	Rebound	See Table 5.1	Escape*

*Although this was specified, bubbles are removed at the free surface.

Table 5.3: Initial Conditions Used for the Continuous Phase in the Park and Yang Cases

Variable	Initial Condition
Liquid volume fraction, α_1 (-)	$\alpha_1 = 1$ (below the free surface) $\alpha_1 = 0$ (above the free surface)
Temperature, T (K)	298
Velocity, $\vec{u}$ (m/s)	Volumetric Injection Source (See Table 5.1)
Modified pressure, P_{rgh} (Pa)	101 325
Turbulent kinematic viscosity, ν_t (m^2/s)	1.0×10^{-11}
O_2 (liquid) mass fraction, Y_{1,O_2} (-)	0
N_2 (liquid) mass fraction, Y_{1,N_2} (-)	0

Table 5.4: Liquid Water Properties Used for the Park and Yang Cases (Welty et al., 2008)

Property	Value
Density, ρ (kg/m^3)	996.7
Specific heat capacity, c_p (J kg^{-1} K^{-1})	4 180
Dynamic viscosity, μ (Pa s)	1.0×10^{-3} *
Prandtl number, Pr (-)	6.30

*The value of the dynamic viscosity at 293 K was mistakenly used in these simulations. The value at 298 K should be 9.093×10^{-4} Pa s. Although the value of the dynamic viscosity was not accurate, the trends displayed in the results are not expected to change significantly.

The pressure field was initialized based on the hydrostatic pressure gradient. This validation case was divided into two sections to investigate the effects of mesh refinement and bubble size on both the fluid dynamics and mass transfer in the bubble plume. A bubble size sensitivity study was performed because the bubble size was not measured in the experiments and the initial bubble diameter is unknown.

5.2.3. Mesh Study Conditions

The mesh dependence tests were performed on the B25Q3-0.385 case since it has high injection flow rates and the injected air volume fraction is about 0.5. Since the bubble size was not measured in the experiments and no information was given for the initial bubble diameter, the initial injected bubble size was assumed to be 2 mm for the B25Q3-0.385 case. In the simulations, the size of the bubbles can change based on the ideal gas law due to the pressure differences at the different depths. However, since the water level in the tank was only 0.55 m, this effect is minimal. Finally, bubbles were removed when they reached the free surface.

The bubble injection rate can be calculated based on the air volumetric flow rate and the bubble volume. Since the bubble injection rate was very high in this validation case, it was necessary to group several bubbles into parcels to resolve their motion. The grouping of bubbles into parcels can affect the simulation results if too many bubbles are grouped together into parcels. However, initial tests showed that grouping ten bubbles together into parcels did not have a significant effect on the predictions. Therefore, parcels containing groups of ten bubbles were simulated in this case. The initial injection bubble density can

be calculated using the ideal gas law at the corresponding pressure. Table 5.5 summarizes the air bubble properties used for the Lagrangian phase for the B25Q3-0.385 case. The bubble properties were similar for the other cases except for the bubble velocity and bubble parcel injection rate, which are provided in Table 5.1. The bubble diameter at the inlet was set to 2 mm for the hydrodynamics study for the B25Q3-0.385 case.

Table 5.5: Air Bubble Properties Used for the Park and Yang B25Q3-0.385 Case

Property	Parameter
Gas density at the inlet, $\rho_{b,inlet}$ (kg/m^3)	1.224
Bubble diameter at the inlet, d_b (mm)	2
Bubble velocity at the inlet, $\vec{u}_b$ (m/s)	8.66
Bubbles per parcel (-)	10
Bubble parcel injection rate (parcels/s)	196
Temperature, T (K)	298
O_2 (gas) mass fraction, Y_{O_2} (-)	0.233
N_2 (gas) mass fraction, Y_{N_2} (-)	0.767

5.2.4. Mass Transfer Study Conditions

Park and Yang (2017) state that the water in the tank was deoxygenated before beginning the experiments. However, the dissolved nitrogen levels were not recorded. The water was therefore assumed to be saturated with nitrogen at atmospheric conditions and only the oxygen dissolution rate was considered. To determine the mass transfer rate for oxygen, the molecular diffusion coefficient and concentration of dissolved oxygen in equilibrium with the gas phase must be specified. The diffusion coefficient for oxygen in water was specified to be 2.40×10^{-9} (Yaws, 2003). The dimensionless Henry's law constant for oxygen was set to be 0.02973 to calculate the concentration of dissolved oxygen in equilibrium with the gas phase (Sander, 2015).

The overall mass transfer coefficient ($k_l a$) can be obtained using the following equation, which is the same equation used in Park and Yang (2017).

$$k_l a = \frac{\ln\left(\frac{C_{sat}-C_0}{C_{sat}-C}\right)}{t} \tag{5.1}$$

where C_{sat}, C_0, and C are the concentrations of dissolved oxygen at the saturation condition, the initial concentration of oxygen, and the oxygen concentration at time t,

respectively. The saturation concentration for dissolved oxygen was approximately 8.48 mg/L. The initial concentration of oxygen was set to zero. The overall mass transfer coefficients reported in the paper for all the five selected cases are summarized in Table 5.6.

Table 5.6: Approximate $k_l a$ Values for the Selected Park and Yang (2017) Cases

Case	$k_l a$ (s^{-1})
B25Q1-0.096	2.50×10^{-3}
B25Q1-0.327	1.85×10^{-3}
B25Q1-0.385	1.00×10^{-3}
B25Q3-0.212	4.25×10^{-3}
B25Q3-0.385	2.00×10^{-3}

Since the bubble sizes were not measured in the experiments, a bubble size sensitivity study was performed to investigate the effect of bubble size on the mass transfer coefficient. In reality, the bubbles should have a size distribution; however, it is difficult to predict the real bubble size distribution. Therefore, the bubble size distribution was not considered in this study and a fixed initial bubble size was assumed. Three different bubble sizes were tested for all five cases and the corresponding bubble parcel injection rates are summarized in Table 5.7. Each parcel contained ten bubbles, as mentioned earlier.

Table 5.7: Summary of the Bubble Size Studies for the Five Cases Selected from Park and Yang

Case	Bubble Diameter (m)	Bubble Parcel Injection Rate (parcels/s)
B25Q1-0.096	0.001	1910
	0.0015	566
	0.002	239
B25Q1-0.327	0.001	955
	0.0015	283
	0.002	119
B25Q1-0.385	0.001	764
	0.0015	226
	0.002	95
B25Q3-0.212	0.001	2844
	0.0015	843
	0.002	355
B25Q3-0.385	0.001	1570
	0.0015	465
	0.002	196

5.2.5. Closure Models

The force closure models used for the simulations were gravity, buoyancy, the Tomiyama (1998) contaminated drag model, the Tomiyama (2002) lift model, and a constant coefficient of 0.5 for the virtual mass force. Simulations were performed using LES with the Smagorinsky (1963) SGS model. The Smagorinsky coefficient, C_s, was assumed to have a value of 0.12, and bubble-induced turbulence was included through the model of Sato et al. (1975). Since LES was used for turbulence modelling, the turbulent dispersion force was not considered in this case. The Hughmark (1967) mass transfer model for contaminated systems was used to evaluate the gas dissolution rate in the bubble plume.

5.2.6. Results and Discussion

5.2.6.1. Mesh Refinement

Fluid dynamics and the mass transfer were simulated to test sensitivity of the predictions to mesh refinement. The mesh refinement tests were performed on the B25Q3-0.385 case and an initial bubble size was assumed to be 2 mm. Figure 5.5 shows the time-averaged (between 3 and 10 s) plume shape of the B25Q3-0.385 case with the intermediate mesh.

The blue plane above the plume represents the free surface. The 1% gas volume fraction contour is coloured as light blue, while the bubbles are shown as dark blue.

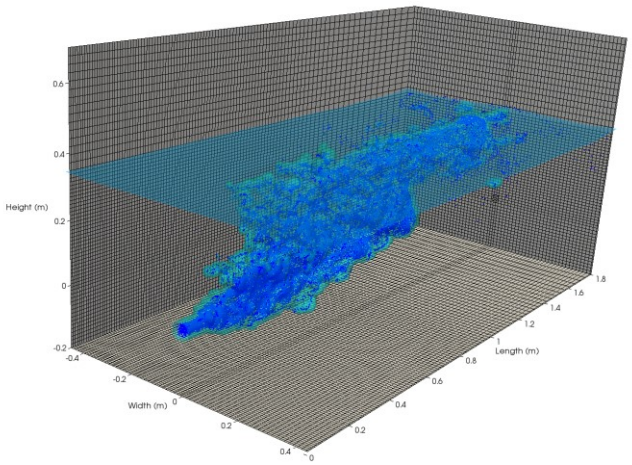

Figure 5.5: Three-dimensional time-averaged (from 3 s to 10 s) bubble plumes for the B25Q3-0.385 case with the intermediate mesh.

Figure 5.6 shows the comparisons between the predicted gas volume fraction contours for the three meshes and the experimental contour. The predicted contours are plotted using three contour levels: 0.01, 0.05, and 0.1. The experimental contour data was obtained from the photos in Park and Yang (2017). However, it is difficult to acquire the precise contour information from the photos due to their resolution. Therefore, only the main contours of the plumes are shown, and the trajectories of the plume actually reach the free surface. From Park and Yang (2017), the penetration length of the plume for this case is 1.02 m. The predicted trajectories have good agreement with the experimental data for all the three meshes. However, the coarse mesh overpredicts the transition of the plume, while the intermediate and the fine meshes give better predictions for the trajectories and transitions. The predictions from the intermediate and fine meshes are similar, but the fine mesh predictions produce more spreading of the plume.

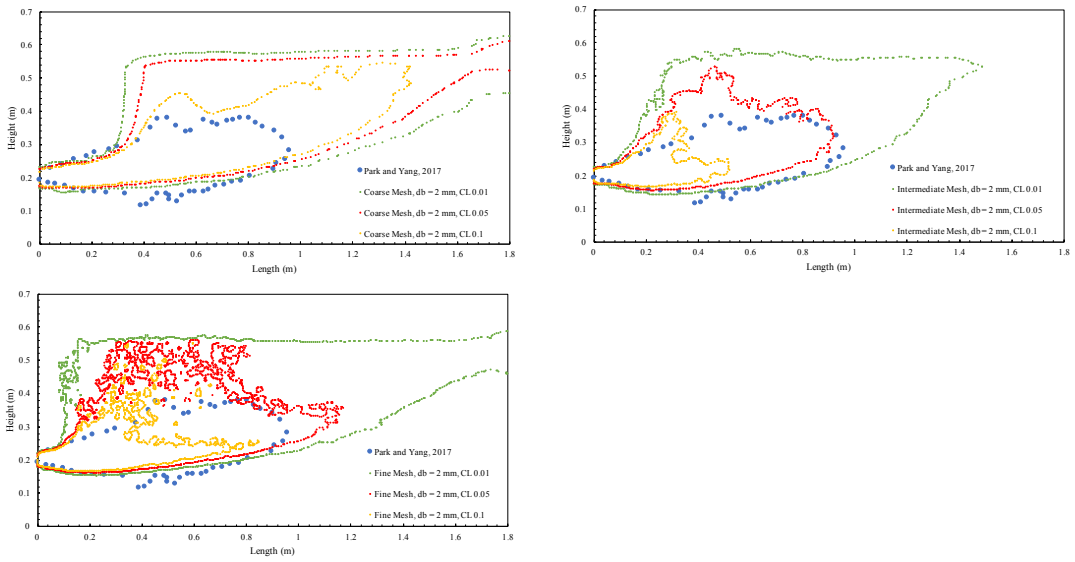

Figure 5.6: Comparisons between the experimental and estimated gas phase fraction contours for the B25Q3-0.385 case on the coarse mesh (top left), intermediate mesh (top right), and fine mesh (bottom) with three contour levels (*CL* = 0.01, 0.05, and 0.1).

The spreading width of the plumes was not reported in Park and Yang (2017). However, they can be estimated based on the following equation for the average spreading angle of the jet (Ma et al., 2018):

$$\tan\theta = 100.58 \cdot Fr'^{0.21} \cdot \left(\sqrt{\frac{\rho_g}{\rho_l}} \cdot Re\right)^{-0.78} \tag{5.2}$$

where θ, Fr', ρ_g, ρ_l, and Re are the spreading angle of the jet, the modified Froude number, gas density, liquid density, and the Reynolds number of the liquid, respectively. Once the average spreading angle is known, the spreading width can be calculated based on the spreading angle and the spreading length of a stable plume.

The spreading length of the stable plume in this case is 1.4 m, as described in Park and Yang (2017), and the corresponding spreading width was calculated to be 0.09 m using Eq. 5.2. The predicted spreading widths for the coarse, intermediate, and fine meshes were 0.12 m, 0.31 m, and 0.29 m. The predicted spreading widths were obtained by taking gas volume fraction contours of 1% on vertical planes at the spreading length of 1.4 m. These results seem to indicate that the spreading width prediction is more mesh dependent than the jet length prediction.

The cases were run to ten seconds to evaluate the mass transfer coefficient to obtain stable results through longer simulation time. Figure 5.7 shows the data used to determine the overall mass transfer coefficients obtained from the three different meshes. The $k_l a$ for each case is equal to the slope of the line in Figure 5.7. The $k_l a$ value reported in Park and Yang (2017) for this case was 2.00×10^{-3} s^{-1}. Unfortunately, the predicted mass transfer coefficient increased by approximately 12% for each mesh refinement. Therefore, it is not possible to estimate how much more mesh resolution would be required to obtain a mesh independent result. The lack of mesh convergence for the mass transfer coefficient seems to agree with the result for the spreading width. One of the reasons for the lack of mesh independence might be the assumption of constant bubble size. Upon injection, the bubble size is likely to be quite large, before the gas jet has time to break up. However, another reason could be the way in which gas and liquid were injected into the domain in the simulations. Further studies would be necessary with a bubble size distribution and/or a population balance model to test the coupled effects of bubble size distribution and mesh refinement. Further studies would also be necessary to test the effect of injection configuration on the results.

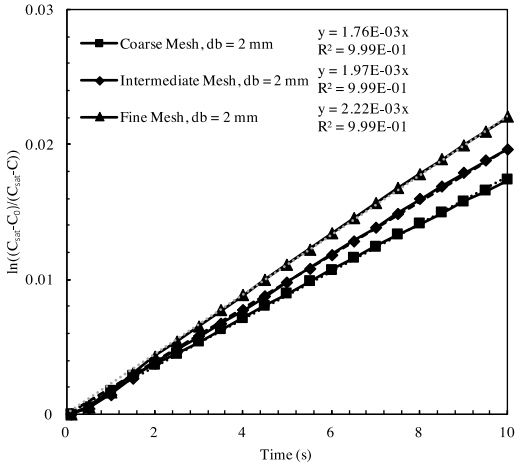

Figure 5.7: Overall mass transfer coefficient prediction for the coarse, intermediate, and fine meshes for the B25Q3-0.385 case using the Hughmark (1967) model.

As mentioned earlier, the coarse mesh did not predict the fluid dynamics of the plume as well as the intermediate and the fines meshes. However, there also seemed to be a lack of convergence on a mesh independent solution between the intermediate and fine meshes.

Unfortunately, it was not possible to test further mesh refinements due to computational resource limitations. Despite the lack of convergence on a mesh independent result, the intermediate mesh was used to simulate further cases to assess the impact of the assumed bubble size on fluid dynamics and mass transfer predictions.

5.2.6.2. Bubble Size Sensitivity Study

Three different initial bubble sizes were used to evaluate the effect of the bubble size on the mass transfer coefficient for all five selected cases. B25Q3-0.385 was the main case for this case study because it was also used for the mesh refinement study. Therefore, the bubble size study was first performed on this case.

The experimental and predicted gas volume fraction contours with the bubble sizes of 1 mm and 1.5 mm for the B25Q3-0.385 case are presented with three contour levels in Figure 5.8. These results can be compared to the result for the bubble size of 2 mm, which is displayed in the top right graph in Figure 5.6. Again, the theoretical spreading width for this case is 0.09 m. The predicted spreading widths for the bubble size of 1 mm, 1.5 mm, and 2 mm were 0.27 m, 0.20 m, and 0.14 m. The bubble size of 2 mm gave the closest estimation for the trajectory transition and the spreading width of the plume among the three bubble sizes, which suggests that 2 mm is the best approximation of the bubble size for this case hydrodynamically. However, it is important to remember that the solution was not mesh independent. Therefore, only the trends in the predictions are meaningful because a more refined mesh would have resulted in a different prediction for the value of the most suitable diameter.

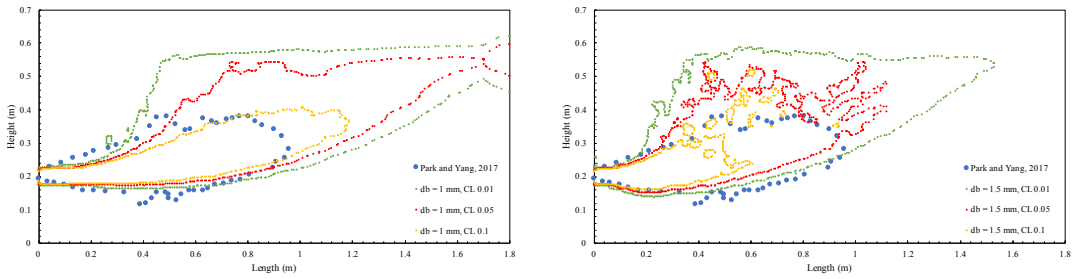

Figure 5.8: Comparisons between the experimental and estimated gas phase fraction contours for the B25Q3-0.385 case with initial bubble sizes of 1 mm and 1.5 mm and three contour levels.

Figure 5.9 shows the predicted $k_l a$ values for the three different bubble sizes in the B25Q3-0.385 case. Among the three bubble sizes, the bubble size of 2 mm has the closest $k_l a$ value when compared to the experimental data. The smaller bubble sizes overpredicted the $k_l a$. This is expected because the plume spreading seems to have been overpredicted for lower diameters. An overprediction of the plume width would lead to an overestimate of the bubble residence time and thereby increase the effective overall mass transfer coefficient. From the results, it appears that the average bubble size should be near 2 mm. However, it is important to remember that this result is not mesh independent and that the predictions depend on the assumed mass transfer closure model. Further, a uniform bubble size was assumed, so the results would also change if a bubble size distribution were used. It would be possible to obtain a more definitive estimate of the bubble size if the experimental plume width and local bubble velocity measurements were available.

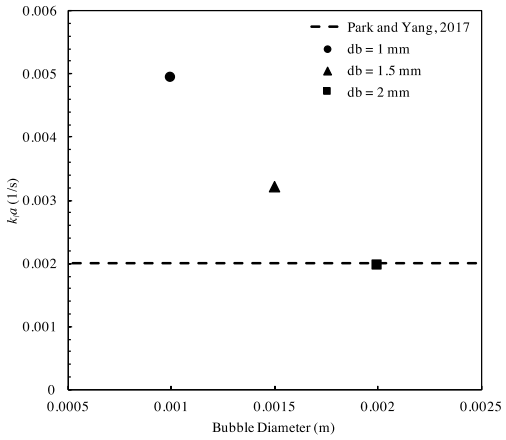

Figure 5.9: Overall mass transfer coefficient comparisons of three different bubble sizes for the B25Q3-0.385 case.

Figure 5.10 and Figure 5.11 show the comparison between the experimental and estimated gas volume fraction contours with bubble sizes of 1 mm, 1.5 mm, and 2 mm and three contour levels for the B25Q1-0.096, B25Q1-0.327, B25Q1-0.385, and B25Q3-0.212 cases. The comparisons between the theoretical and predicted spreading widths with three different bubble sizes for the four cases are shown in Table 5.8. It seems that, when considering the hydrodynamics, the ranges of bubble sizes that give the best predictions for the B25Q1-0.096, B25Q1-0.327, B25Q1-0.385, and B25Q3-0.212 cases are 1 to 1.5 mm, 1 mm, 1.5 to 2 mm, and 1.5 to 2 mm, respectively. However, similar to the B25Q3-

0.385 case, it is not possible to definitively select an optimal bubble size because of the mesh dependency.

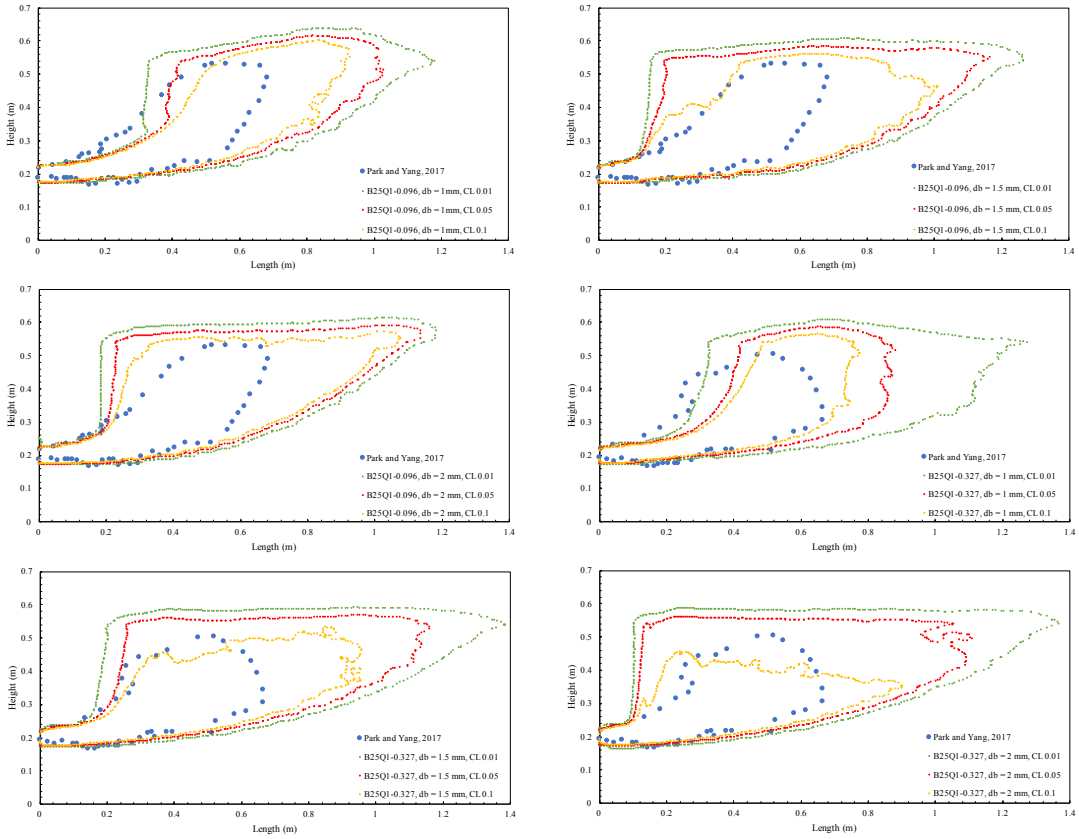

Figure 5.10: Comparisons between the experimental and estimated gas phase fraction contours for the B25Q1-0.096 and B25Q1-0.327 cases with initial bubble sizes of 1 mm, 1.5 mm and 2 mm and three contour levels.

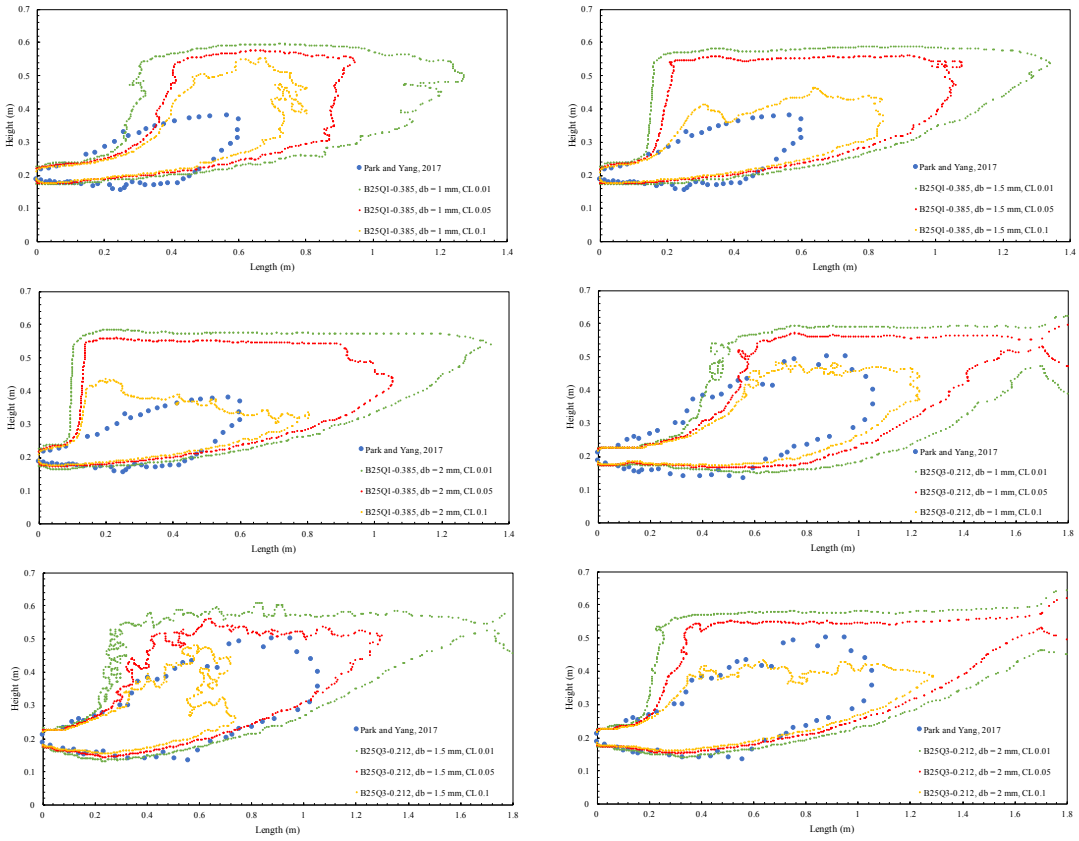

Figure 5.11: Comparisons between the experimental and estimated gas phase fraction contours for the B25Q1-0.385 and B25Q3-0.212 cases with initial bubble sizes of 1 mm, 1.5 mm and 2 mm and three contour levels.

Table 5.8: Summary of the Spreading Widths for B25Q1-0.096, B25Q1-0.327, B25Q1-0.385, and B25Q3-0.212 Cases with Three Different Bubble Sizes

Case	Penetration Length (m)	Spreading Length (m)	Theoretical Spreading Width (m)	Bubble Diameter (m)	Predicted Spreading Width (m)
B25Q1-0.096	0.58	1.24	0.12	0.001 0.0015 0.002	0.26 0.23 0.11
B25Q1-0.327	0.56	1.08	0.08	0.001 0.0015 0.002	0.31 0.22 0.18
B25Q1-0.385	0.63	1.00	0.07	0.001 0.0015 0.002	0.26 0.19 0.16
B25Q3-0.212	0.81	1.44	0.11	0.001 0.0015 0.002	0.37 0.25 0.24

Figure 5.12 shows the comparison between the experimental and predicted overall mass transfer coefficients with three bubble sizes for the B25Q1-0.096, B25Q1-0.327, B25Q1-0.385, and B25Q3-0.212 cases. From the mass transfer coefficient data, it appears that the actual bubble size should be approximately 1 mm to match the experimental value for the B25Q1-0.327 case. For the B25Q1-0.096 case, the bubble size of 1 mm overpredicted the mass transfer coefficient, while bubble sizes of 1.5 mm and 2 mm underpredicted the mass transfer coefficient. This means that a bubble size between 1 mm and 1.5 mm is needed to match the experimental value. Similarly, for the B25Q1-0.385 and the B25Q3-0.212 cases, bubble sizes of 1 mm and 1.5 mm overpredicted the $k_l a$ values, while 2 mm bubbles underpredicted the $k_l a$ values. Therefore, a bubble size between 1.5 mm and 2 mm is needed to match the experimental value. Again, the estimated bubble sizes that provide the most reasonable mass transfer coefficient predictions also provide plume width predictions that are most similar to the theoretical values. Although this confirms that the model provides consistent predictions between fluid dynamics and mass transfer, the values cannot be treated as absolute estimates due to mesh dependence of the results and the assumption of a uniform bubble size distribution.

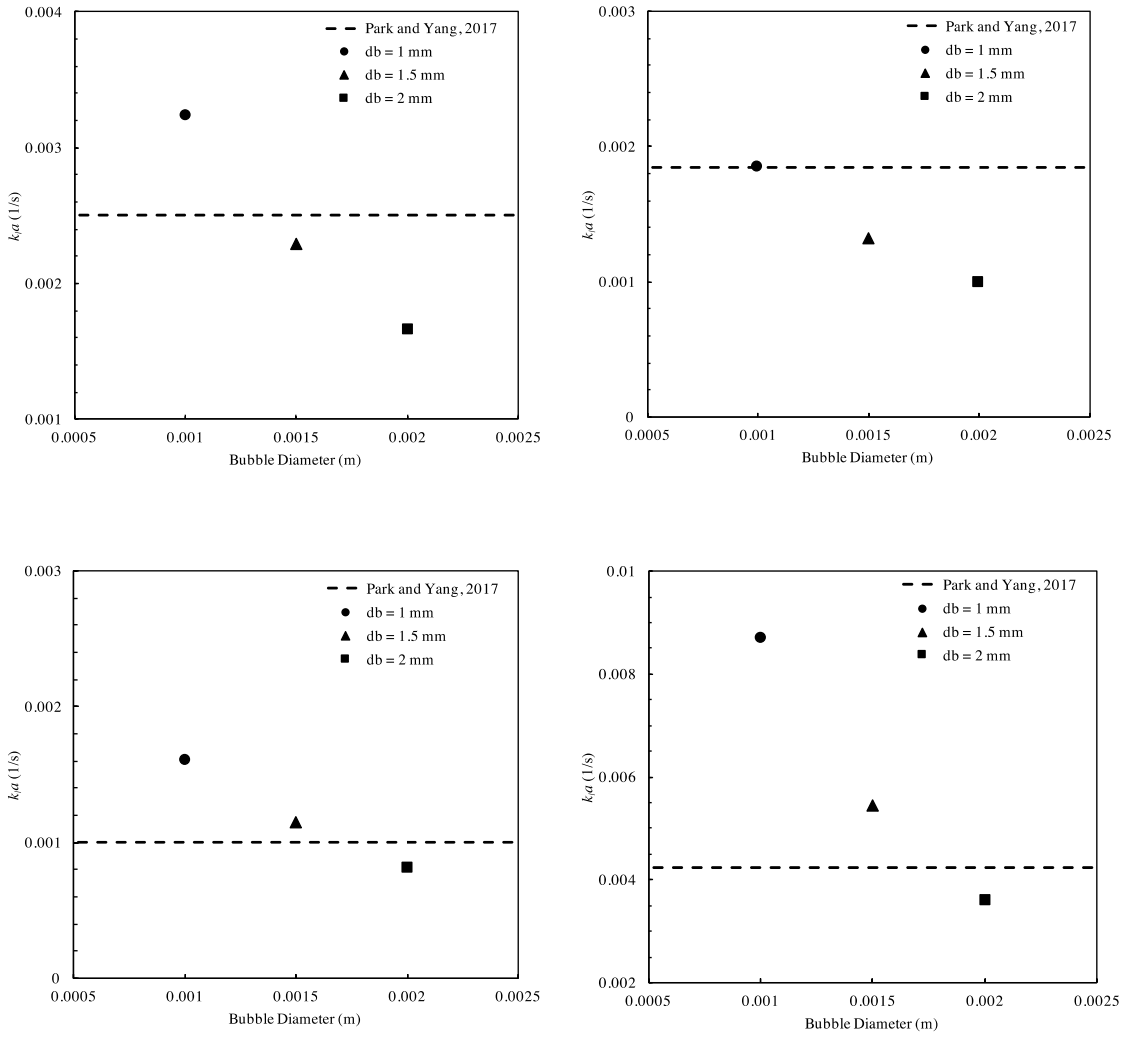

Figure 5.12: Overall mass transfer coefficient comparisons of three different bubble sizes for the B25Q1-0.096 case (top left), B25Q1-0.327 case (top right), B25Q1-0.385 case (bottom left), and B25Q3-0.212 case (bottom right).

5.3. Milgram Case

A large-scale plume was simulated based on the experiments conducted by Milgram (1983). The purpose of this validation case was to evaluate the performance of the LPT-VOF solver when used to predict fluid dynamics and gas dissolution in a large-scale vertically-injected bubble plume. The objectives of this case were to compare the gas volume fraction, velocity, and radius of the bubble plume with the experimental data and to validate the solver at a larger scale. The case was simulated with and without mass

transfer because the experimental study did not record the background dissolved oxygen concentration. Therefore, the simulations with and without mass transfer should bound the hydrodynamic results.

5.3.1. Case Studies

Milgram (1983) performed large-scale experiments of a vertically-injected bubble plume with various air injection rates up to 0.59 Nm^3/s in Bugg Spring, Florida. The water temperature in the lake is reported to be approximately 22 °C year-round (Underwater Sound Reference Division (USRD), n.d.). The diameter of the spring is approximately 35 m. The pipe used for the air injection had an inside diameter of 5 cm and a height of 2.5 m. The water level was 50 m above the end of the injection pipe. A sketch of the geometry is shown in Figure 5.13. The geometry was approximated using a square cross-section because the effects of the boundaries is expected to be minimal due to the size of the system.

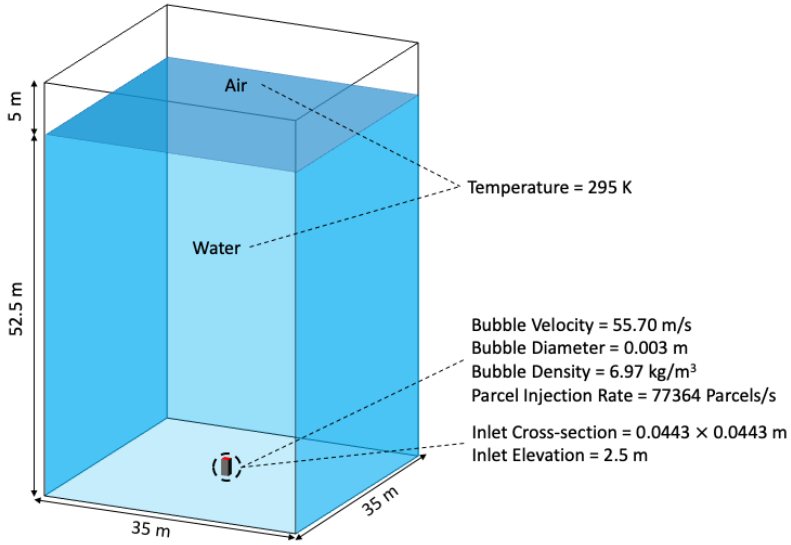

Figure 5.13: Geometry and conditions used in the Milgram case.

To simplify meshing for the structured mesh, the inlet pipe was converted to a square with the same cross-sectional area as the pipe. The inlet patch was therefore specified as a square with a side length of 0.0443 m. The inlet patch was elevated to 2.5 m above the center of the bottom of the geometry to match the height of the injection pipe in the experiments. The case settings were similar to those used in the LES cases in Chapter 4, but a different

flow rate and a slightly different temperature were used. Table 5.9 and Table 5.10 summarize the boundary conditions and the initial conditions used in this case. The liquid properties are listed in Table 5.11.

Table 5.9: Boundary Conditions Used in the Milgram Case

Variable	Inlet Patch	Walls and Bottom	Top
Liquid volume fraction, α_1 (-)	Zero gradient	Zero gradient	Zero gradient
Temperature, T (K)	Zero gradient	Zero gradient	Zero gradient (outflow) $T = 295$ K (inflow)
Velocity, $\vec{u}$ (m/s)	Slip	No slip	Zero gradient (outflow) $\vec{u} = 0$ m/s (inflow)
Modified pressure, P_{rgh} (Pa)	Zero gradient	Zero gradient	101325
O_2 mass fraction, Y_{1,O_2} (-)	Zero gradient	Zero gradient	Zero gradient (outflow) $Y_{1,O_2} = 0$ (inflow)
N_2 mass fraction, Y_{1,N_2} (-)	Zero gradient	Zero gradient	Zero gradient (outflow) $Y_{1,N_2} = 0$ (inflow)
Lagrangian bubbles	Injection	Rebound	Escape*

*Although this was specified, bubbles are removed at the free surface.

Table 5.10: Initial Conditions Used in the Milgram Case

Variable	Initial Condition
Liquid volume fraction, α_1 (-)	$\alpha_1 = 1$ (below the free surface) $\alpha_1 = 0$ (above the free surface)
Temperature, T (K)	295
Velocity, $\vec{u}$ (m/s)	0
Modified pressure, P_{rgh} (Pa)	101 325
Turbulent kinematic viscosity, ν_t (m^2/s)	1.0×10^{-11}
O_2 (liquid) mass fraction, Y_{1,O_2} (-)	0
N_2 (liquid) mass fraction, Y_{1,N_2} (-)	0

Table 5.11: Liquid Water Properties Used in the Milgram Case (Welty et al., 2008)

Property	Value
Density, ρ (kg/m^3)	997.6
Specific heat capacity, c_p (J kg^{-1} K^{-1})	4 181
Dynamic viscosity, μ (Pa s)	9.6×10^{-4}
Prandtl number, Pr (-)	6.62

The highest gas flow rate of 0.59 normal m^3/s in the experiments of Milgram (1983) was used. The actual injection flow rate at 295 K and atmospheric pressure was converted to be 0.11 m^3/s based on the gas density ratio at the standard conditions and the inlet. The gas density at the inlet can be calculated using the ideal gas law at the corresponding pressure and temperature and the value was 6.97 kg/m^3. The corresponding injection velocity and bubble injection rate at the inlet were calculated to be 55.70 m/s and 77 364 parcels/s (100 bubbles per parcel), respectively.

The pressure field was initialized based on the hydrostatic pressure gradient. The initial bubble size was set to be 3 mm, as described in Milgram (1983). However, the size of the bubbles changes with elevation in the water column according to the ideal gas law. Therefore, the bubble size leaving the free surface is approximately 5 mm. The bubbles were removed when they reach the free surface. Table 5.12 summarizes the air bubble properties used for the Lagrangian phase.

Table 5.12: Air Bubble Properties Used in the Milgram Case

Property	Parameter
Gas density at the inlet, $\rho_{b,inlet}$ (kg/m^3)	6.97
Bubble diameter at the inlet, d_b (mm)	3
Bubble velocity at the inlet, $\vec{u}_b$ (m/s)	55.70
Bubbles per parcel (-)	100
Bubble parcel injection rate (parcels/s)	77 364
Temperature, T (K)	295
O_2 (Gas) mass fraction, Y_{O_2} (-)	0.233
N_2 (Gas) mass fraction, Y_{N_2} (-)	0.767

As in the Park and Yang (2017) case, the Smagorinsky (1963) SGS model with a coefficient, C_s, of 0.12 was used with the bubble-induced turbulence model of Sato et al.

(1975). The turbulent dispersion force was not considered in this case. The Hughmark (1967) mass transfer model for contaminated system was used to evaluate the gas dissolution in the bubble plume. The dimensionless Henry's law constants for the oxygen and the nitrogen at 295 K were set to be 0.02943 and 0.01570, respectively (Sander, 2015). Gravity and buoyancy were included in the force balance. The lift coefficient and the virtual mass coefficient were set to 0.5. Based on Olsen and Skjetne (2016), who also simulated the Milgram case using an LPT-VOF approach in ANSYS Fluent, the Tomiyama (1998) model with the swarm correction of Tsuji et al. (1982) was used as the drag model in this validation case.

The mesh that used in this validation case is shown in Figure 5.14. This case only tested on one mesh to save the computational time as it is a large-scale case. The number of the computational cells in the mesh is 623 295.

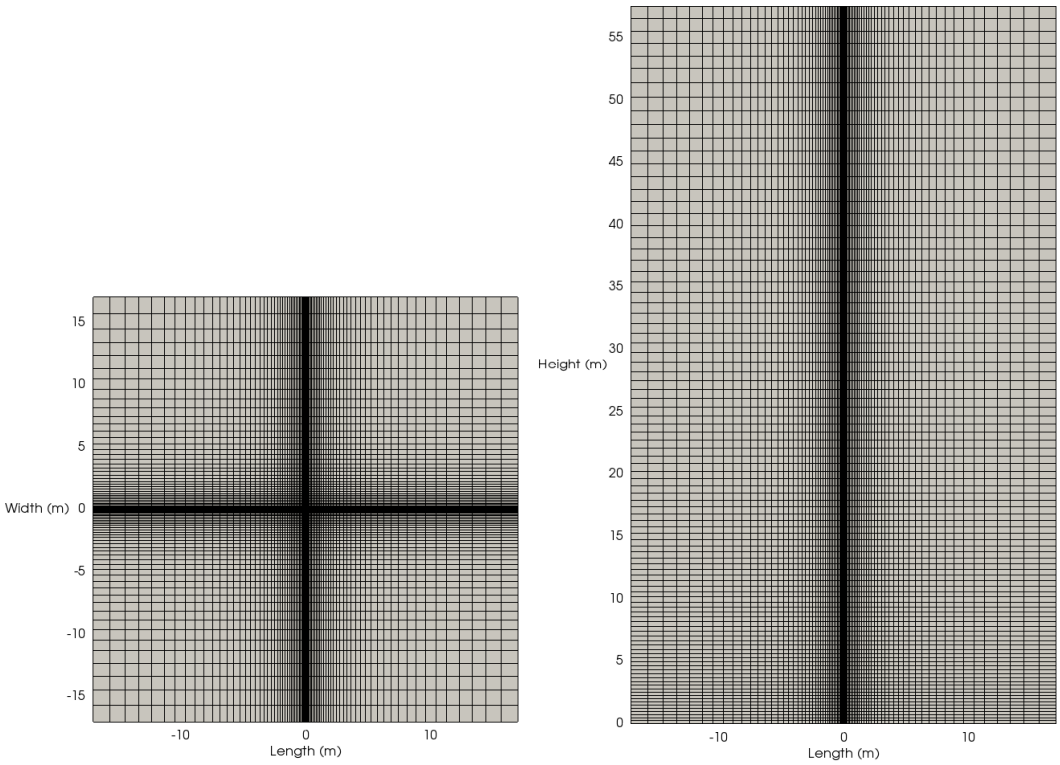

Figure 5.14: Mesh used in the Milgram case. The mesh contains 623 295 computational cells.

5.3.2. Results and Discussion

Figure 5.15 shows a screenshot of the time-averaged plume for this case. The range of time averaging was 100 second after steady state. The blue plane above the plume represents the free surface. The contour of 0.01% gas volume fraction is colored light blue and the bubbles are shown as the dark blue.

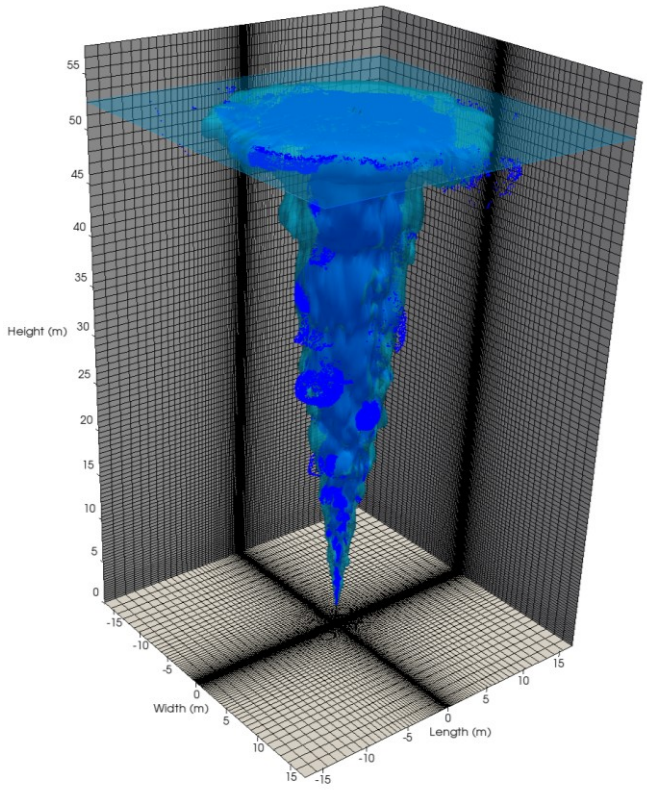

Figure 5.15: Screenshot of the three-dimensional time-averaged results for the bubble plume in the Milgram case.

Comparisons between the experimental and predicted gas volume fraction, plume velocity, and plume radius are shown in Figure 5.16. The gas volume fraction and plume velocity were obtained at the centerline of the bubble plume. The plume radius was estimated by averaging the radius of the plume at ten horizontal planes between the injector and the free surface. The solver gives relatively good predictions of the hydrodynamics and plume shape for the large-scale case with the chosen parameterization. The hydrodynamics predictions with the mass transfer model on and off are similar. The case with gas dissolution seems to give a slightly closer match to the experimental data than the case without gas dissolution. The amount of dissolution is low compared to the injection rate.

Up to 200 seconds, there were 46 811 parcels dissolved while the total number of the injected parcels was 15 472 766. In other words, only 0.30% of injected parcels dissolved completely in the water. However, there were some existing parcels that reduced their sizes due to the mass transfer as well. The mass transfer for those parcels can be estimated by the difference between the changes of the bubble flow rates of the mass transfer case and the no mass transfer case. For the case that did not include the mass transfer, the ratio of the bubble flow rate close to the free surface and the bubble flow rate near the injection point was 20.21%. The same ratio for the mass transfer case was 17.63% and the difference of those two ratios was 2.58%. In other words, the bubble flow rate near the free surface decreased by 2.58% due to the gas dissolution. Overall, 2.88% of the injected gas dissolved due to the mass transfer.

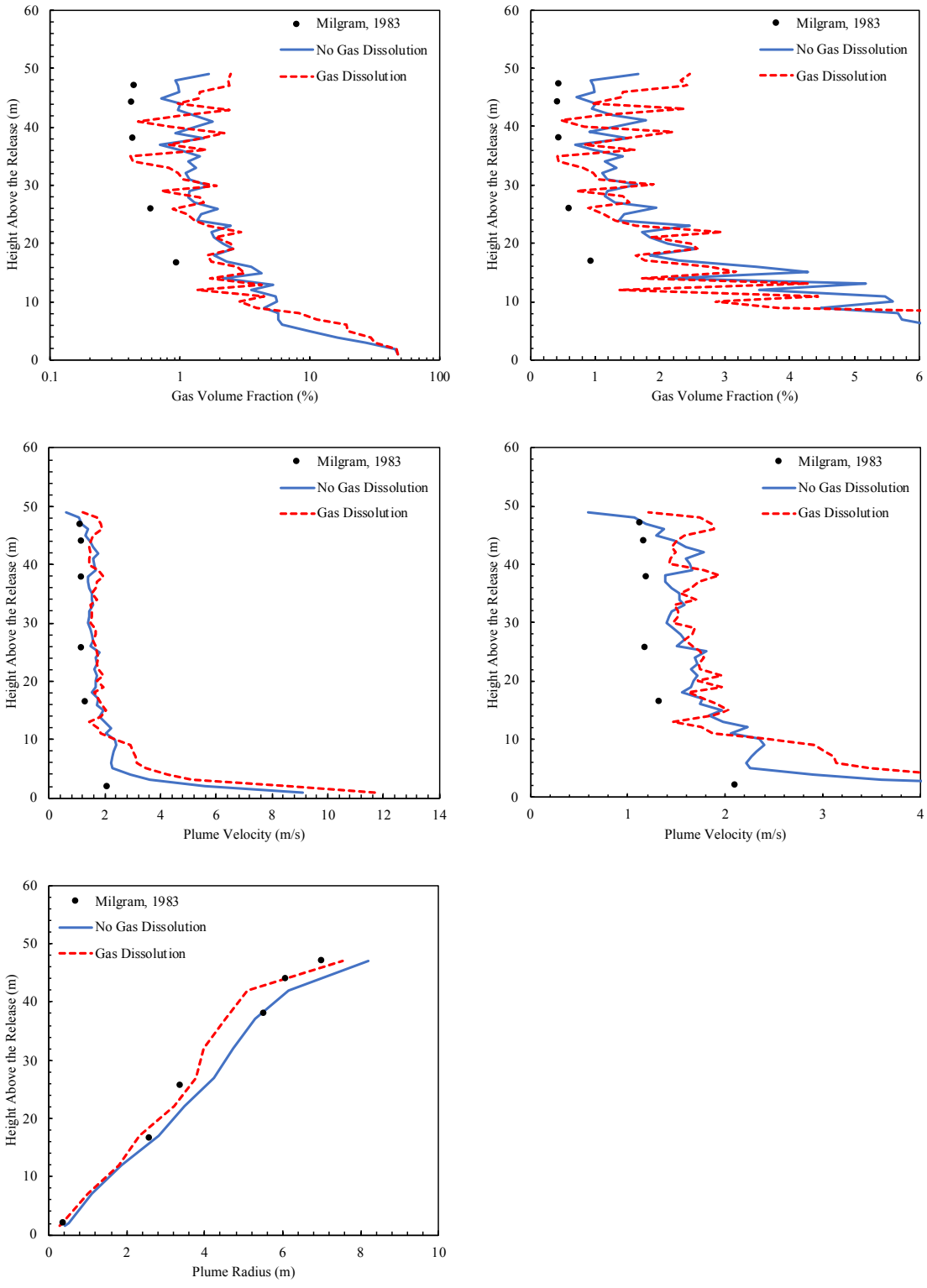

Figure 5.16: Comparisons between the centerline experimental and estimated gas volume fraction (top), plume velocity (middle row), and plume radius (bottom) of the Milgram case without and with the gas dissolution model.

5.4. Conclusions

Both fluid dynamics and mass transfer performance in horizontally-injected bubble plumes were investigated using the LPT-VOF solver by comparing to the experimental data from Park and Yang (2017). The liquid water and the air bubbles were mixed and injected together through an injection box on the left wall of the tank, which is 0.2 m above the bottom of the tank. Gravity, buoyancy, drag, lift, and virtual mass forces were included. An LES approach with the Smagorinsky SGS model and a coefficient of 0.12 was used as the turbulence model. A bubble-induced turbulence model was also included (Sato et al., 1981). The mesh refinement was tested on three different meshes on one of the five selected cases. The intermediate and fine meshes gave better prediction of the spreading length and width compared to the coarse mesh. However, the predicted plume width and mass transfer coefficient showed that a mesh independent solution was not obtained. Nonetheless, the intermediate mesh was selected to perform further simulations to study the impact of bubble size on plume spreading behaviour and mass transfer rate. The sensitivity study for the bubble size showed reasonable trends for the selected cases, but an actual average bubble size could not be estimated due to the lack of a mesh dependent solution and model simplifications.

A large-scale bubble plume was simulated to investigate the performance of the solver on the large-scale system. The predicted gas volume fraction, plume velocity, and plume radius for the simulations with and without mass transfer provided predictions close to the experimental results from Milgram (1983). Only 2.88% parcels of the injected gas dissolved in the water when the simulation used a negligible background dissolved oxygen concentration. Therefore, the effect of mass transfer on the hydrodynamic simulation and experimental results is small.

For the future work, the effect of bubble size distribution should be further investigated for both the Park and Yang and the Milgram cases. Further mesh refinement studies would also be useful for both the Park and Yang and Milgram cases.

Chapter 6: Conclusions and Recommendation

Simulation of bubble plumes is important in many industrial applications. In this study, a hybrid LPT-VOF solver was developed in OpenFOAM to simulate fluid dynamics and mass transfer in bubble plumes. The VOF method is used to simulate the free surface of the bubble plumes, while LPT method is used to track the bubbles individually in the liquid phase. The solver combines the compressible VOF solver and the Lagrangian library in OpenFOAM. Specifically, the solver uses `compressibleInterFoam` with modifications to the phase fraction conservation, momentum conservation, pressure, and species conservation equations to account for the presence of Lagrangian particles occupying the same volume. Interphase mass, species and momentum exchange sources, the compressibility of gas, and a mass transfer model were implemented by modifying the Lagrangian library. The implementation of the solver was verified against the theoretical solutions through a series of verification cases. The solver was validated by comparing simulation results to experimental data for a set of vertically- and horizontally-injected gas plumes.

To test the predictions of the LPT-VOF solver on the fluid dynamics, validation cases that based on the experiments conducted by Simiano (2005) were simulated. The simulation results from Dhotre and Smith (2007) and Dhotre et al. (2009) were used to help in tuning the parameters in the closure models. This validation case was simulated using the LES and the RANS turbulence models. The Smagorinsky (1963) SGS model was used for the LES simulations, while the k-ε model was chosen for the RANS simulations. Three lift coefficients (0.1, 0.288 and 0.5) were used to investigate the effects of the lift coefficient. Two different meshes were used to test the mesh dependence. Three different bubble injection flow rates were also tested using the LES turbulence model to study the effect of gas superficial velocity on fluid dynamics. The effect of a turbulent dispersion model on the predictions was evaluated using the RANS turbulence model. The gas volume fraction, axial gas and liquid velocities, and turbulent kinetic energy at three different elevations (0.35 m, 0.75 m and 1.1 m) were compared with the experimental data and the EE simulation results. The solver predicted similar results of the gas volume fraction, axial gas

and liquid velocities, and turbulent kinetic energy for both the coarse and fine meshes in the LES and the RANS simulations. The lift coefficient study showed that the gas volume fraction and turbulent kinetic energy are strongly affected by the lift coefficient. Higher lift coefficients result in more spreading of the plume in the radial direction and lower gas volume fraction values near the centerline. The predictions using a lift coefficient of 0.5 are the best among the three lift coefficients, which means that 0.5 was found to be most suitable for a bubble size of 2.5 mm. The turbulent dispersion model was found to have a significant impact on the spreading of the plume, but it does not significantly affect the axial liquid velocity and the turbulent kinetic energy predictions. The flow rate study showed that the results for the lower flow rates underpredict the gas volume fraction at the centerline of the plume but overpredict the plume radius. The results for the higher flow rates overpredict the gas volume fraction, axial gas and liquid velocities, and the turbulent kinetic energy but have better fits to the experimental data and the simulation results than the EE model. Overall, the predicted results are in good agreement with the experimental data and the results from EE simulations.

Fluid dynamics and mass transfer were investigated in a small-scale case and a large-scale case using the LPT-VOF solver. The small-scale case was based on the experiments conducted by Park and Yang (2017). In this case, the bubble plumes were injected horizontally into a rectangular tank. The mesh dependency was tested using one of the five selected cases on three different meshes with an initial assumed bubble size of 2 mm. Since the bubble sizes were not measured in the experiments, a bubble size sensitivity study was also performed to investigate the effect of the bubble size on the fluid dynamics and the mass transfer. The bubble size sensitivity study was performed on the intermediate mesh because it gave a better prediction of the spreading length and width compared to the coarse mesh. The sensitivity study for the bubble size showed reasonable trends for the selected cases, but an actual average bubble size could not be estimated due to the lack of a mesh independent solution and model simplifications. The large-scale case was based on the experiments by Milgram (1983), where the gas was injected through a pipe into a lake with four different flow rates. The highest experimental flow rate was chosen as the validation case in this study, and a mesh refinement study was not considered for this case due to the computational time for the large-scale case. The predicted gas volume fraction, plume

velocity, and plume radius for the simulations for both the no mass transfer and mass transfer cases provided reasonable predictions compared to the experimental results. It was estimated that only a maximum of 2.88% of the injected gas could dissolve. Therefore, mass transfer is expected to have a negligible effect on fluid dynamics results in this case.

One of the main limitations of the developed LPT-VOF solver is that it only currently allows transition from LPT to VOF. That is, the transition from VOF to LPT is not permitted in the current implementation of the solver. Additionally, based on the validation cases, it appears that the turbulence modelling approach could be further refined to provide more accurate predictions. Further, a collision model was not includes in this work due to the lack of the empirical data for the model parameters. Also, the current solver did not include the effect of surface resistance on bubble disengagement rates at the free surface.

For the future work, the transition from VOF to LPT should be implemented in the current solver. Other turbulence modelling approaches should be studied to give to try to improve predictions. More work could also be done regarding the implementations of the surface resistance and the collision model with suitable model parameters. Further, in reality, the bubble size distributions exist in the bubble plumes due to coalescence and breakup of the bubbles. Gruber et al. (2013) and van den Hengel (2005) have included the bubble size distribution modelling in their work using the EL method. Similar models should be further implemented in the solver to track changes in the bubble size distribution due to breakup and coalescence of the bubbles.

References

Anderson, T., & Jackson, R. (1967). A fluid mechanical description of fluidized beds. *Industrial & Engineering Chemistry Fundamentals, 6*(4), 527–539.

ANSYS, Inc. (2009). Mixture Model Theory. Retrieved on July 27, 2019 from http://www.afs.enea.it/project/neptunius/docs/fluent/html/th/node308.htm

Asad, A., Kratzsch, C., & Schwarze, R. (2017). Influence of drag closures and inlet conditions on bubble dynamics and flow behavior inside a bubble column. *Engineering Applications of Computational Fluid Mechanics, 11*(1), 127-14.

Badreddine, H., Sato, Y., Niceno, B., & Prasser, H. (2015). Finite size Lagrangian particle tracking approach to simulate dispersed bubbly flows. *Chemical Engineering Science, 122*, 321-335.

Becker, S., Sokolinchin, A., & Eigenberger, G. (1995). Gas-liquid flow in bubble columns and loop reactors. Part II. Comparison of detailed experiments and flow simulations. *Chemical Engineering Science, 49*, 5747.

Bird, R.B., Stewart, W.E. & Lightfoot, E.N. (1960). Transport Phenomena. *Wiley, New York.*

Boemer, A., Qi, H., & Renz, U. (1997). Eulerian simulation of bubble formation at a jet in a two dimensional fluidized bed. *International Journal of Multiphase Flow, 23*, 927–944.

Brevik, I. (1977). Two-Dimensional Air-Bubble Plume. *Journal of the Waterway, Port, Coastal and Ocean Division, 103*(1), 101-115.

Brevik, I. & Killie, R. (1996). Phenomenological description of the axisymmetric air-bubble plume. *International Journal of Multiphase Flow, 22*(3), 535-549.

Burns, A.D., Frank, T., Hamill, I., & Shi, J. (2004). The Favre averaged drag model for turbulent dispersion in Eulerian multi-phase flows. *In: 5th International Conference on Multiphase Flow, ICMF, Yokohama, Japan.*

Buscaglia, G. C., Bombardelli, F. A., & García, M. H. (2002). Numerical modeling of large-scale bubble plumes accounting for mass transfer effects. *International Journal of Multiphase Flow, 28*(11), 1763-1785.

Buwa, V.V., Deo, D.S., & Ranade, V.V. (2006). Eulerian-Lagrangian simulations of unsteady gas-liquid flows in bubble columns. *International Journal of Multiphase Flow, 32*(7), 864-885.

Chuang, T.J. & Hibiki, T. (2017). Interfacial forces used in two-phase flow numerical simulation. *International Journal of Heat and Mass Transfer, 113,* 741-754.

Clift, R. (1978). Bubbles, Drops, and Particles. *Academic Press, New York; London.*

Darmana, D., Deen, N.G., & Kuipers, J.A.M. (2005). Detailed modeling of hydrodynamics, mass transfer and chemical reactions in a bubble column using a discrete bubble model. *Chemical Engineering Science, 60*(12), 3383-3404.

Davidson, M.R. (1990). Numerical calculations of two-phase flow in a liquid bath with bottom gas injection: the central plume. *Applied Mathematical Modelling 14*, 67–76.

Deen, N.G., Solberg, T., & Hjertager, B.H. (2001). Large eddy simulation of the Gas-Liquid flow in a square cross-sectioned bubble column. *Chemical Engineering Science, 56*(21), 6341-6349.

Dhotre, M.T. & Smith, B.L. (2007). CFD simulation of large-scale bubble plumes: Comparisons against experiments. *Chemical Engineering Science, 62*(23), 6615-6630.

Dhotre, M.T., Niceno, B., & Smith, B.L. (2008). Large eddy simulation of a bubble column using dynamic sub-grid scale model. *Chemical Engineering Journal, 136*(2), 337-348.

Dhotre, M.T., Niceno, B., Smith, B.L., & Simiano, M. (2009). Large-eddy simulation (LES) of the large scale bubble plume. *Chemical Engineering Science, 64*(11), 2692-2704.

Dhotre, M., Deen, N., Niceno, B., Khan, Z., & Joshi, J. (2013). Large Eddy Simulation for Dispersed Bubbly Flows: A Review. *International Journal of Chemical Engineering, 2013*, 22.

Ding, J. & Gidaspow, D. (1990). A bubbling fluidization model using theory of granular flow. *AIChE Journal, 36*(4), 523–538.

Ding, J. & Lyczkowski, R. (1992). Three-dimensional kinetic theory modeling of hydrodynamics and erosion in fluidized beds. *Powder Technology, 73*, 127–138.

Ditmars, J. D. & Cederwall, K. (1974). Analysis of air-bubble plumes. *In proceedings, 14th Coastal Engineering Conference*, Copenhagen.

Einarsrud, K., & Brevik, I. (2009). Kinetic Energy Approach to Dissolving Axisymmetric Multiphase Plumes. *Journal Of Hydraulic Engineering-Asce, 135*(12), 1041-1051.

Enwald, H., Peirano, E., & Almstedt, A. (1996). Eulerian two-phase flow theory applied to fluidization. *International Journal of Multiphase Flow, 22*, 21–66.

Fraga, B., Thorsten, S., Lai, C., & Socolofsky, S.A. (2016). A LES-based Eulerian-Lagrangian approach to predict the dynamics of bubble plumes. *Ocean Modelling, 97*, 27-36.

Frössling, N. (1938). Über die Verdunstung falender Tropfen. *Beitr Geophys. 52*, 170–216.

Garg, S., & Pritchett, J. (1975). Dynamics of gas-fluidized beds. *Journal of Applied Physics, 46*(10), 4493–4500.

Godderidge, B., Phillips, A., Lewis, S.G., Turnock, S., Hudson, D., & Tan, M. (2008). The simulation of free surface flows with Computational Fluid Dynamics. *ANSYS UK User Conference*.

Gosman, A.D., & Ioannides, E., 1981. Aspects of computer simulation of liquid fueled combustors. *In: Proceedings of 19th Aerospace meeting, AIAA*, St. Louis, MO, Paper No. 81-03223.

Gruber, M.C., Radl, S., & Khinast, J.G. (2013). Coalescence and Break-Up in Bubble Columns: Euler-Lagrange Simulations Using a Stochastic Approach. *Chemie Ingenieur Technik, 85*(7), 1118-1130.

Helfer, F., Lemckert, C., & Zhang, H. (2012). Influence of bubble plumes on evaporation from non-stratified waters. *Journal of Hydrology, 438*, 84-96.

Hessenkemper et al. (2019). Contamination effects on the lift force of ellipsoidal air bubbles rising in saline water solutions. DOI: 10.1016/j.cej.2019.04.169

Hibiki, T. and Ishii, M. (2007). Lift force in bubbly flow systems. *Chemical Engineering Science, 62*(22), 6457-6474.

Higbie, R. (1935). The rate of absorption of a pure gas into a still liquid during short periods of exposure. *Trans. AIChE 31*, 365–389.

Hu, G., & Celik, I. (2008). Eulerian-Lagrangian based large-eddy simulation of a partially aerated flat bubble column. *Chemical Engineering Science, 63*(1), 253-271.

Hughmark, G.A. (1967). Liquid-liquid spray column drop size, holdup, and continuous phase mass transfer. *Industrial & Engineering Chemistry Fundamentals, 6*(3), 408-413.

Ishii, M. (1975). Thermo-fluid dynamic theory of two-phase flow. *Direction des Etudes et Recherches d'Electricité de France,* Eyrolles, Paris, France.

Ishii, M., & Zuber, N. (1979). Drag coefficient and relative velocity in bubbly, droplet or particulate flows, *AIChE Journal, 25*(5), 843–855.

Ishii, M., & Hibiki, T. (2011). Thermo-fluid dynamics of two-phase flow (2nd ed.). *New York: Springer.*

Jain, D., Kuipers, J.A.M, & Deen, N.G. (2014). Numerical study of coalescence and breakup in a bubble column using a hybrid volume of fluid and discrete bubble model approach. *Chemical Engineering Science, 119*, 134-146.

Kiambi, S.L., Billet, A., Dupont, J., Colin, C., & Risso, F. (2003). Measurements of Bubble Characteristics: Comparison Between Double Optical Probe and Imaging. *Canadian Journal of Chemical Engineering, 81*(3-4), 764-770.

Lain, S., Broder, D., Sommerfeld, M., & Goz, M.F. (2002). Modelling hydrodynamics and turbulence in a bubble column using the Euler–Lagrange procedure. *International Journal of Multiphase Flow, 28*(8), 1381-1407.

Laux, H., & Johansen, S.T. (1999), A CFD analysis of the air entrainment rate due to a plunging steel jet combining mathematical models for dispersed and separated multiphase flows. *Fluid Flow Phenomena in Metals Processing*, 21–30.

Lopez de Bertodano, M. (1992). Turbulent Bubbly Two-phase Flow in a Triangular Duct. *Ph. D. Thesis, New York.*

Manninen, M., Taivassalo, V., & Kallio, S. (1996). On the mixture model for multiphase flow. *Technial Research Centre of Finland, VTT Publications, 288*, 67.

Milgram, J. H. (1983). Mean flow in round bubble plumes. *Journal of Fluid Mechanics, 133*, 345-376.

Ming, F.R., Sun, P.N, & Zhang, A.M. (2017). Numerical investigation of rising bubbles bursting at a free surface through a multiphase SPH model. *Meccanica, 52*(11-12), 2665-2684.

Morton, B., Taylor, G., & Turner, J. (1956). Turbulent Gravitational Convection from Maintained and Instantaneous Sources. *Proceedings of the Royal Society of London. Series A, Mathematical and Physical Sciences (1934-1990), 234*(1196), 1-23.

Olsen, J.E., & Skjetne, P. (2016). Current understanding of subsea gas release: A review. *Canadian Journal of Chemical Engineering, 94*(2), 209-219.

Olsen, J.E., & Skjetne, P. (2016). Modelling of underwater bubble plumes and gas dissolution with an Eulerian-Lagrangian CFD model. *Applied Ocean Research, 59*, 193-200.

Olsen, J.E., Skjetne, P., & Johansen, S.T. (2017). VLES turbulence model for an Eulerian–Lagrangian modeling concept for bubble plumes. *Applied Mathematical Modelling, 44*(C), 61-71.

Olsen, J.E., Dunnebier, D., Davies, E., Skjetne, P, & Morud, J. (2017). Mass transfer between bubbles and seawater. *Chemical Engineering Science, 161*, 308-315.

OpenFOAM Foundation. (2019). Retrieved from https://openfoam.org/

Park, S., & Yang, H. (2017). Experimental investigation on mixed jet and mass transfer characteristics of horizontal aeration process. *International Journal of Heat and Mass Transfer, 113*, 544-555.

Pritchett, J., Blake, T., & Garg, S. (1978). A numerical model of gas fluidized beds. *AIChE Symposium Series, 74*(176), 134–148.

Rafique, M., Chen, P, & Dudukovic, M.P. (2004). Computational modeling of gas-liquid flow in bubble columns. *Reviews in Chemical Engineering, 20*, 225-375.

Ranz, W.E., & Marshall, W.R.J. (1952). Evaporation from droplets, parts I & II. *Chemical Engineering Progress 48*(3), 173–180.

Roghair, I., Lau, Y., Deen, N.G., Slagter, W., Baltussen, V.S., & Kuipers, J. (2011). On the drag force of bubbles in bubble swarms at intermediate and high Reynolds numbers. *Chemical Engineering Science, 66*(14), 3204–3211.

Sander, R. (2015). Compilation of Henry's law constants (version 4.0) for water as solvent. Atmospheric Chemistry and Physics, 15, 4399-4981.

Sato, Y., & Sekoguchi, K. (1975). Liquid velocity distribution in two-phase bubble flow. *International Journal of Multiphase Flow, 2*, 79-95.

Sato, Y., Sadatomi, M., & Sekoguchi, K. (1981). Momentum and heat transfer in two phase bubble flow, Part I theory. Liquid velocity distribution in two phase flow. *International Journal of Multiphase Flow, 7*(2), 167–177.

Schaub, F., & Pluschkell, W. (2006). Turbulent Enhancement of Mass Transfer in Bubble Plumes. *Chemical Engineering & Technology, 29*(9), 1073-1083.

Sheng, Y., & Irons, G. (1995). The impact of bubble dynamics on the flow in plumes of ladle water models. *Metallurgical and Materials Transactions B, 26*(3), 625-635.

Simano, M. (2005). Experimental investigation of large-scale three-dimensional bubble plume dynamics. *ETH Zurich Research Collection*. Doctorial Thesis at Palermo University, Italy.

Simonin, O., & Viollet, P.L. (1988). On the computation of turbulent two phase flows in Eulerian formulation. *In: Proceedings of the Conference, EUROMECH, vol. 234, Toulouse, France.*

Skjetne, P., & Olsen, J. E. (2012). A parcel based modelling concept for studying subsea gas release and the effect of gas dissolution. *Progress in Computational Fluid Dynamics, 12*, 187-195.

Smagorinsky, J. (1963). General circulation experiments with the primitive equations. *Monthly Weather Review, 91*, 99–165.

Spalart, P.R., Deck, S., Shur, M.L., Squires, K., Strelets, M.K, & Travin, A. (2006). A new version of detached-eddy simulation, resistant to ambiguous grid densities. *Theoretical and Computational Fluid Dynamics, 20*, 181-195.

Tomiyama, A., Kataoka, I., Zun, I., & Sakaguchi, T. (1998). Drag coefficients of single bubbles under normal and micro gravity conditions. *JSME International Journal, Series B, 41*(2), 472–479.

Tomiyama, A., Tamai, H., Zun, I., & Hosokawa, S. (2002). Transverse migration of single bubbles in simple shear flows. *Chemical Engineering Science, 57*(11), 1849–1858.

Tsuchiya, K., Furumoto, A., Fan, L., & Zhang, J. (1997). Suspension viscosity and bubble size velocity in liquid–solid fluidized beds. *Chemical Engineering Science, 52*(18), 3053-3066.

Tsuji, Y., Morikawa, Y., & Terashima, K. (1982). Fluid-dynamic interaction between twospheres. International Journal of Multiphase Flow, 8, 71–82.

van den Hengel, E.I.V., Deen, N.G., & Kuipers, J.A.M. (2005). Application of coalescence and breakup models in a discrete bubble model for bubble columns. *Industrial and Engineering Chemistry Research, 44*(14), 5233–5245.

Van Wachem, B.G.M. & Almstedt, A.E. (2003). Methods for multiphase computational fluid dynamics. *Chemical Engineering Journal, 96*, 81-98.

Wang, Z., Yang, J., & Stern, F. (2008). Comparison of Particle Level Set CLSVOF Methods for Interfacial Flows. *In 46th AIAA Aerospace Sciences Meeting and Exhibit*, Reno, Nevada.

Welty, J.R., Wicks, C.E., Wilson, R.E., & Rorrer, G.L. (2008). Fundamentals of Momentum, Heat and Mass Transfer, 5th Edition. John Wiley & Sons, Inc., Hoboken, p. 554, 678.

Wörner, M. (2012). Numerical modeling of multiphase flows in microfluidics and micro process engineering: A review of methods and applications. *Microfluidics and Nanofluidics, 12*(6), 841-886.

Xue, J., Chen, F., Yang, N., & Ge, W. (2017). Eulerian-Lagrangian simulation of bubble coalescence in bubbly flow using the spring-dashpot model. *Chinese Journal of Chemical Engineering, 25*(3), 249-256.

Yang, C., & Löhner, R. (2005). Computation of 3D Flows with Violent Free Surface Motion. *Proceeding of the 15th ISOPE*, Seoul, Korea.